Surface Forces during Electrophoretic Assembly of Micron Scale Silica Particles

by

Ryan J. Kershner

S.B. Materials Science and Engineering
S.B. Humanities
Massachusetts Institute of Technology, 1998

SUBMITTED TO THE DEPARTMENT OF MATERIALS SCIENCE AND ENGINEERING IN PARTIAL FULFILLMENT OF THE REQUIREMENTS FOR THE DEGREE OF

DOCTOR OF PHILOSOPHY IN MATERIALS ENGINEERING
AT THE
MASSACHUSETTS INSTITUTE OF TECHNOLOGY

FEBRUARY 2004

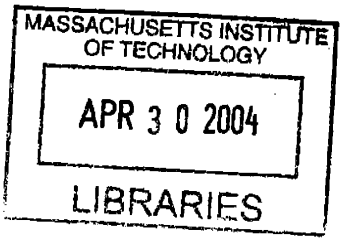

Signature of Author: _____
Department of Materials Science and Engineering
January 13, 2004

Certified By: _____
Michael J. Cima
Sumitomo Electric Industries Professor of Engineering
Thesis Supervisor

Accepted By: _____
Harry S. Tuller
Professor of Ceramics and Electronic Materials
Chair, Departmental Committee on Graduate Students

Surface Forces during Electrophoretic Assembly of Micron Scale Silica Particles

by

Ryan J. Kershner

Submitted to the Department of Materials Science and Engineering
on January 13, 2004 in Partial Fulfillment of the Requirements for
the Degree of Doctor of Philosophy in Materials Engineering

ABSTRACT

A system of platinum microelectrodes was fabricated on a sapphire substrate by lithographic patterning and used to manipulate 1.58 μm silica particles in-plane. A digital video system was used to image the motion of particles far from the electrodes and their deposition onto the working electrode during application of a DC potential. The role of electrode reversibility was investigated and the performance of the as-deposited electrodes was improved by electrolytic plating of platinum. Particles were also seen to adhere to the substrate before reaching the electrode. Force distance curves were recorded using a colloid probe atomic force microscopy technique to directly measure the interaction of the silica particles with the sapphire substrate. This data validated the observed adhesion at the electrode and provided further support for the temporal and spatial reduction in pH. The role of Faradaic processes and the diffusion of potential determining ions in electrophoretic deposition was also considered. The zeta potential of planar sapphire substrates for three different crystallographic orientations was measured by a streaming potential technique in the presence of KCl and $(CH_3)_4NCl$ electrolytes. The streaming potential was measured for large single crystalline C-plane (0001), A-plane $(11\bar{2}0)$, and R-plane $(1\bar{1}02)$ wafers over a full pH range at three or more ionic strengths ranging from 1 to 100 mM. The results reveal a shift in the iso-electric point (i.e.p.) of the three samples by as much as two pH units, with the R-plane surface exhibiting the most acidic behavior and the C-plane samples having the highest i.e.p. The acidity of the sapphire wafers is explained in terms of an absence of adsorbed hydroxyl groups for these surfaces prepared at room temperature. Modified Auger parameters (MAP) were calculated from XPS spectra of a mono-layer of iridium metal deposited on the sapphire by electron beam deposition. A shift in MAP consistent with the observed differences in i.e.p. of the surfaces confirms the effect of surface structure on the transfer of charge between the Ir and sapphire, hence accounting for the changes in acidity as a function of crystallographic orientation.

Thesis Supervisor: Michael J. Cima
Title: Sumitomo Electric Industries Professor of Engineering

Acknowledgements

It's hard to believe, after having spent so much of my young life at MIT, that this chapter has come to a close. Looking back, I think I can honestly say that I had about as much fun as the next guy. The knowledge I gained from MIT and its community goes far beyond the work contained in these pages and I look forward to continuing down this road: there is always much to learn.

I owe a great debt of gratitude to my thesis advisor, Professor Michael Cima. I of course thank him for his financial support — but also for his sharp insight and ability to grasp the most salient details from any technical problem, no matter how complex. It has been said that imitation is the greatest form of admiration, and I am pleased to embark upon a career as a scientist with Michael's support and encouragement behind me. I only hope I can live up to his expectations in all my future endeavors.

I am also honored to have included two very distinguished faculty on my thesis committee. Professors Ian Hunter and Ned Thomas served as invaluable resources, providing thoughtful discussions and probing questions that forced me to think beyond the framework from which this project was conceived.

Funding for this project came from the National Science Foundation and the National Aeronautics and Space Administration. I am also grateful for collaborations with Professor Menachem Elimelech at Yale University and his students, Jeffrey Chen and Sharon Walker. Their expertise and very generous hospitality contributed greatly to the success of this work.

My interest in the rich area of Materials Science and Engineering is rooted in my very early days at MIT and I have been privileged to have been mentored by a number of outstanding faculty. Professor Don Sadoway continues to inspire students through his teaching with his savvy presentation and excellent sense of style. Thank you for the in-depth discussions and encouragement. Other faculty and administrators I wish to thank include Dr. Bernd Widdig, Professor Sam Allen, Professor Yet-Ming Chiang, Deans Ike Colbert and Larry Benedict, Joe Contrada, and Professor Michael Ouellette. The late Professor Gus Witt was wholly responsible for giving me my first research opportunity within the department and his vision will continue to inspire students for many years to come.

I also wish to recognize by name those in the Ceramics Processing Laboratory who have contributed to this work, either through direct technical means or by way of more lively (but equally valuable) discussions. Mindy Tupper and I have been colleagues working on parallel research tracks for some time and have had numerous opportunities to share advice, scientific or otherwise. I wish her well in her future endeavors, wherever they may take her. I enjoyed a very productive summer in 2003 working alongside of my friend Joe Bullard. Thanks to him for his hard work and dedication. I will no doubt run into Joe again and hope that this work might provide a brick in the foundation for his future research at MIT and beyond. Thanks to Ariel Virshup for her contributions in the early stages of the AFM work. Other inspirations include Drs. Scott Uhland, John Santini, Sherry Morrisette, Mike Read, Mani Gopal, Masa Yoshizumi and all the others who have passed through this lab and left their mark. Thanks to Barbara Layne for her kindness, to Lenny Rigione for his wisdom, and to John Centerino for all the opportunities to take my mind off of work, if only for a little bit at a time.

I have also been fortunate to rely upon a solid support network of friends in Boston and beyond. Thank you first and foremost to the gentlemen of 99 Bay State Road — past, present, and future — who had a profound impact on my character. The MIT Logarhythms, the Theater Arts Department at MIT, the Tanglewood Festival Chorus, the volunteers and community of the Graduate Student Council, and the staff and patrons of the Muddy Charles Pub are all responsible for the successful completion of this research. Special thanks to Jen DiMase for her understanding and her infectious smile. I could not have done this without her. Thanks to Hartmut Rudmann, Catherine Bishop, Rob Bernstein, Clark Allred, Raymundo Arroyave, and all my colleagues in the department whose friendships I value dearly. My good friends Meredith Cooley, Dan Morgan, and Mike Smith are perhaps the kindest people I will ever meet. Thanks for making me feel at home in my time of, well, homelessness.

I have been honored over the past several years to count Richard Holman among my closest friends. Thanks for the good cheer and for always offering a balanced perspective on just about anything. I trust I will continue to be impressed by your achievements. I hold my colleague and good friend Hong-Ren Wang in the highest regard and know he will succeed in anything he chooses to tackle. I thank Sarah for her sweetness and for opening my eyes to see things in a whole new way. Someday I hope to repay you. I have shared some good times with my brother Dave and sister Melissa and look forward to many more. Thanks to them for teaching me how to enjoy life and all its challenges.

Last but far from least I wish to thank my parents, Paul and Mary Ann, for their support and guidance. Much of the dedication and perseverance necessary to bring this work to completion had its early roots in my hometown of Williamsburg, VA. I am truly honored to have been brought up by the most caring folks one could have. I am truly happy to have made you proud.

The Devil is in the details. . .
But so is salvation.

- ADM Hyman G. Rickover,
Father of the modern nuclear Navy

Table of Contents

List of Figures

List of Tables

Chapter 1: Introduction

1.1 Motivation

The surfaces of particles and electronic components in an electrolyte adopt a charge due to the specific absorption of potential determining ions. This surface charge can be used to manipulate the spatial position of the particles under the influence of an applied electric field. Microelectrodes patterned on a substrate using standard ultraviolet photolithography allow the field to be shaped to achieve a specific arrangement of components. Small parts are subject to a wide variety of forces that are not normally important to macrobodies because of their larger surface to volume ratio. Advanced packaging technologies for electronics and new optical devices share similar needs for harnessing these forces during assembly of components. Complete control over component placement and alignment is critical for high frequency electronics where packaging of filters off chip seriously degrades the performance of the circuit. Discrete components are rapidly decreasing in dimension, becoming so small that the assembly processes used to mount them must account for static electric charge, van der Waals forces acting through surfaces, other adhesion forces, and, in the not too distant future, Brownian dynamics. Optical system assembly presents the same challenges with the added requirement of ultra precision placement. The demand for discrete components has not decreased with the improvements in VLSI fabrication technology. Indeed, system engineering has driven the demand for higher performance components. Discreet, high performance components have become smaller with a greater emphasis on packaging and assembly processes.

The surface mount capacitor is a simple example. Worldwide production of these devices is now approaching six billion per month, up 30% from just a few years ago. The capacitance per unit volume has increased over two orders of magnitude in the past fifteen years due to reductions in layer thickness and improvements in the component materials. This has allowed for reductions in component size. The first large scale introduction of the 0201 minichip capacitor with dimensions of only 300 by 600 μm occurred this past year. Smaller capacitors can be manufactured but their use is severely limited by current mechanical assembly methods. This is because the detrimental influence of uncontrolled electrostatic forces and mechanical vibrations become more severe as the component dimensions decrease. Micron-scale components are much more strongly

influenced by surface forces and Brownian motion than their macroscopic counterparts due to their higher surface to volume ratio.

High-speed automated assembly of surface mount components is practiced on a large scale throughout the world. The equipment varies in detail but all are based on mechanical placement of components using a contact technique. Components are typically provided to the assembly equipment in large plastic reels. The actuators remove the component and place it on the target substrate. The accuracy of placement and the reliability of the component hand-off to the substrate depend on many factors, including the vibration inherent in mechanical systems operating at high speed and the adhesion of components to the assembly tooling. Shown in Figure 1.1 are 0201 minichip capacitors adhering to a pair of metal tweezers. The parts were stored in a plastic vial and acquired an electrostatic charge due to the friction of rubbing against one another and the container. The electrostatic attraction of the parts to the metal as well as to themselves is apparent. The presence of this electrostatic charge illustrates a critical problem in component handling that is highly dependent on environmental conditions such as temperature and humidity. Fine-tuning of the alignment and placement of components during mechanical placement operations is not possible without the controlled use of another force in order to overcome mechanical vibrations that lead to improper assembly.

Applications of ordered structures composed of small components are not limited to microelectronics. Recent developments in biotechnology have made the assembly of micron-scale particles into patterned structures extremely attractive for use as templates for cell growth, as biosensers for use in immunological tests, and as test cells for research on fundamental cellular

(a) **(b)**

Figure 1.1: **(a)** Photo of 0201 capacitor and **(b)** demonstration of static charge induced adhesion to a pair of tweezers.

and molecular phenomena. Interest in miniaturization is driven by the need for test cells which are capable of assessing thousands of independent combinations of biological material. Current industry standard techniques for fabricating microarrays of proteins or nucleic acids, such as microspotting or microjet printing, require large sample areas. The minimum size droplet which can currently be deposited to form a single test cell is on the order of a nanoliter, placing additional restrictions on the speed with which these microarrays may be fabricated. The extremely small scale of biological material used in these tests requires droplets only on the order of a femtoliter. Thus, assembly techniques capable of placing smaller sample sizes have the potential to greatly improve the speed with which microbiological experiments may be carried out.

Even smaller scale assembly methods are required for the manufacture of new advanced composite materials. One remarkable example is photonic crystals, in which the characteristic dimension of the ordering phenomenon is fairly large compared with the length scale of the forces which serve to stabilize the components of the structure. Simple dielectric materials can be artificially arranged in periodic structures to eliminate or enhance the density of electromagnetic states within a given frequency range [1]. The usefulness of three-dimensional photonic band gap structures has been theoretically demonstrated, with applications ranging from waveguides capable of channeling light with nearly zero loss to optical resistors and tunable filters [2][3][4]. Great strides have recently been made in the fabrication of materials exhibiting a full or partial photonic band gap [5][6][7]. Ordered periodic arrays consisting of colloidal particles which self-assemble to form an fcc lattice have been used either as free standing structures or as templates for infiltration with another material [8]. The latter technique, designed to increase the dielectric contrast necessary to produce a complete band gap, makes use of heat treatment of chemical etching to remove the particles, leaving behind a periodic array of highly ordered micropores with a continuous air phase [9][10]. The development of advanced patterning techniques such as microcontact printing [11][12] to selectively deposit charged regions on a substrate has been crucial for providing a template for colloidal crystallization [13] and for producing ordered arrays of colloids on a surface [14][15]. Precise control over the center-to-center distance between particles has been achieved using this technique, resulting in the formation of self-assembled arrays of colloids with very low defect concentrations. Other novel techniques using electric-field induced capillary forces show promise for controlling interparticle spacings at distances much larger than would be possible by traditional charge stabilization techniques [16].

1.2 Application Examples of Surface Forces in Assembly

Applications abound for the assembly of micron-scale particles at interfaces. This has led to numerous studies which focus on the manipulation of micro- and nanoscale forces for the fabrication of novel systems and structures. Three such examples will be presented here, namely mechanical assembly, fluidic self-assembly, and electrophoretic deposition.

1.2.1 Mechanical Assembly

Mechanical assembly methods represent the current state of the art in industrial assembly of small microelectronic components. A typical mechanical assembly process uses an automated mechanical actuator to contact the part and move it to an exact location for placement on the substrate. These include pick and place operations (similar to that described earlier to place surface mount capacitors) and flip chip assembly. Flip chip technology uses the surface tension of the solder joints to self-align components. The component partially aligned with high speed actuators and the solder coated surfaces of the component and target are brought into contact. The temperature of the entire assembly is raised, and the surface tension of the molten solder pulls the component into place. The alignment accuracy of this technique varies from a few microns to eight microns or more. More accurate placement of devices such as light emitting diodes can be achieved by use of photodetectors which provide a feedback mechanism. The diode is powered and its position slowly adjusted while the light output through the detector is measured. The feedback system repeatedly moves the device, then measures the output intensity until the maximum output is achieved. This process is very slow, which significantly increases the manufacturing cost [17].

Researchers at the University of Tokyo have developed a micro-robotic contact technique of assembling three-dimensional photonic band gap crystals using particles on the micron-scale. The robot consists of a left hand that holds a substrate containing randomly placed particles and a right hand which contains a needle-like tool. The tool is used to pick and place each individual particle, allowing the formation of very complicated structures through this highly localized assembly technique. The entire robot assembly is contained within a scanning electron microscope and the hands are remotely controlled by an operator. Each particle is contacted by the robotic needle and moved into position. The process is slow and laborious and can only be used with spherical particles [18]. This technique is an example of work currently being done to adapt the mechanical pick-and-place methods traditionally used in industry to components on a much

smaller scale. This method offers promise for the fabrication of controlled defects within photonic band gap materials for use in waveguide and other applications but is extremely slow and not practical for scale up as an industrial process.

1.2.2 Fluidic Self Assembly (FSA)

A technique for the assembly of microelectronic devices has been described by J.S. Smith *et al.* [19]. The fluidic self-assembly process (FSA) allows the integration of micron scale components into a substrate fabricated from a dissimilar materials system. Devices are fabricated onto specifically-shaped structures of one material into similarly shaped receptacle holes made on a substrate of some other material, such as silicon. This process has been applied to the integration of optical and electronic devices on a single chip module, as in the placement of GaAs light-emitting diodes on silicon substrates, as well as to the fabrication of flat panel displays. FSA provides an alternative to more traditional methods of placing small devices such as epitaxial lift-off and microrobotic assembly. The trend towards reducing device dimensions to the micron scale has significantly limited the application of these mechanical or contact placement processes.

Devices such as GaAs LEDs are first fabricated by molecular beam epitaxy onto a sacrificial substrate. This is followed by selective metallization of the devices to form electrical contacts, as shown in Figure 1.2 (a). The devices are then formed into blocks of uniform dimensions

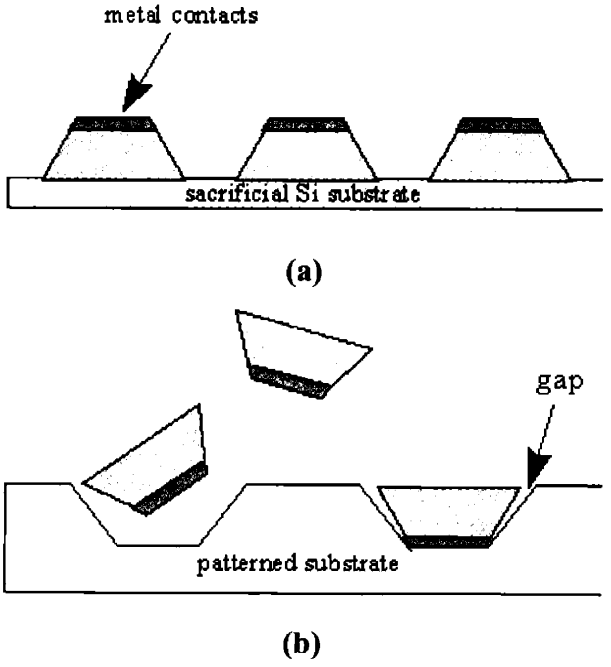

Figure 1.2: Schematic of fluidic self assembly process showing **(a)** the formation of devices on a sacrificial substrate and **(b)** the deposition of devices onto a patterned substrate.

by either ion milling or reactive ion etching at an angle of 55° to the substrate, thus creating a trapezoidal shape. The blocks are freed from the sacrificial substrate by etching away the undoped silicon layer. Devices of different size scales have been assembled using FSA, ranging from on the order of 20 μm to 1.0 mm. The substrate onto which the devices are to be assembled is then patterned with an array of holes by anisotropic etching with KOH. The etchant acts at different rates along different crystal directions. This allows the substrate to be selectively etched along the slower {111} planes, forming the slanted sides of the desired trapezoidal geometry. It is noted by Smith, *et al.* that the shape of the assembled blocks will not perfectly match that of the holes due to process variations, resulting in small gaps between the devices and the silicon substrate [20]. The truncated pyramid geometry facilitates the self alignment of the devices within the holes as illustrated in Figure 1.2 (b). The shape of the substrate determines the orientation of the blocks in a manner similar to the mating of a key with a lock. The holes can be keyed in various fashions to match a device of any shape, thus allowing the symmetry of placement to be reduced to one fold rotation.

The blocks are then suspended in a fluid medium which acts as a carrier for the deposition of the devices onto the patterned substrate. Due to the presence of the heavier interconnect metal on the smaller face of the trapezoids, the blocks tend to orient themselves with this smaller face downwards, corresponding to the geometry of the holes (see Figure 1.2 (b)). The blocks are brought to the vicinity of the substrate by a steady recirculating flow and settle to the surface due to gravity. Acoustic vibration is used to migrate the blocks across the surface until a patterned hole is encountered. The amplitude of vibration can be adjusted to facilitate the settling of the blocks into the holes while minimizing the removal of settled blocks. Blocks which do not fall into receptor sites after a single pass over the substrate are recirculated to the flow inlet and are again vibrated across the surface. This process will continue until a steady state fraction of filled holes is reached. Fill fractions as high as 1.0 have been observed within three minutes for parts having a characteristic dimension of 1.0 mm. Smaller parts (on the order of 30 μm) reached a steady state fill ratio of 0.9 after roughly fifteen minutes. Continuing the process for longer times resulted in no improvement in the fraction of filled sites [19].

Alternate techniques which do not use a recirculating flow mechanism have also been attempted. It has been demonstrated that while the local fill ratios in certain regions may approach 0.5, the total yield of filled sites is extremely low (on the order of 0.03) [21]. The

advantages gained by a continuous process are therefore significant. Smith *et al.* present a general discussion of the factors which affect the filling efficiency of the holes. An empirical observation of yield as a function of the concentration of parts within the fluid led to the conclusion that a large number of blocks in solution enhances the filling efficiency.

Another critical factor in the efficiency of the FSA process is the adhesion forces between the blocks and the wells. These forces are attributed to Van der Waals interactions but the nature of the forces was not investigated experimentally [19]. Empirical observations revealed that roughening of the surface of the blocks resulted in a larger fraction of filled sites. This is likely due to the reduction in contact area between the devices and the substrate which in turn reduces the average magnitude of the Hamaker force per unit area. It was also observed that the steady state filling efficiency of the larger blocks was much greater than that of the smaller blocks. The smaller devices have a higher surface to volume ratio. The greater exposed surface area increases the overall magnitude of surface forces as compared with the force due to gravity. Thus smaller parts will be more susceptible to sticking to the surface, presenting a physical barrier to the migration and deposition of other nearby blocks once proper placement occurs. It should also be noted that the same surface forces which cause undesirable adhesion may also be beneficial in keeping the correctly oriented blocks within the holes. This can be controlled by ensuring that the contact surface at the bottom of the holes is as smooth as possible for maximum adhesion between the substrate and the blocks.

The effect of the dielectric properties of the substrate and devices was also discussed. The surface forces which cause blocks to stick to the substrate will depend on the dielectric constant of the fluid medium. These forces will be significantly reduced by the presence of the fluid as compared with the same effects in air. Additionally, the strength of the Van der Waals attraction will be dependent on the relative dielectric constants of the devices and the substrate. Various coatings and other surface treatments have been proposed to optimize these interactions. Mustakis, *et al.* suggests the use of self assembled monolayers composed of functionalized long chain alkanes. Hydrophobic and hydrophilic SAMs can be preferentially deposited onto the substrate, increasing the adhesion of the parts to the bottom of the holes while allowing the parts to glide across the upper surface without sticking [22].

1.2.3 Electrophoretic Assembly

Particles in a liquid can acquire a surface charge by preferential adsorption of ions from solution, dissociation of surface groups, isomorphic substitution, adsorption of polyelectrolytes from solution, or accumulation of electrolytes at the surface. The primary mechanism of charging for colloidal suspensions of ceramic particles is preferential adsorption of ions, especially in aqueous suspensions. Clay particles are charged primarily by isomorphic substitution. Preferential adsorption of ions from solution occurs when ceramic particles are placed in a liquid such as water with an electrolyte such as an acid, base, or a metal salt. Most oxide surfaces are hydrated, so that there are hydroxyl groups on the surface. H^+ ions are adsorbed on the surface if the solution is acidic, creating a positive surface charge. A basic solution causes adsorption of hydroxide ions, which form water with the H^+ ions of the surface hydroxyl groups and leave O^- ions on the surface, thus creating a negative surface charge. This surface charge is balanced by counter ions in a diffuse layer extending into the solution. The width of this electrical double layer is characterized by the Debye length, which is a function of the dielectric constant of the dispersion medium, the deposition temperature, the concentration of the electrolyte in solution, and the valence of the ions of the dissociated electrolyte. The potential associated with the double layer is characterized by the potential at the shear plane, known as the zeta potential. The zeta potential depends on the magnitude of the charge on the particle surface. The surface charge is changed by varying the concentration of potential determining ions in the solution. The concentration of potential determining ions present depends on the type of electrolyte used and the degree of dissociation of the electrolyte in the liquid. In aqueous suspensions, an acid or base may be added to change the concentration of H^+ ions, which are potential determining.

The force on the charged particle due to an externally applied electric field is equal to the charge multiplied by the magnitude of the field. This force will act to accelerate the particle, while the liquid medium will exert a drag force on it. The maximum velocity of the particle is determined by a balance of these two forces, such that the velocity is independent of the particle size. For a typical water / alcohol based slurry, the zeta potential may be estimated as 60 mV, the viscosity is approximately 1 cP, and the dielectric constant is approximately 48. This results in an electrophoretic mobility of 2.5 X 10^{-10} m^2/Vs, or a velocity of 1.3 μm/s in the typical maximum field of 50 cm/V [23].

Electrophoretic forces have been used to assemble a variety of micron-scale systems into ordered, controlled arrays. The first reported observations of two dimensional crystallization of colloidal particles suspended in a fluid medium under the influence of an applied DC electric field were made by Marcel Böhmer [24]. Böhmer observed clustering of latex spheres on the order of a micron in diameter when a field was applied normal to the substrate. A transparent indium tin oxide (ITO) electrode facilitated the *in-situ* observation of particle clustering with the counter electrode oriented parallel to the substrate (find article and expand). The surface charge on the particles due to the preferential absorption of ions in solution caused the particles to be brought to the surface. A similar experiment resulted in the observation of attractive forces between micron- and nanometer-scale particles [25]. These forces contradicted the expected behavior due to the steric stabilization of colloidal polystyrene and silica in water with the addition of ionic and non-ionic surfactants. An explanation based on the electrohydrodynamic induced fluid flow resulting from charge accumulation near the surface of the electrodes was presented. The attraction of particles in-plane and resulting lateral motion was controlled by tailoring the field strength to achieve a balance between the deposition of particles on the surface and the packing induced by the flow of counter ions. The domain size of the assembled systems could thus be manipulated in a controlled fashion. Additional layers are deposited in a similar fashion and packing faults and point defects are eliminated by the application of an ac current in a process similar to thermal annealing. This method offers promise for tailoring the properties of assemblies of colloidal particles in the submicron to nanometer range and is particularly attractive as an alternative to molecular vapor deposition processes currently used to fabricate nanostructured materials.

1.3 Organization of Thesis

This thesis focuses on three major research themes. The first, presented in Chapter 2, explores the complex surface interactions for a model system of silica particles moving in the vicinity of a sapphire substrate. Electrokinetic measurements are presented for both the particles and the surface in the presence of aqueous electrolytes under a number of different conditions. Particular emphasis is place on the dependence of zeta potential on the crystallographic orientation of single crystalline sapphire substrates. This initial surface characterization work is built upon in Chapter 4, where the electrophoretic deposition device outlined in Chapter 3 is used to manipulate the silica particles in plane using applied electric fields. A summary of experiments conducted using both AC and DC fields is presented and the adhesion of particles near the elec-

trode studied in detail. The use of atomic force microscopy for the characterization of pH changes during EPD is also presented in Chapter 4, while Chapter 3 details the use of a finite element model to predict the field distribution between the electrodes under a range of conditions. Chapter 5 presents a summary of the major findings of the entire body of work presented here and briefly suggests some areas of interest for future related experiments.

Chapter 2: Surface Phenomena

2.1 Introduction

2.1.1 Linear Approximation of Potential for Flat Plate

Dielectric materials acquire a surface charge when immersed in aqueous environments due to the differential absorption of ions present in solution. Ions opposite in sign to the surface charge of the particle are attracted to the surface. The mobility of these counterions in solution also allows them to be uniformly distributed throughout the surrounding aqueous medium such that they reach an equilibrium concentration at distances far from the surface. The concentration of counterions is therefore higher in the immediate vicinity of the particle surface and falls off rapidly towards the bulk solution. This charge arrangement is known as the diffuse electrical double layer and is well characterized according to the spatial distribution of charge first developed by Gouy and Chapman. The model considers a plane surface with a single layer of charge distributed uniformly, giving rise to an electrostatic potential ψ_0. The ions in the diffuse double layer are regarded as point charges immersed in a continuous dielectric medium. The potential distribution is then found by solving Poisson's equation, which relates the local volume density of charge ρ to the divergence of the potential:

$$\nabla^2\psi = -\frac{\rho}{\varepsilon_0\varepsilon_r} \tag{2.1}$$

The volume density of charge is given by a summation over all charged species n_i present in the neighborhood of the surface,

$$\rho = \sum_i n_i z_i e \tag{2.2}$$

where z_i is the valence of ion i and n_i is given by the Boltzmann equation:

$$n_i = n_i^0 \exp\left(-z_i e\frac{\psi}{kT}\right) \tag{2.3}$$

This expression was found by integrating the variation in chemical potential from the surface to a point in the bulk solution, where $n_i = n_i^0$ and $\psi = 0$. Substituting Equation 2.2 and Equation 2.3 into Equation 2.1 gives the complete Poisson-Boltzman equation for a flat surface of constant potential:

$$\nabla^2\psi = -\frac{1}{\varepsilon_0\varepsilon_r}\sum_i n_i^0 z_i e \exp\left(-\frac{z_i e\psi}{kT}\right) \tag{2.4}$$

Calculation of the potential distribution in the diffuse double layer can be simplified by making a linear approximation of the exponential term in the above expression, provided that $z_i e\psi \ll kT$. Expanding the exponential and taking the first two terms then yields:

$$\nabla^2\psi = -\frac{1}{\varepsilon_0\varepsilon_r}\left[\sum_i n_i^0 z_i e - \sum_i \frac{n_i^0 z_i^2 e^2}{kT}\right] \tag{2.5}$$

The first term must them sum to zero according to the electroneutrality condition in the bulk solution and we are left with:

$$\nabla^2\psi = \left[\frac{e^2}{\varepsilon_0\varepsilon_r kT}\sum_i n_i^0 z_i^2\right]\psi = \kappa^2\psi \tag{2.6}$$

The constant κ is known as the Debye-Hückel parameter or Debye constant, after whom the linear approximation above is named, and can be expressed in terms of the ionic strength of the electrolyte, $I = \sum c_i z_i^2$:

$$\kappa = \left(\frac{2000F^2}{\varepsilon_0\varepsilon_r RT}\right)^{\frac{1}{2}}\sqrt{I} \tag{2.7}$$

where c_i is the ionic concentration in mol/L, F is Faraday's constant, and R is the molar gas constant. The solution of the linearized Poisson-Boltzman equation then follows directly by integrating with the boundary condition of a constant surface potential $\psi = \psi_0$ at the flat plate. The potential in the double layer is then given by:

$$\psi = \psi_0 \exp(-\kappa x) \tag{2.8}$$

where x is the linear distance away from the surface into the bulk fluid [26].

2.1.2 Extension to Spherical Particle Interacting with Flat Plate

The preceding analysis can be extended to the case of a spherical particle adhering to a flat plate. The potential energy of interaction can be calculated using the familiar linear (Debye-Hückel) approximation for two constant potential surfaces at low potential. This approach has been applied to surfaces composed of dissimilar materials and is valid for large particle radii such

that $\kappa a > 10$. This condition is well met for a 1.58 μm particle in an aqueous electrolyte with a salt concentration of 10 mM, where the Debye constant is calculated to give $\kappa = 9.89 \times 10^{-9}$ nm. This approach is based on the scaling of the interaction energy per unit area between two semi-infinite flat half spaces for application to arbitrary geometries and can be used to calculate the potential between two dissimilar materials [27]. The total potential is given by:

$$V_{TOTAL} = V_{Rep} + V_{Att} \tag{2.9}$$

where the repulsive potential is:

$$V_{Rep} = \pi\varepsilon_0\varepsilon_f r(\Psi_p^2 + \Psi_s^2)\left[\left(\frac{2\Psi_p\Psi_s}{\Psi_p^2 + \Psi_s^2}\right)\left(\log\frac{1 + \exp(-\kappa D)}{1 - \exp(-\kappa D)}\right) + \log(1 - \exp(-\kappa D))\right] \tag{2.10}$$

and the attractive potential is:

$$V_{Att} = \frac{d}{12D}A_{132}\left(1 + \frac{D}{d+D} + 2\frac{D}{d}\right)\log\frac{D}{d+D} \tag{2.11}$$

where Ψ_p and Ψ_s are the zeta potentials of the particle and substrate, respectively (for a given pH), κ is the Debye length of the charged double-layer (for a given ionic strength), A_{132} is the Hamaker constant calculated for two unique surfaces interacting in a third medium, d is the diameter of the particle, and D is the separation distance between the particle and the flat plate.

2.2 Streaming Potential

The zeta potential, ζ for flat surfaces is calculated from the measured streaming potential, U_S according to the Helmholtz-Smoluchowski equation:

$$\zeta = \frac{\Delta U_S}{\Delta P}\frac{\eta}{\varepsilon\varepsilon_0}\frac{L}{A}\frac{1}{R} \tag{2.12}$$

where $\Delta U_S/\Delta P$ is the slope of the streaming potential curve with increasing applied pressure through the streaming channel, η and ε are the viscosity and permittivity of the electrolyte, L and A are the length and area of the channel, and R is the resistance of the solution in the channel during measurement. The ratio L/A can be approximated by the Fairbrother-Mastin technique

under conditions where the conductivity of the electrolyte is sufficiently high (generally at salt concentrations greater than 1×10^{-3} M) such that surface conductivity may be neglected:

$$\frac{L}{A} = \kappa R \tag{2.13}$$

where κ is the conductivity of the electrolyte. Substituting this expression into Equation 2.12 gives the zeta potential in its more familiar form:

$$\zeta = \frac{\Delta U_S}{\Delta P} \frac{\mu}{\varepsilon \varepsilon_0} \kappa \tag{2.14}$$

This approach was used for all streaming potential measurements presented here.

2.3 Zeta Potential of Silica Particles

2.3.1 Experimental Methods

A ZetaPALS zetameter (Brookhaven Instrument Corporation, NJ) was used for all particle zeta potential measurements. The instrument utilizes phase analysis light scattering to provide an average over multiple particles. Single point measurements were conducted over a full range of pH for dilute suspensions of particles. KNO_3 was used as the background electrolyte for all particle zeta potential measurements and the pH was adjusted with 0.1 M KOH and HNO_3. Fifteen measurements were taken to obtain an average value for each data point, with each measurement consisting of twenty iterations of the fitting routine to obtain a more accurate reading of the phase signal.

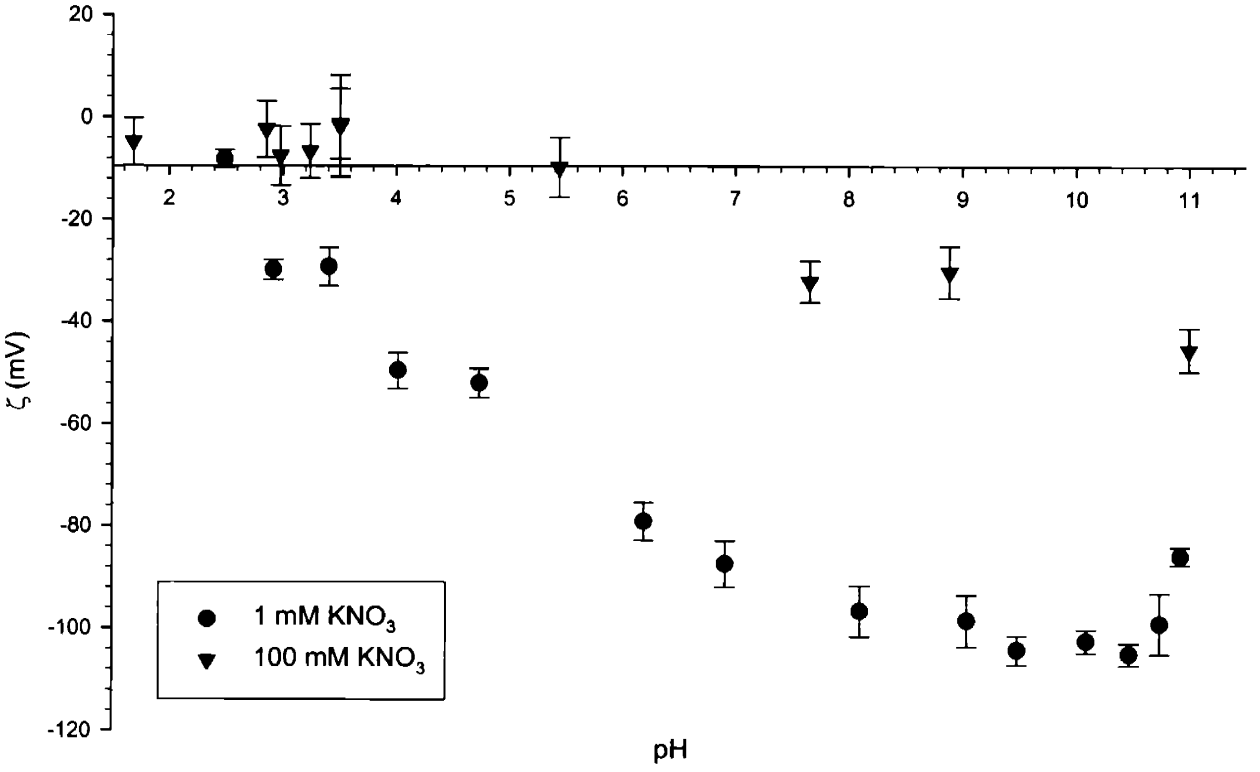

Figure 2.1: Zeta potential as a function of pH for silica particles.

2.3.2 Results

The zeta potential as a function of pH and ionic strength is presented in Figure 2.1 for the 1.58 μm silica particles. The data reveals a well defined iso-electric point (i.e.p.) falling near a pH of 2.5 that is consistent with values reported in other studies [28]. The expected reduction in zeta potential with increasing ionic strength is also observed for the silica particles.

2.4 Surface Preparation and Characterization

Substrates of three different crystallographic orientations used in the following experiments, namely C-plane (0001), A-plane $(11\bar{2}0)$, and R-plane $(1\bar{1}02)$, were obtained from a commercial supplier (Rubicon Technology, Franklin Park, IL) and were melt grown using the heat exchanger method. Two substrates of each orientation, one for each half of the streaming channel, were cut with a rectangular geometry and a thickness of 2 mm from a single sapphire boule and initially polished with an optical finish. Diamond machining was employed to create inlet and outlet ports through which the fluid could flow into and across the channel according to the specifications for the rectangular streaming potential cell. All the wafers used in this study were of single piece construction to avoid any errors associated with variations in the hydrody-

namics of the flow across the surface. The diamond machined slots were also beveled to remove sharp edges at the inlet and outlet and reduce any discontinuities in the flow. A second polishing process was performed on each wafer following machining to achieve an atomically smooth epi-finish. Two additional R plane wafers having a round geometry were obtained from another commercial supplier (St. Gobain Crystals and Detectors) and were used for initial measurements. These wafers were received from the manufacturer with an epi-polish and the slots were machined in a similar fashion without a final re-polish of the surface. The rectangular geometry was later adopted as preferred due to difficulties in providing a pressure seal with the round wafers. A surface treatment was employed for all wafers to ensure that the sapphire surfaces were clean and free of organic and other contaminants prior to measurement of streaming potential. The cleaning procedure consisted of immersing the wafers in a 4:1 bath of sulfuric acid and hydrogen peroxide (commonly known in the microelectronics processing industry as a 'piranha' etch), followed by thorough rinsing in deionized water and blowing dry with nitrogen. X-ray photoelectron spectroscopy was performed both immediately following the cleaning procedure and after all streaming potential measurements were taken to verify that the surfaces had been adequately cleaned and remained so throughout the course of the measurements. It was also confirmed that no silica contamination had occurred at any point during the collection of data. Atomic force microscopy was also used to image the surfaces and confirm that the polishing had rendered them appropriately smooth.

2.4.1 Results

Characteristic AFM images for each crystallographic orientation of the rectangular sapphire wafers following the final polishing and surface cleaning step are presented in Figure 2.2. The RMS roughness achieved on each of the three planes was on the atomic scale and is indicated

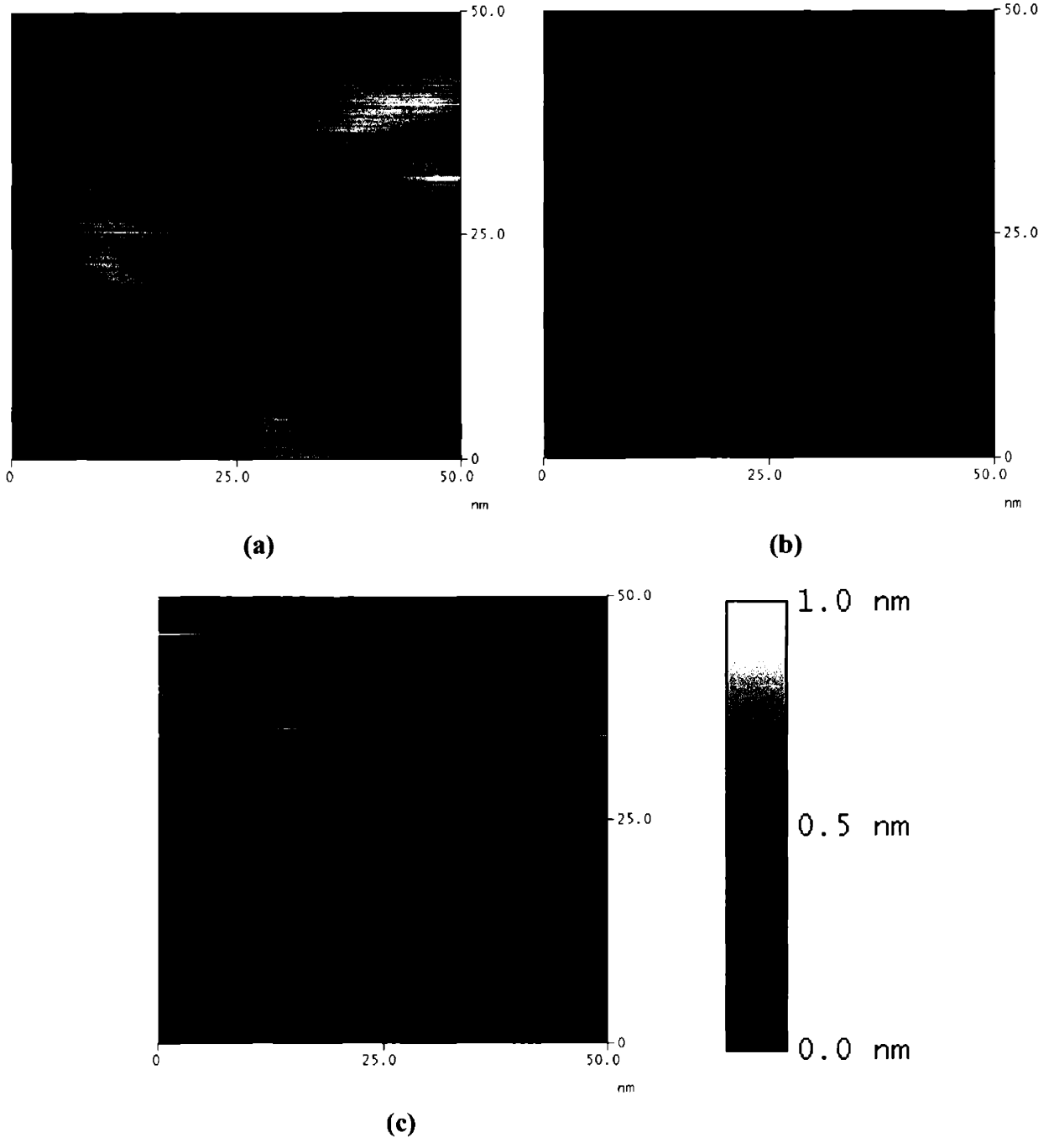

Figure 2.2: Characteristic AFM images of (a) C-, (b) A-, and (c) R-plane sapphire illustrating sub-atomic RMS roughness.

in Table 2.1. Results of a normal incidence XPS survey of a C-plane sample are shown in Figure

Table 2.1: RMS roughness for C-, A-, and R-plane sapphire crystals used in streaming potential experiments

plane (geometry)	RMS roughness
C	1.52 Å
A	0.96 Å
R (rectangular)	0.39 Å
R (round)	0.25 Å

2.3. The survey is dominated by aluminum and oxygen peaks, with trace amounts of sulfur and carbon present on the surface as well. The later is a direct result of the cleaning process used,

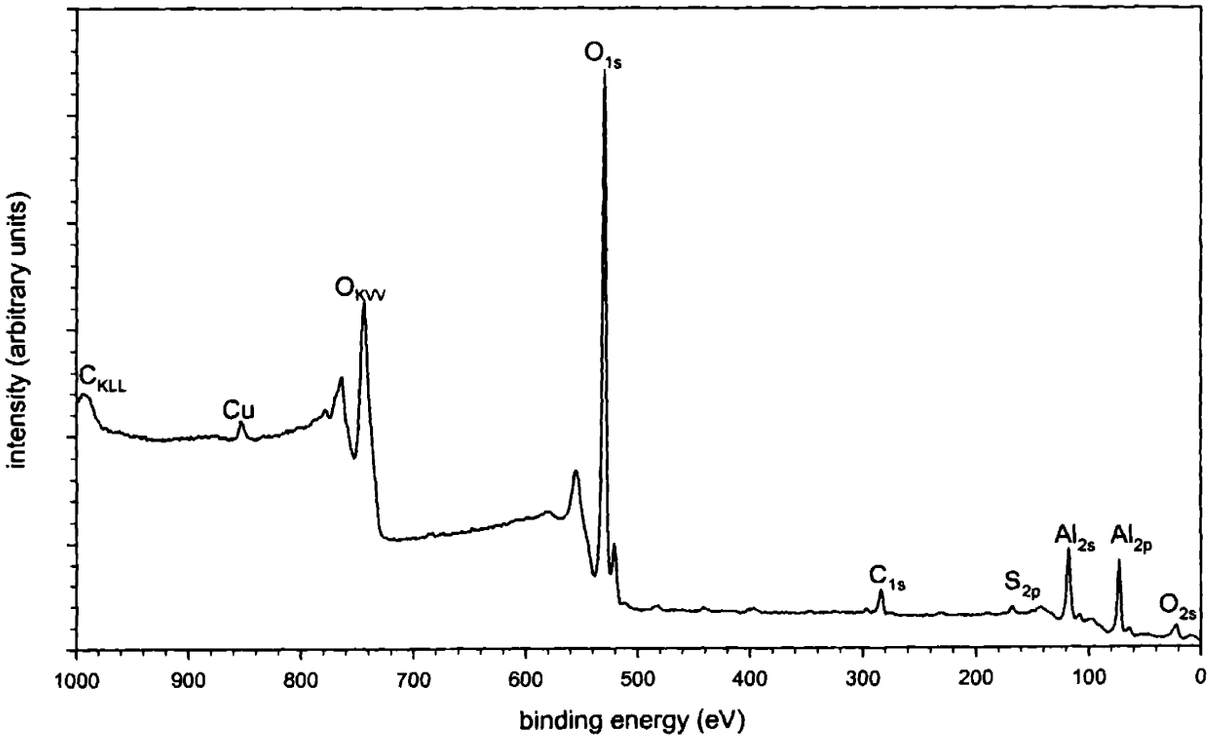

Figure 2.3: Characteristic XPS survey of sapphire streaming potential samples after cleaning in a bath of 4:1 sulfuric acid and hydrogen peroxide.

while the carbon contamination is virtually unavoidable even when handling in a cleanroom environment. It was assured that the height of the carbon peak was substantially reduced after cleaning the samples. The results were nearly identical for all of the crystal planes.

2.5 Zeta Potential of Sapphire Substrates

2.5.1 Literature Review

Comprehensive studies of the experimentally measured zeta potential of planar sapphire surfaces and the corresponding iso-electric point (i.e.p.) are few in number in the available literature. This may stem partially from the extreme cost required to prepare single crystalline samples having a surface area which is adequate to obtain reproducible and fully qualified results. The handful of studies that are available have reported a wide range of values, no doubt resulting from the numerous different measurement techniques and surface preparation methods used. Only recently have well designed commercial instruments appeared on the market, capable of producing reliable data using standard and proven methods. Larson, *et. al.* developed a streaming potential apparatus to study C-plane surfaces [29], while other authors have made use of a modified electro-osmotic technique to evaluate the zeta potential of rod-shaped sapphire fibers [30][31]. Other studies using scanning probe microscopy are not capable of measuring the zeta potential over the full pH range and present only a single value for the i.e.p. A surface force apparatus was used in two separate investigations of the i.e.p. of C-plane sapphire crystals [32][33], while atomic force microscopy was employed by two other authors to study macroscopic sapphire surfaces without mention of the orientation of the samples [34][35]. More recent data presented by Franks and Meagher evaluated the zeta potential as a function of pH for four different crystallographic orientations of sapphire wafers [36]. This work was conducted with two different electrolytes at a single ionic strength of 1 mM. Though some variation in the i.e.p. as a function of orientation was observed, the authors conclude that the reproducibility of the techniques used (particularly the atomic force microscopy method) rendered these differences insignificant. Franks and Meagher also present an excellent summary of the various measurements of sapphire i.e.p., both by streaming potential and scanning force microscopy. An additional study not summarized there was carried out by Sasaki and co-workers using the plane-interface technique to measure the zeta potential of C-plane sapphire plates as a function of pH. The reported i.e.p. in this case occurred at pH = 5.6 [37].

We present here a comprehensive measure of the pH-dependent zeta potential of planar sapphire substrates for C-plane (0001), A-plane $(11\bar{2}0)$, and R-plane $(1\bar{1}02)$ wafers [100]. The zeta potential is measured at several different ionic strengths for each crystal plane, and the R-plane substrates are evaluated using two different electrolytes. A streaming potential technique was selected for the measurement of i.e.p. due to its direct correlation to ion adsorption at surface sites of the sapphire crystal. The streaming potential technique remains the most accurate method for determining i.e.p. and also allows the measurement of zeta potential over the full pH range. The commercial streaming potential analyzer (BI-EKA, Brookhaven Instruments Corporation, Holtsville, NY) used for all measurements in this work was identical in design to an instrument that has been demonstrated in the literature to produce extremely accurate and reproducible zeta potential data on a variety of surfaces [38][39][40][41]. This technique provides a complete picture of the sign and magnitude of the surface potential of the substrate, thus giving information on the exact pH at which the surface moves from a positive to a negative charge. Careful consideration is given to the preparation of the commercially polished surfaces used in this work. This was done primarily to eliminate the deleterious effects of silica contamination alluded to by other authors [36]. The removal of this and other organic and inorganic contaminants was closely monitored using XPS and AFM. A standard cleaning procedure used in microelectronics was employed to render the surface sufficiently clean for the direct measurement of zeta potential.

2.5.2 Structure of Sapphire

Large, defect-free, synthetic sapphire crystals have been commercially grown using the heat exchanger method for several decades[42][43]. The most stable form of alumina, the α-Al_2O_3 single crystal has a corundum structure with a hexagonal unit cell composed of two molecules and possessing rhombohedral symmetry of space group D_{3d}^6 . The unit cell, shown in Figure 2.4, contains 12 Al^{3+} and 18 O^{2-} ions with a = 4.76 Å and c = 12.99 Å [44]. The oxygen anions are arranged in a close-packed array, with aluminum cations occupying 2/3 of the available octahedral interstitial sites. This bulk structure results in each Al^{3+} being surrounded by six O^{2-}, while the coordination number of the oxygen sites is four. The crystallographic orientations of

interest studied in the present work are identified by the colored planes in Figure 2.4. Considering first the easiest orientation to visualize, the C- (or basal) plane is oriented parallel to the close-packed array of oxygen sites and has been well-characterized in the literature. It is immediately apparent from the figure that several unique C-plane surfaces can be realized depending on the manner in which the crystal is cleaved. The termination of the surface of the crystal is paramount to understanding the adsorption of potential determining ions and other surface active species. The temperature-dependent surface reconstruction will also dictate the arrangement of surface ions, such that the total energy of the surface is minimized by the lateral motion of ions within the surface plane. The C-plane surface has been confirmed by both experimental [45][46][47][48][49][50] and theoretical [51] studies to possess a 1×1 unreconstructed surface identical to the bulk crystal up to temperatures of approximately 1370 K, with various other

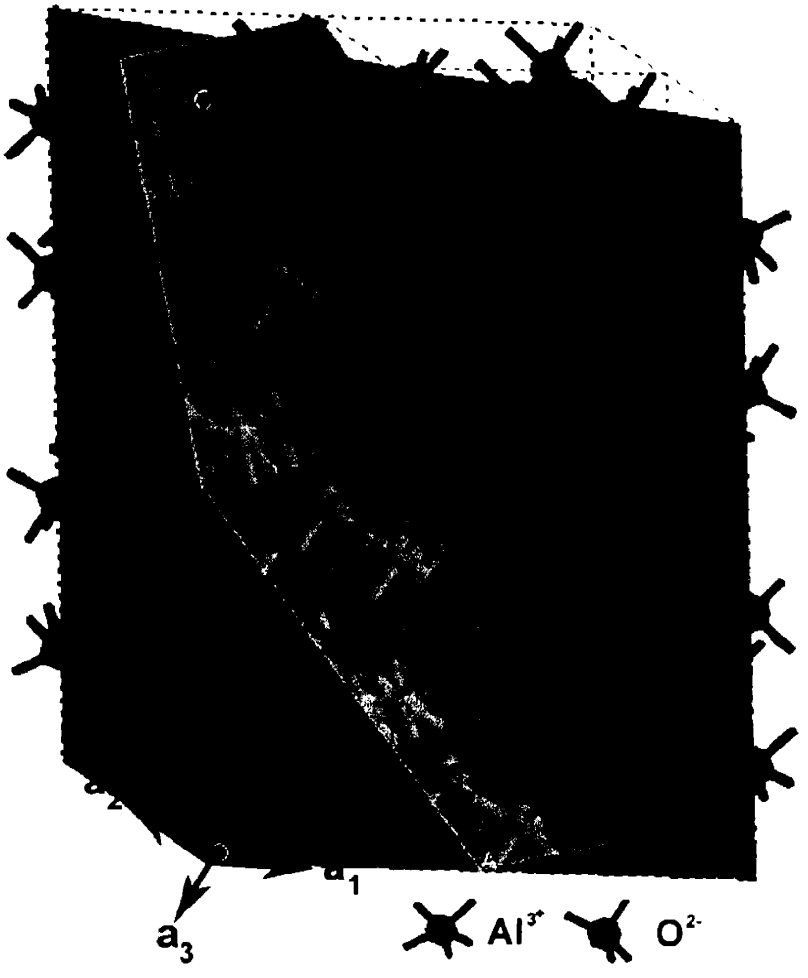

Figure 2.4: Sapphire unit cell showing crystallographic orientations studied: C-plane (red), A-plane (green), and R-plane (yellow).

reconstructions resulting from annealing at more elevated temperatures [52][53][54]. The existence of both oxygen [55] and aluminum C-plane terminated surfaces [56] has been reported in the literature. Other studies have suggested the possible existence of a surface consisting of mixed oxygen and aluminum sites. The majority of this work was conducted under UHV conditions with native sapphire surfaces where care was taken to avoid exposure to moisture or surface contaminants. These experiments [57][58] coupled with more recent theoretical evidence based on density functional theory in the local density approximation (DFT-LDA) calculations [51] confirm that the native C-plane surface is indeed terminated in a monolayer of aluminum cations under UHV. This conclusion is based on the highly stable nature of the electrically neutral Al-O-Al stacking sequence that occurs for this configuration.

The presence of Al^{3+} at the surface of the native C-plane crystal results in a reduction in coordination of these cations relative to the bulk structure. This leads to an energetically favorable relaxation of the surface aluminum cations towards the three coordinating oxygen anions below. The phenomena has been studied in the literature for native unhydroxylated C-plane crystals using advanced computational techniques. Up to eighteen alternating Al^{3+} and O^{2-} layers of the surface structure are modeled in this work as a multi-layer slab. Verdozzi, et. al. report the relaxation of the surface Al^{3+} layer by as much as -87.4% [59], with the minus sign denoting a relaxation into the plane of oxygen anions immediately below this surface layer such that the aluminum becomes nearly co-planar with the O^{2-}. Other authors have reported slightly lower values on the order of -85% to -86% using similar computational methods [51][60][61][62], though the calculations have been shown to be somewhat sensitive to the specific selection of technique and model parameters [63]. These models also show a slight shift of the oxygen layer towards the surface such that the co-planar oxygens are displaced by on the order of +3.0%. Much less dramatic shifts occur on various planes of subsurface atoms until the relaxations are eventually damped out in the bulk.

Limited work concerning the reconstruction and termination of the native A- and R-plane surfaces has been presented in the literature, though a few studies do tackle these more complicated structures. Guo, Ellis, and Lam reported termination of the R-plane surface with a single layer of O^{2-} [56], though more recent experimental evidence has not been provided. This conclusion was again based on the reduction in energy afforded by the oxygen termination but may also

result from the hydroxylation of the surface as was reported for the (0001) orientation, discussed in Section 2.6.3. Reconstruction studies of the R-plane sapphire surface have not been reported. The A-plane surface, on the other hand, is known to exhibit a number of reconstructions upon annealing, with the lowest temperature (3×1) structure occurring at 900 K [64]. No work concerning the termination of the unreconstructed A-plane surface is available in the literature.

The introduction of native, aluminum terminated C-plane sapphire crystals to an aqueous environment has been shown by many authors to result in complete hydroxylation of the surface at water vapor pressures as low as 1 torr [65][66][67][68]. It becomes necessary to adapt the discussion of native sapphire surfaces presented in Section 2.5.2 to reflect this phenomenon. Additional spectroscopy work by Eng, *et al.* using a synchrotron x-ray source, confirms that the hydration results in termination of the C-plane sapphire surface with a layer of surface hydroxyl groups even at temperatures as low as 300 K [69], a schematic of which is shown below in Figure 2.5.

2.5.3 Experimental Methods

A commercial streaming potential analyzer (BI-EKA, Brookhaven Instruments Corporation, Holtsville, NY) was used for all measurements in this work. The instrument is comprised of a rectangular cell which holds the sample and forms the streaming channel, a mechanical pump which provides a pressure flow of an electrolyte solution held in a reservoir, electrodes positioned at either side of the channel, and a control system and data collection software. The streaming channel is formed by two flat parallel plates separated by a polytetrafluoroethylene (PTFE) spacer with the channel height specified by the thickness of the spacer and equal to 0.254 mm. A mechanical clamping mechanism provided a pressure seal and ensured that a continuously ramp-

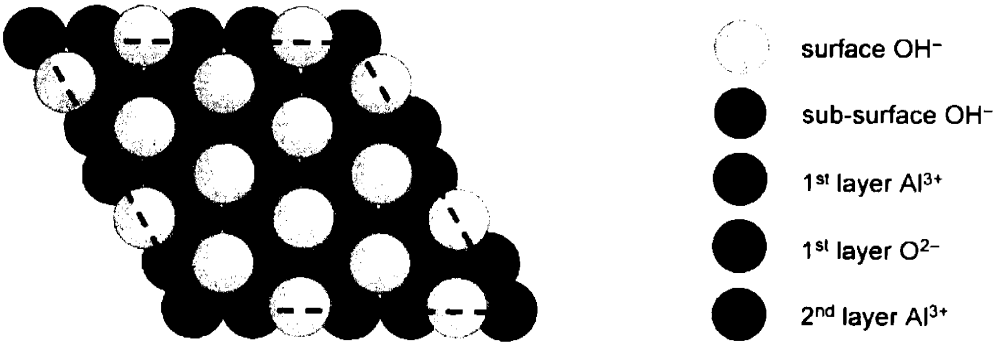

Figure 2.5: Schematic of hydroxyl terminated C-plane surface. The projection of the multiple unit cells is shown by the dotted line. The relative scale of the ionic radii is exaggerated for clarity.

ing pressure flow could be maintained. The geometrical and other details of this so-called rectangular cell have been presented elsewhere [70][71][72]. The potential difference between the two reversible Ag/AgCl electrodes was recorded as the pressure was slowly ramped at a rate of 100 Pa/s. Each measurement cycle was characterized by an initially non-linear dU/dP curve until the flow through the cell reached steady-state, after which the curve became linear for the duration of the experiment. The electrodes were prepared by plating and their reversibility verified by ensuring that the initial measured potential in absence of any pressure flow (the asymmetric potential) was less than 0.1 mV. Replating of the electrodes was undertaken as necessary whenever the reproducibility of the measurements became inadequate. The electrodes were ion selective for Cl^- ion and a chloride salt was therefore used in all experiments as the background electrolyte. The linear portion of the dU/dP curve was then manually fit to determine the measured value of the streaming potential at each pH and ionic strength.

Reproducibility of the streaming potential data was critical to observing a systematic shift in the i.e.p. as a function of crystallographic orientation of the substrate. Streaming potential measurements were taken at three different time periods over the course of a year using the same samples and procedures. Overlapping data was collected during each period to verify that the data was appropriately reproducible. Two sets of measurements were performed on the R-plane wafers, with the round geometry wafers used for the first set and the preferred rectangular geometry used for the second. The rectangular geometry was used for all measurements on A- and C-plane substrates. The majority of measurements were conducted with a background electrolyte of analytical grade KCl, though additional data was taken with the R-plane wafers using analytical grade $(CH_3)_4NCl$. The pH adjustment was performed by the addition of 0.1 M KOH or HCl to the solution in the constantly stirred reservoir. Eight measurements were performed at each data point corresponding to a single pH and ionic strength, with the direction of flow alternated between adjacent measurements to ensure that no polarization of the electrodes occurred. The measurements at each condition were averaged and values which exceeded the mean by one standard deviation were removed.

2.5.4 Results

The results of streaming potential measurements performed on R-plane wafers in the presence of a KCl electrolyte at various ionic strengths are shown in Figure 2.6. Data from experiments using both the round and rectangular shaped wafers are plotted together and are independent of the sample used and the time at which the experiments were performed. The data indicate a characteristic reduction in the magnitude of the zeta potential at all values of pH with increasing ionic strength, as would be expected due to the collapse of the Debye layer caused by the addition of salt. Experimental results using a $(CH_3)_4NCl$ electrolyte are also shown for com-

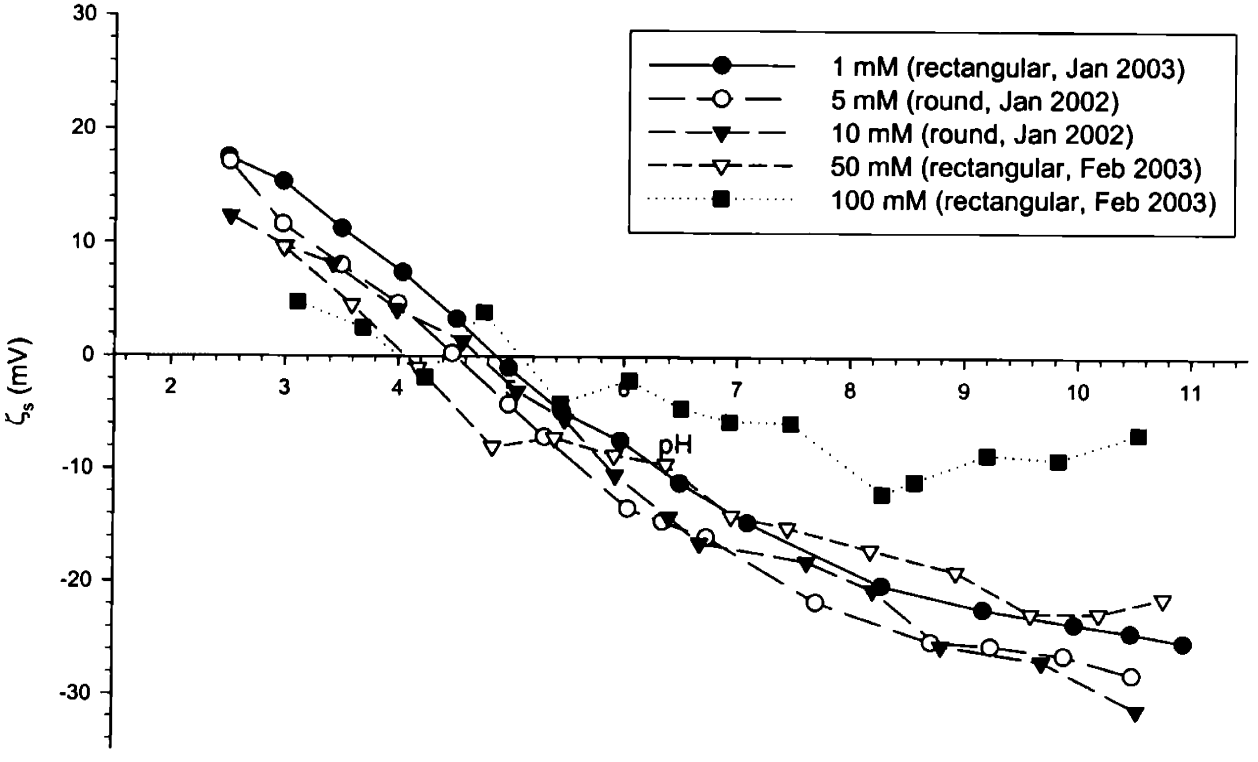

Figure 2.6: Zeta potential as a function of pH for the R-plane substrates in the presence of a KCl electrolyte over a range of ionic strengths. The results are observed to be independent of the sample geometry and the time at which the experiment was conducted.

parison in Figure 2.7. The i.e.p. of the R-plane wafers is tightly centered around a pH of 4.5 for both electrolytes at all ionic strengths. Results of identical experiments performed on the A- and

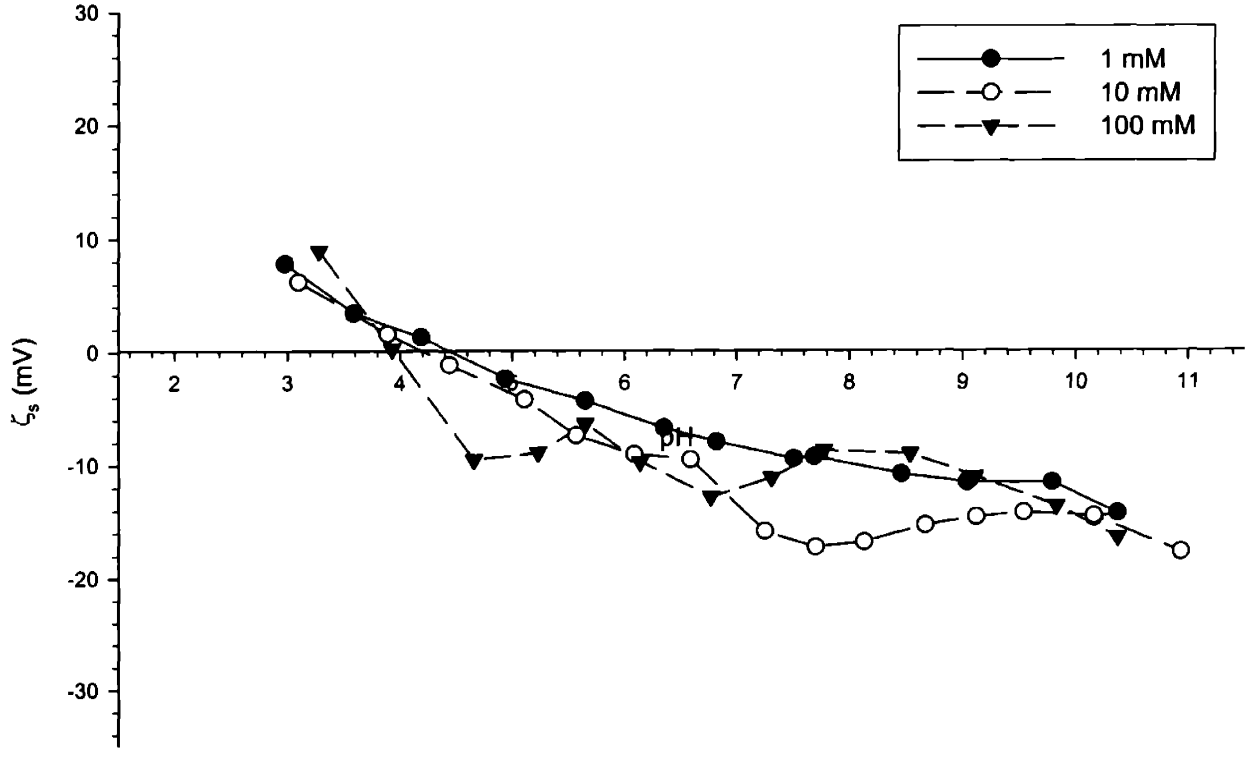

Figure 2.7: Zeta potential as a function of pH for the R-plane substrates in the presence of a $(CH_3)_4NCl$ electrolyte.

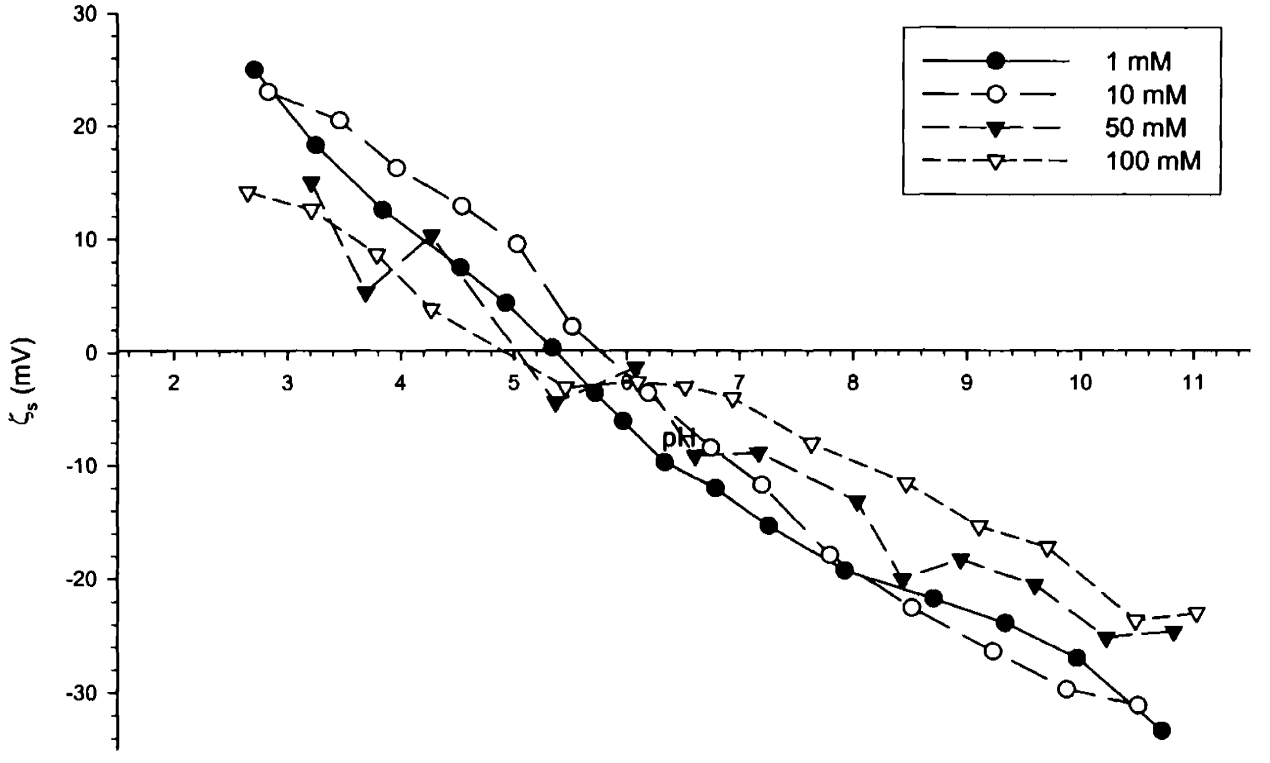

Figure 2.8: Zeta potential as a function of pH for the A-plane substrates in the presence of a KCl electrolyte over a range of ionic strengths.

C-plane wafers are presented in Figure 2.8 and Figure 2.9, respectively. Data at three different

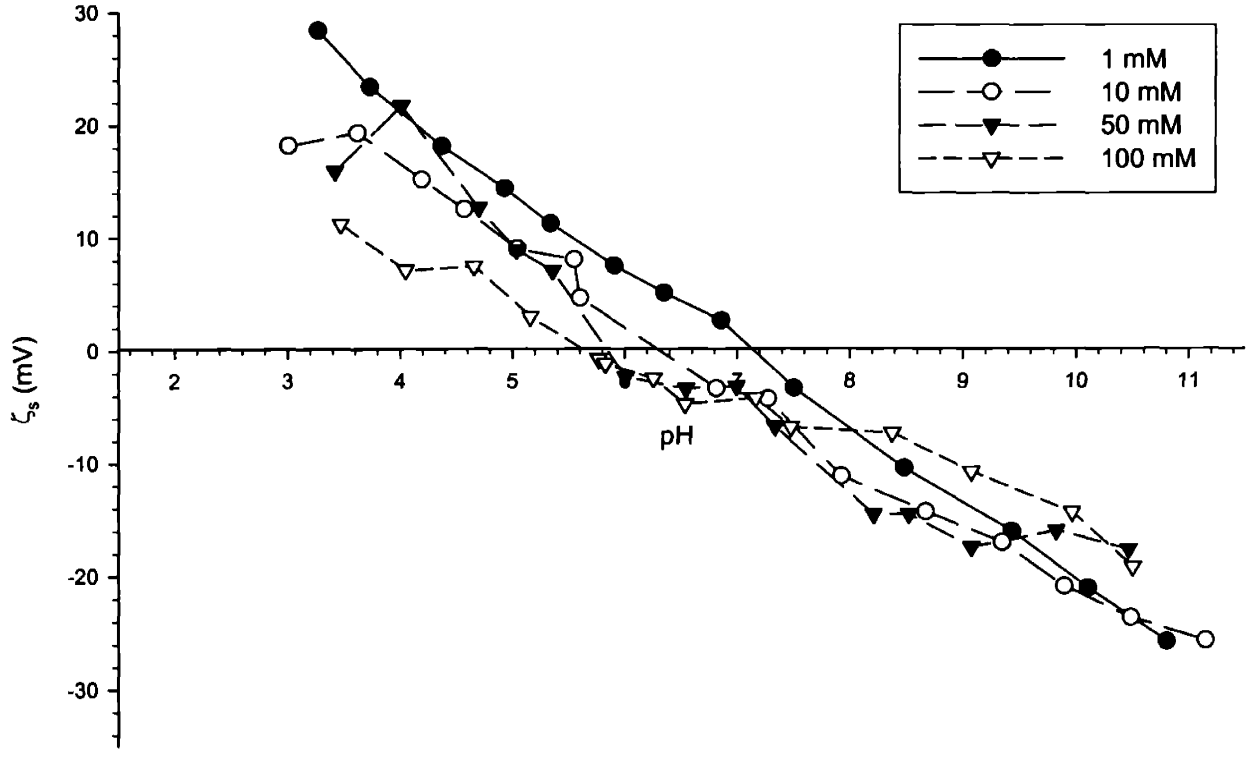

Figure 2.9: Zeta potential as a function of pH for the C-plane substrates in the presence of a KCl electrolyte over a range of ionic strengths.

ionic strengths are presented for these orientations. The data for the A- and C-plane wafers is also quite consistently centered around two distinct and well-defined iso-electric points. The shift in i.e.p. as a function of crystallographic orientation is illustrated quite dramatically in Figure 2.10, where the pH-dependent zeta potential is plotted for all crystal planes in the presence of a 10 mM KCl electrolyte. The error bars, omitted for simplicity in the plots containing data at multiple ionic strengths, are shown in this figure. The increase in error observed at higher ionic strengths and in strongly acidic or basic electrolytes is due simply to the dependence of the zeta potential as measured by the streaming potential technique on conductivity of the solution.

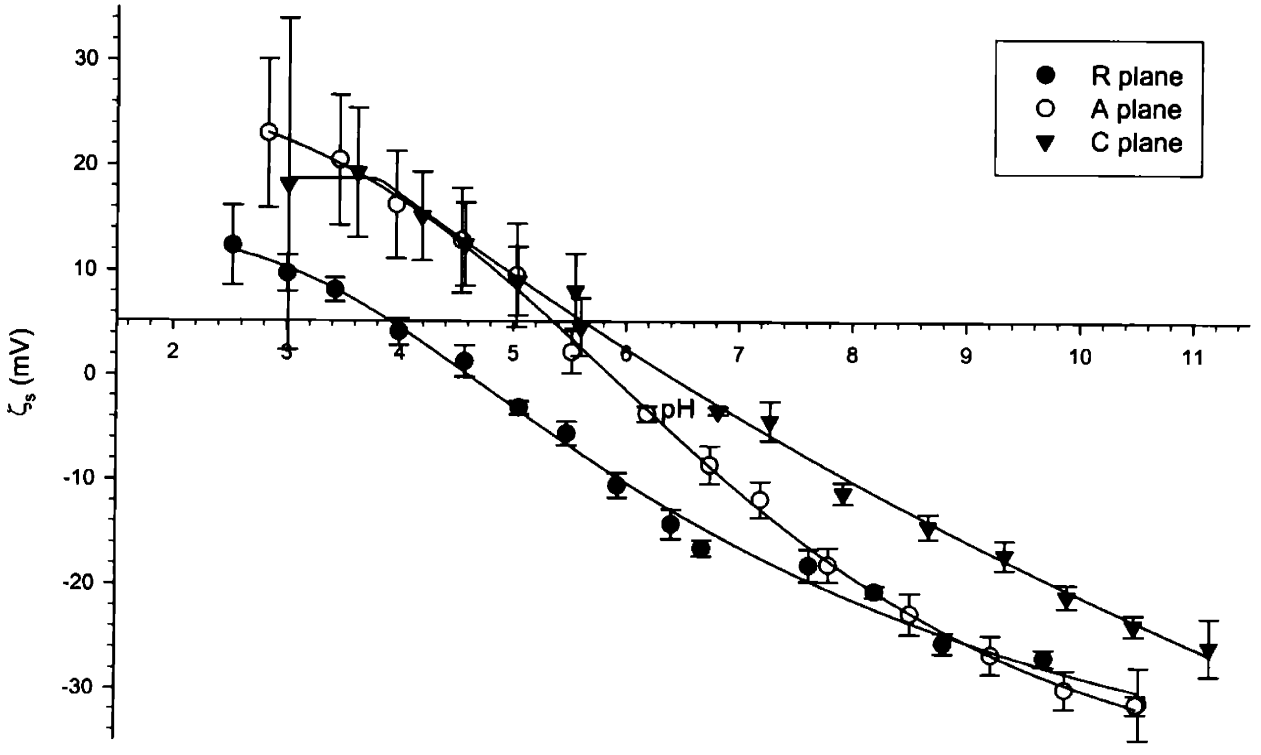

Figure 2.10: Results of streaming potential measurements conducted in a 10 mM KCl solution, replotted with error bars. All orientations are shown to illustrate dramatic shift in i.e.p. and increase in acidity of R-plane surface.

2.5.5 Comparison with Particles

The zeta potential as a function of pH of the Sumitomo AKP-30 particles is shown in Figure 2.11. The measured iso-electric point which occurs at pH = 8.0 is consistent with values reported in the literature for both similar and identical dispersed powders [73][74][75]. Equivalent measurements on the single crystalline AA-2 powder revealed a much lower i.e.p. near pH = 3.8. The dramatic increase in acidity of the surface of the Sumicorundum powder follows logically from our experimental observations of a greatly reduced i.e.p. for the three planes of sapphire studied. Though the exact processing history of the AA-2 powder is proprietary, it is assumed that the final high temperature heat treatment is followed by a dehydroxylation step, presumably by heating in a moisture free environment to drive off adsorbed surface hydroxyl groups followed by rapid cooling to prevent readsorption. It is also significant that the same surface acidity may be achieved with the very high surface area single crystalline powder, indicating that the low i.e.p. measured by streaming potential for flat sapphire plates is not simply a function of the number of surface sites available for adsorption of hydroxyl groups. The i.e.p. at pH = 3.8 is similar to that of the R-plane sapphire wafers. A scanning electron micrograph of a single crystal of

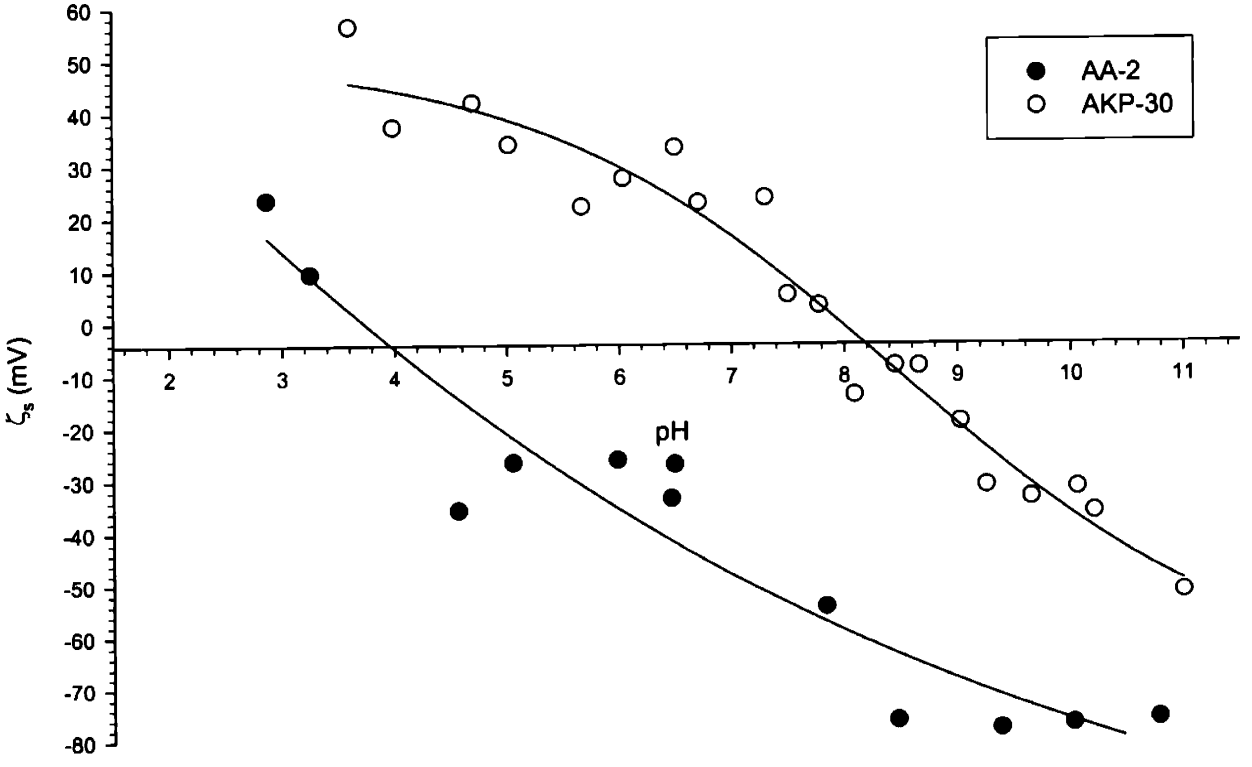

Figure 2.11: Zeta potential of Sumitomo AKP-30 and single crystalline Sumicorundum AA-2 as measured by phase analysis light scattering. The trendlines are provided simply to guide the eye.

Sumicorundum is shown in Figure 2.12 (a), where the shape of the crystal clearly mimics the calculated Wulff shape shown in Figure 2.12 (b). Other crystallographic planes not studied in the present work are also indicated in the figure. The dominance of the R-plane orientation may account for the similarity between the i.e.p. of the powder and that of the R-plane sapphire wafers, without specific knowledge of the acidity of the surfaces having other surface structures not studied here.

2.6 X-Ray Photoelectron Spectroscopy of Sapphire Substrates

The change in acidity of the sapphire surfaces studied can be validated through indirect measurement of the shift in chemical state resulting from the transfer of charge between the substrate and a thin metal film. XPS has been established as the tool of choice for probing the electronic structure of the surface due its ability to reveal information about core-level transitions without producing chemical changes in the surface layers. The ionicity of various metal oxide surfaces has, for example, been studied using Auger peaks during XPS to reveal differences in the local atomic charge on the oxygen due to changes in the nature of the chemical bonding [76]. One significant problem in applying this technique to the study of insulators has been the need for various charge neutralization techniques in order to discern sensitive chemical information about the surface under investigation. Wagner first proposed the simultaneous measurement of Auger and photoelectron peak shifts and their comparison [77], thus allowing any charge correction that may

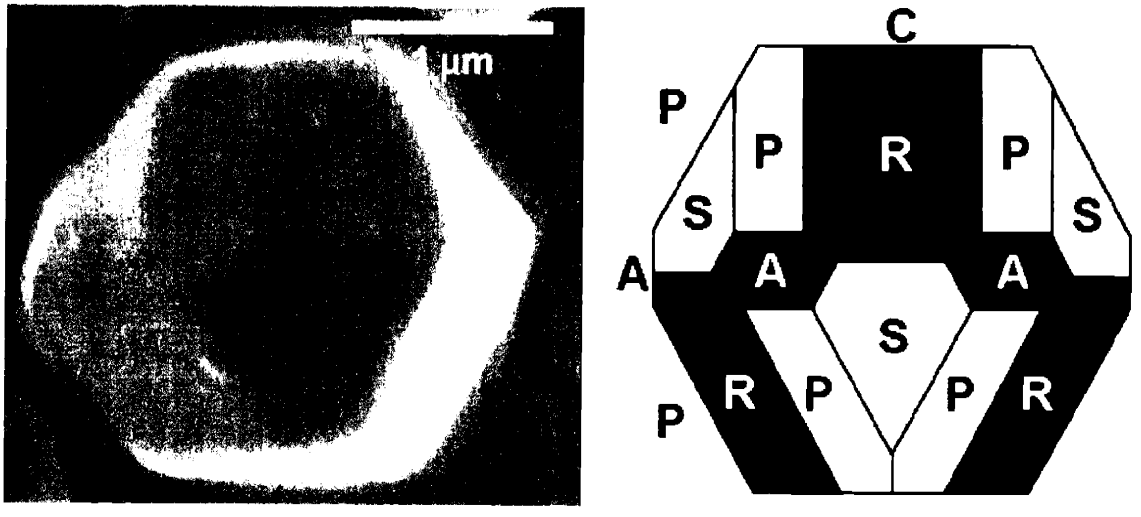

(a) (b)

Figure 2.12: Scanning electron micrograph **(a)** of a single crystal of Sumicorundum AA-2, showing striking resemblance to Wulff shape **(b)**, dominated by faces exhibiting an R-plane orientation.

have been employed to simply cancel out. This so-called Auger parameter could then be used to demonstrate shifts in line energies due to variations in the electronic state transitions of surface atoms. One minor difficulty arises in the definition of the Auger parameter, leading to the measurement of negative values on an otherwise absolute energy scale. This problem was overcome by defining a modified Auger parameter (MAP) [78], α^* such that:

$$\alpha^* = \alpha + h\upsilon = E_{k,\,Auger} + E_{b,\,photoelectron} \qquad \textbf{(2.15)}$$

where α is the Auger parameter and $h\upsilon$ is the energy of the incident X-ray. Here the energy of the Auger electron line is given as kinetic energy while the photoelectron transition is normalized on a binding energy scale.

This technique has recently been applied to the investigation of the electronic structure of the interface between a thin layer of palladium and sapphire substrates having the same orientation as those used in the present work [79]. The interest here was in the size of the Pd domains during deposition, hence elucidating information about the growth mode on the sapphire. Ealet, *et al.* performed a similar study of the alumina-nickel interface to reveal information about the ionic character of the bonding [80]. Here we take a reverse approach, using a thin layer of metal deposited on the surface to act as a test base to determine the acidity of the sapphire substrates as a function of crystallographic orientation.

2.6.1 Experimental Methods

Iridium was selected for a MAP study of chemical state shifts as a function of orientation of the sapphire substrate due to the occurrence of both photoelectron and Auger peaks that did not overlap with those of oxygen, aluminum, or carbon. An electron beam evaporator was used to deposit a thin film of iridium approaching a monolayer. This technique of iridum deposition was selected in order to yield as uniform a film as possible for all samples so as to eliminate effects of thickness reported by other authors. Angle resolved spectroscopy at 30° and glancing (70°) incidence was performed using non-monochromated Mg-Kα excitation (1486.6 eV) from a dual anode Mg/Al x-ray source at a base pressure on the order of 2.5×10^{-6} Pa. The measurement of spectra at multiple angles rendered the thickness of the film insignificant as an analysis parameter since the penetration depth of the excitation energy and hence the surface information is a function of the angle of incidence. The Ir_{NNN} Auger peaks and $Ir_{4f_{7/2}}$ and $Ir_{4f_{5/2}}$ photoelectron peaks

corresponding to the outermost core level transition giving a sufficiently strong signal were quantified with high resolution scans.

2.6.2 Results

Detailed plots of the XPS spectra centered around the iridium photoelectron and Auger peaks are shown in Figure 2.13 for the 30° incidence experiment. The Auger peaks for all three orientations of sapphire are nearly identical while a dramatic shift of over a half an eV is apparent in the photoelectron peaks. The C-plane surface peak was observed to occur at the lowest binding energy with the highest binding energy peak corresponding to the R-plane sample. The calculated

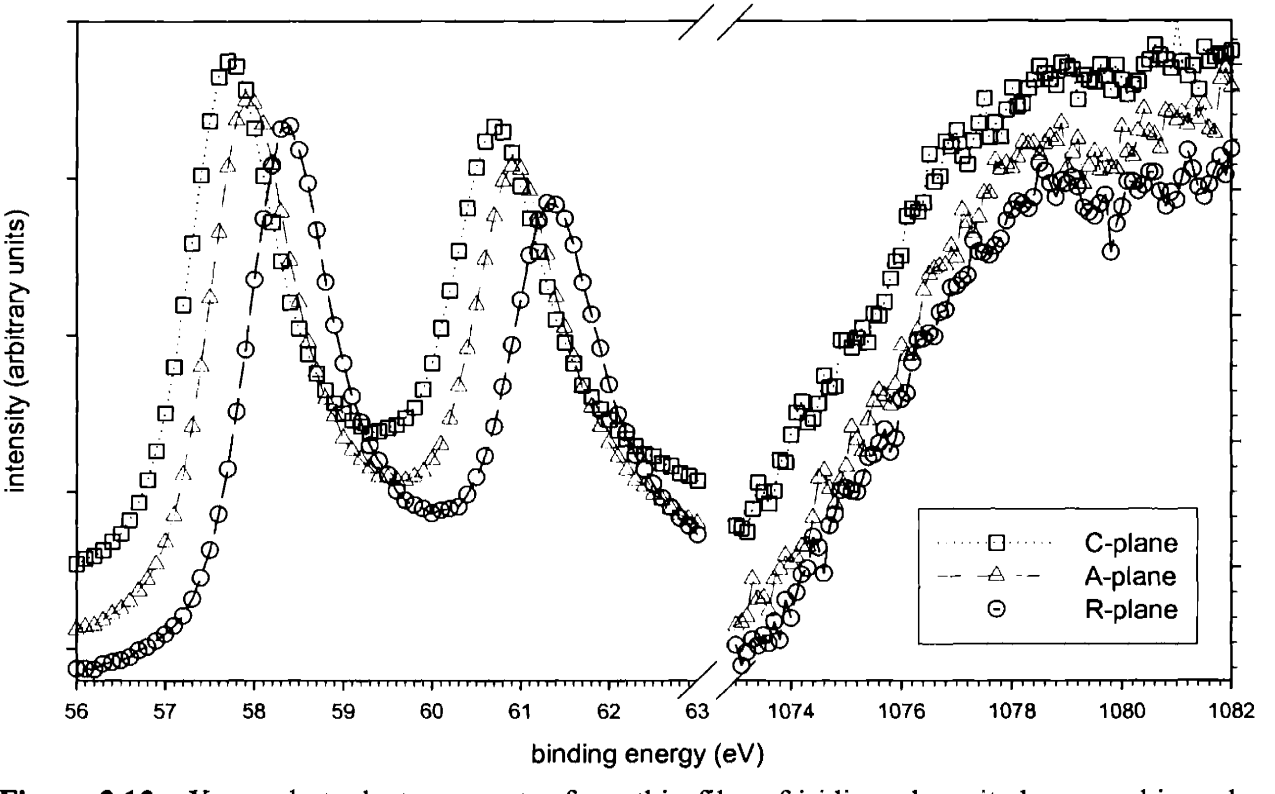

Figure 2.13: X-ray photoelectron spectra for a thin film of iridium deposited on sapphire substrates of three different crystallographic orientations. The photoelectron peaks are shown at left while the Auger peaks are shown at right.

MAP at both angles of incidence is summarized in Table 2.2 for the three substrates, revealing a

Table 2.2: Modified Auger parameter for all substrates as a function of angle of incidence of the Mg-Kα radiation.

angle of incidence	R-plane	A-plane	C-plane
30°	234.479 eV	234.054 eV	233.839 eV
70°	234.625 eV	234.606 eV	234.535 eV

similar (though less dramatic) shift spanning 0.09 eV for the spectra measured at 70° incidence. The energy required to remove a core electron from atoms contained within the iridium film is greatest for the monolayer deposited on the R-plane substrate. Considering a simple electrostatic model, it follows that this energy should increase with increasing positive net atomic charge. The effect of the more acidic R-plane substrate is to more strongly bind the outermost electrons of iridium. The A- and C-plane substrates exhibiting a higher i.e.p. have a less dramatic effect on the iridium MAP. These less acidic surfaces will consequently bind the outer most iridium electrons less strongly, providing further validation for the observed shift in i.e.p. for the three different orientations of sapphire.

2.6.3 Discussion

Both the results of the streaming potential experiments and the MAP analysis of the A-, R-, and C-plane sapphire substrates demonstrate a change in the acidity of the crystals as a function of crystal orientation. One possible explanation for the observed change in acidity on different sapphire planes can be deduced by considering the number density of adsorption sites available on the surface. It is reasonable to assume that the number of adsorbed ions, and hence the total charge on the surface, would be directly correlated to the number of hydroxyl sites on these very low surface area substrates. A simple calculation of this parameter for the three surfaces under consideration reveals no correlation between the site density and the observed trend in

acidity, as shown in Table 1. The critical property to understand is then not the density of adsorp-

Table 2.3: Number density of hydroxyl adsorption sites for each crystallographic orientation.

Crystal Plane	Surface OH^- Density
C	9.0 sites/nm^2
A	14.56 sites/nm^2
R	12.15 sites/nm^2

tion sites but rather how strongly acidic each surface is. This behavior will depend on the structural and electronic characteristics of the surface which are responsible for the adsorption of potential determining ions.

It was assumed based on evidence available in the literature (see Section 2.5.2) that the surface of the C-plane wafers used in the aqueous streaming potential experiments presented here

was indeed hydroxyl terminated, a schematic of which is shown again for comparison in Figure 2.14 (a). The figure shows a sub-surface layer of Al^{3+} directly beneath the close-packed surface layer of OH^-, along with two additional subsurface planes of O^{2-} and Al^{3+}. Each sub-surface Al^{3+} is coordinated by a total of six anions on the C-plane surface, with three surface OH^- due to the hydroxylation and three sub-surface O^{2-} originating from the bulk structure. The same assumption of a hydroxyl terminated surface at room temperature was adopted for the R- and A-plane wafers in absence of any more conclusive experimental evidence to the contrary. A schematic of these structures showing the upper-most hydroxyl plane and subsurface ions is presented in Figure 2.14 (b) and (c). One important distinction between these surfaces and that of the C-plane crystal stems directly from the differences among the three surface structures. The A- and R-

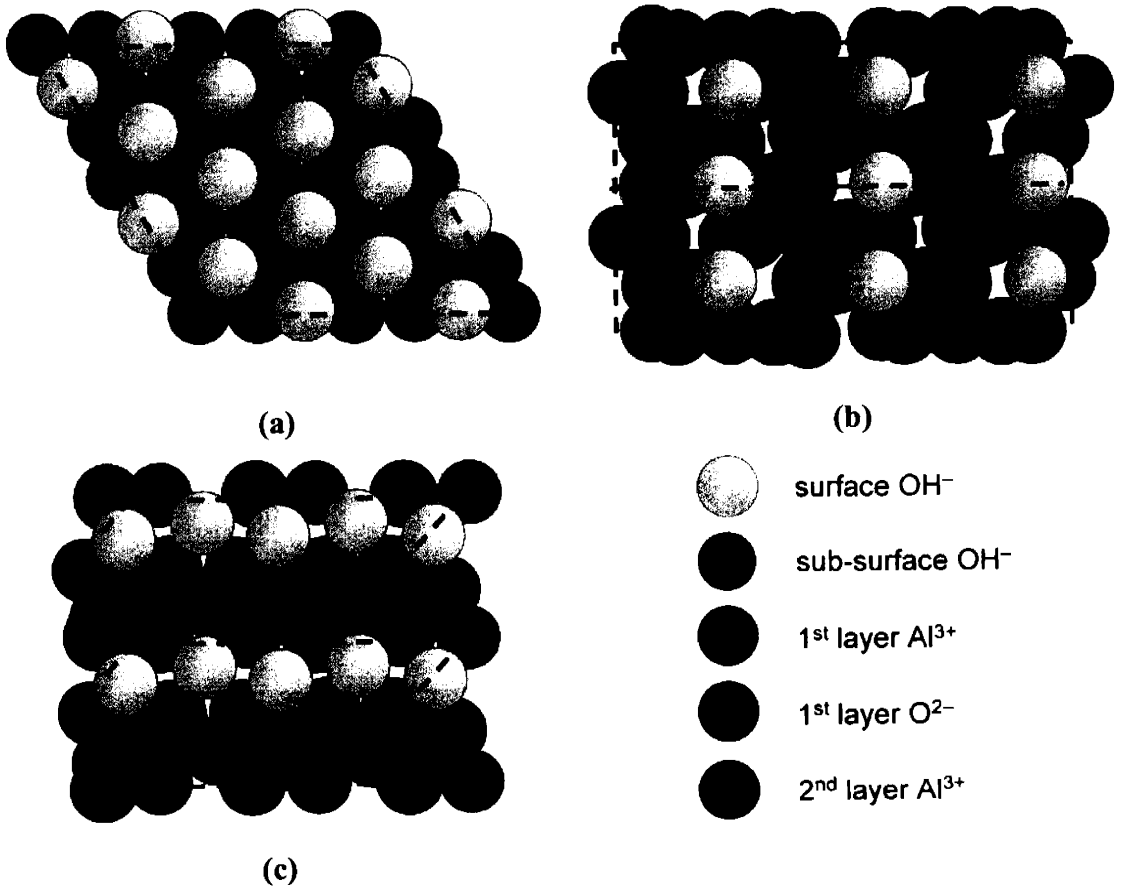

Figure 2.14: Schematic of hydroxyl terminated surfaces, showing surface hydroxyl groups for the **(a)** C-plane, **(b)** A-plane, and **(c)** R-plane crystallographic orientations. The projection of the multiple unit cells is shown by the dotted line. The relative scale of the ionic radii is exaggerated for clarity.

plane surfaces may be thought of an off-axis rotation of the (0001) orientation, as is depicted schematically in Figure 2.15. Here only two hydroxyl groups are located immediately at the surface, with the third OH^- set back due to the rotation. This may mean that not all three oxygen positions are available for hydroxylation, leading to a difference in surface composition of the A-, R-, and C-plane crystals.

An additional consideration is the position of the sub-surface aluminum cations relative to the OH^- layer in the hydroxylated sapphire crystal. A relaxation of the sub-surface aluminum cations has been observed for hydroxylated C-plane crystals [69], where the sub-surface aluminum cations are normally found to lie in two distinct planes due to the energetically favorable puckering of the Al^{3+} occupying the octahedral sites. The resulting relaxed structure shows a 53% reduction in the inter-layer spacing between the two planes of Al^{3+}, causing an extension of bonds between these sub-surface ions and the hydroxyl surface layer. This relaxed surface layer has, in fact, been compared by Eng and co-workers to the gibbsite structure, illustrated schematically in

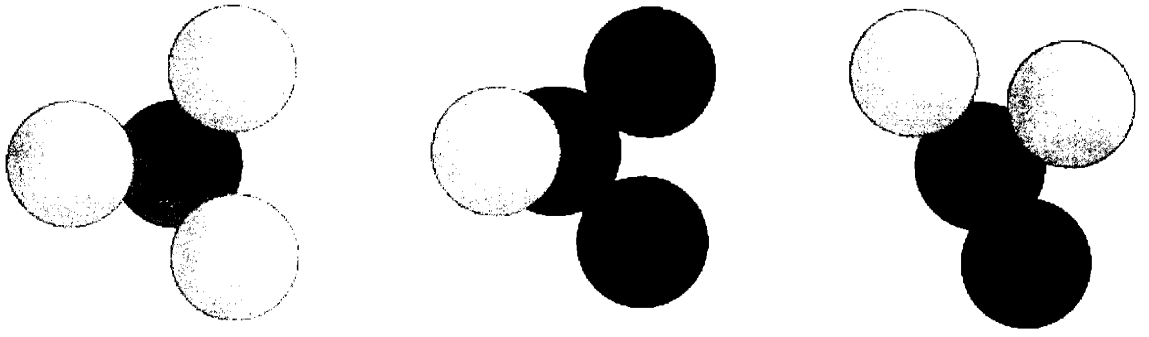

Figure 2.15: Projection onto surface plane of **(a)** C-plane, **(b)** A-plane, and **(c)** R-plane hydroxyl terminated tetrahedra, showing position of sub-surface atoms resulting from the rotation. The relative ionic radii have been exaggerated for clarity.

Figure 2.16, suggesting that the monolayer of hydroxyl groups at the surface is sufficient to change both the composition and structure of the native sapphire crystal due to the relaxation of the aluminum cations. A similar structural change may result on the A- and R-plane surfaces. The net effect is a reduction in coordination of the aluminum cation, leading to different potential determining ion adsorption and accounting for the experimentally observed change in the acidity of the surfaces as a function of crystal orientation. The aluminum cation of the R-plane surface,

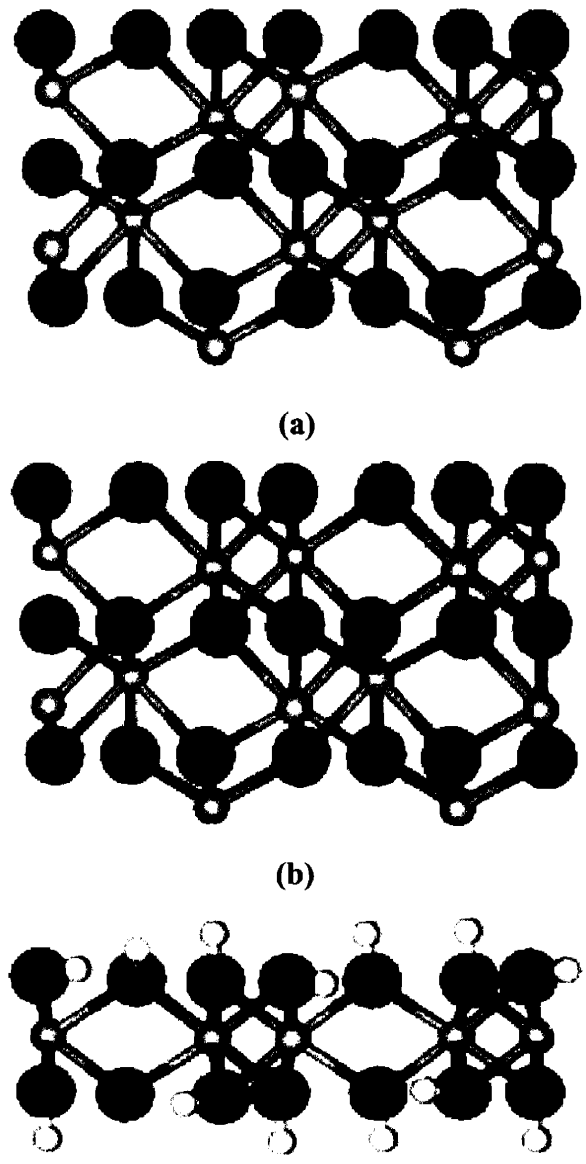

Figure 2.16: Schematic illustration of hydroxyl terminated C-plane crystal showing **(a)** unrelaxed surface structure, **(b)** relaxation of sub-surface aluminum cations and **(c)** comparison to gibbsite structure [69].

exhibiting the most acidic behavior, therefore is the most electron starved and is capable of producing the strongest attraction to a protenated H^+ at the surface. The C-plane surface exhibits a weaker attraction due to the perfect coordination of the Al^{3+} by three surface hydroxyl groups and three sub-surface oxygen anions. A schematic of this behavior is shown in Figure 2.17.

2.7 Brownian Motion and Adhesion

The adhesion of the model system of silica particles to the substrates studied in the previous section define the operating space for future experiments involving directed assembly processes. Adhesion was evaluated by direct observation of the Brownian motion of the particles using digital video techniques. The measurement of particle diffusion on the surface of the sapphire required that the silica be found directly at the surface after settling under the influence of gravity. The rate of settling is found by balancing the gravitational and viscous forces as was first shown by Stokes:

$$(\rho_p - \rho_f)4\pi r^3 \frac{g}{3} = 6\pi\eta r u_t \qquad (2.16)$$

where ρ_p and ρ_f are the densities of the particle and fluid, respectively; r is the particle radius; g is the acceleration due to gravity; η is the viscosity; and u_t is the settling velocity. Rearranging the above expression gives the settling velocity as:

$$u_t = \frac{2}{9}\frac{(\rho_p - \rho_f)r^2 g}{\eta} \qquad (2.17)$$

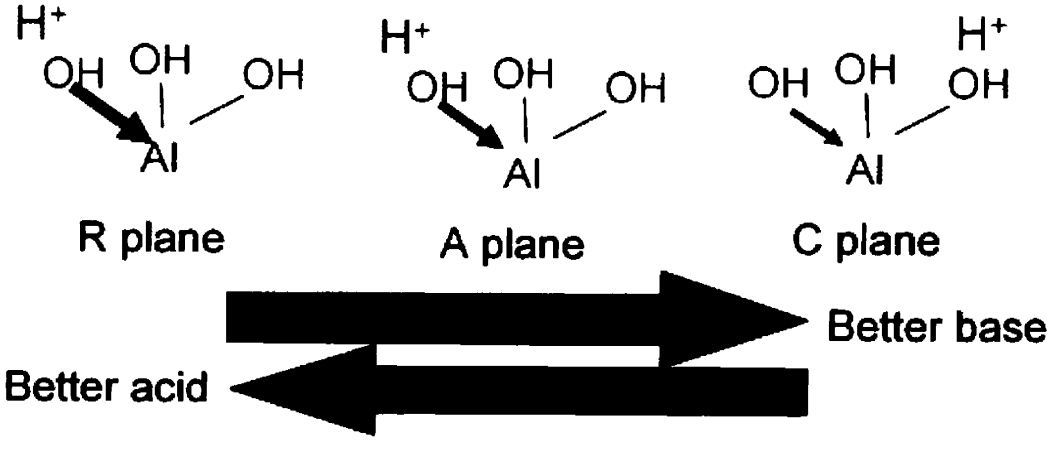

Figure 2.17: Schematic of behavior of the three orientations of sapphire studied, showing relative acidity of R-plane surface due to a reduction in coordination of the sub-surface aluminum cation.

The settling rate of a silica particle having a diameter of 1.58 μm moving through water is calculated to be 1.36 m^2/s. The time required for all particles to settle in a droplet of water deposited on a sapphire substrate is therefore on the order of 25 min. The motion of particles was characterized a function of pH and ionic strength of indifferent ions present in the solution. The free motion of particles was necessary for the study of the electrophoretic motion using applied AC and DC electric fields as described in Chapter 4. Knowledge of the pH and ionic strength range over which this state could be found was therefore particularly important and provided motivation for the characterization of Brownian displacement and adhesion presented here.

2.7.1 Experimental Methods

Monodispersed silica particles having a mean diameter of 1.58 μm were obtained from Duke Scientific Corporation and were initially suspended in a 2 wt% de-ionized water solution at neutral pH. The particle size distribution was extremely narrow, having a variance of 2.5%. No surfactants or other reagents were added and the particles were therefore not purified further prior to use. Dilute solutions of particles were prepared by pippetting a desired volume of the 2 wt% solution into de-ionized water at neutral pH. KNO_3 was then added by weight and the solution was stabilized at the desired pH by the addition of either KOH or HNO_3. The K^+ and NO_3^- ions were known to be non-potential determining for the sapphire surface (need a reference here). Typically 100 mL of particle solution were prepared for most experiments, though other quantities were also used as dictated by each protocol. The concentration of acid or base added was varied depending on the pH range to allow the pH to be stabilized more easily. The appropriate particle concentration was determined empirically by observing the density of particles on the surface after all particles had completely settled. The solutions used for the Brownian motion experiments contained 10^{10} particles L^{-1} such that approximately 1 particle was found per 100 μm^2 and particles were not found to come within more than 50 μm of each other during acquisition of data.

The large size of the 1.58 μm particles relative to the wavelength of light made possible the direct observation of their motion using conventional optical microscopy. A Toshiba Image Master color CCD camera was connected to an inverted metallurgical microscope (Olympus PME) with a 50x objective having a numerical aperture of 0.55. The microscope was positioned on a vibration isolation table such that the instrument could be made level to the ground using

three points of contact. The S-video output from the camera was fed directly into a Panasonic AG-DV2000 digital video recorder. The real time motion of particles was recorded for each experiment and archived to DV format tape. Illumination was provided by a polychromatic source positioned above the substrate such that the particles were imaged by transmitted light. Refraction of light around the particles caused them to appear as halos approximately 5 μm in diameter in the field of view. The position of each particle's center could therefore be clearly identified. Video data recorded to tape was then output to a high capacity IEEE 1394 firewire disk drive using Adobe Premiere 6.0 and a firewire image capture card. All video was captured to disk in NTSC DV format with a resolution of 720 x 480 pixels and a pixel aspect ratio of 0.9. The frame rate was 29.97 fps for all raw video.

Surface diffusion experiments were conducted using solutions having ionic strengths varying from 1 to 10 mM and over a pH range of 3 to 11. A sapphire wafer 5" in diameter and 0.060" thick was obtained from Bicron Crystal Products. The wafer was double side polished, as the direct imaging technique described above required the substrate to be transparent. The wafer was initially cleaned by immersion in a solution of concentrated chromic and sulfuric acids for several hours to remove any organics or other surface contaminants. The wafer was then rinsed thoroughly with de-ionized water and blown dry. A similar de-ionized water rinse was conducted prior to each experiment and the surface evaluated using optical microscopy to verify that particulates had been removed. A small volume of a particle solution stabilized at a desired pH was pipetted onto the sapphire substrate and the particles allowed to completely settle to the surface. A single particle was identified and its motion observed over a period of 20-30 minutes to verify that the particle stayed within the field of view of the microscope. The vibration isolation table was then adjusted accordingly and the procedure repeated until the substrate was deemed satisfactorily level to the ground and lateral migration of the particle due to gravitational forces was minimized. The motion of the particle was then recorded to tape for 60 minutes.

The time dependent motion of particles in the x-y plane was extracted from the digital video data using National Instruments IMAQ Vision Builder 5.0. Premiere was used to capture single still images at an appropriate frame rate. A routine was then performed on each image in Vision Builder to identify the x-y position of the particle of interest at a single point in time. Manual threshholding was used to create a binary image. A circle identification technique was then employed to identify the center of the particle in each frame and the coordinates stored in a

data file. This process is shown in Figure 2.18. An optical calibration was performed to convert the x-y coordinates from pixels to microns for data taken at each magnification. The time-dependent position of each particle was then evaluated using a Matlab routine to determine whether its motion had ceased. Each particle was deemed either moving or stationary using this routine, allowing plots of time-dependent adhesion to be produced. The vast majority of particles were found to remain in the adhered state following initial detection. Particles which were characterized as having returned to the mobile state following initial classification in a stationary state were not included in the statistical analysis.

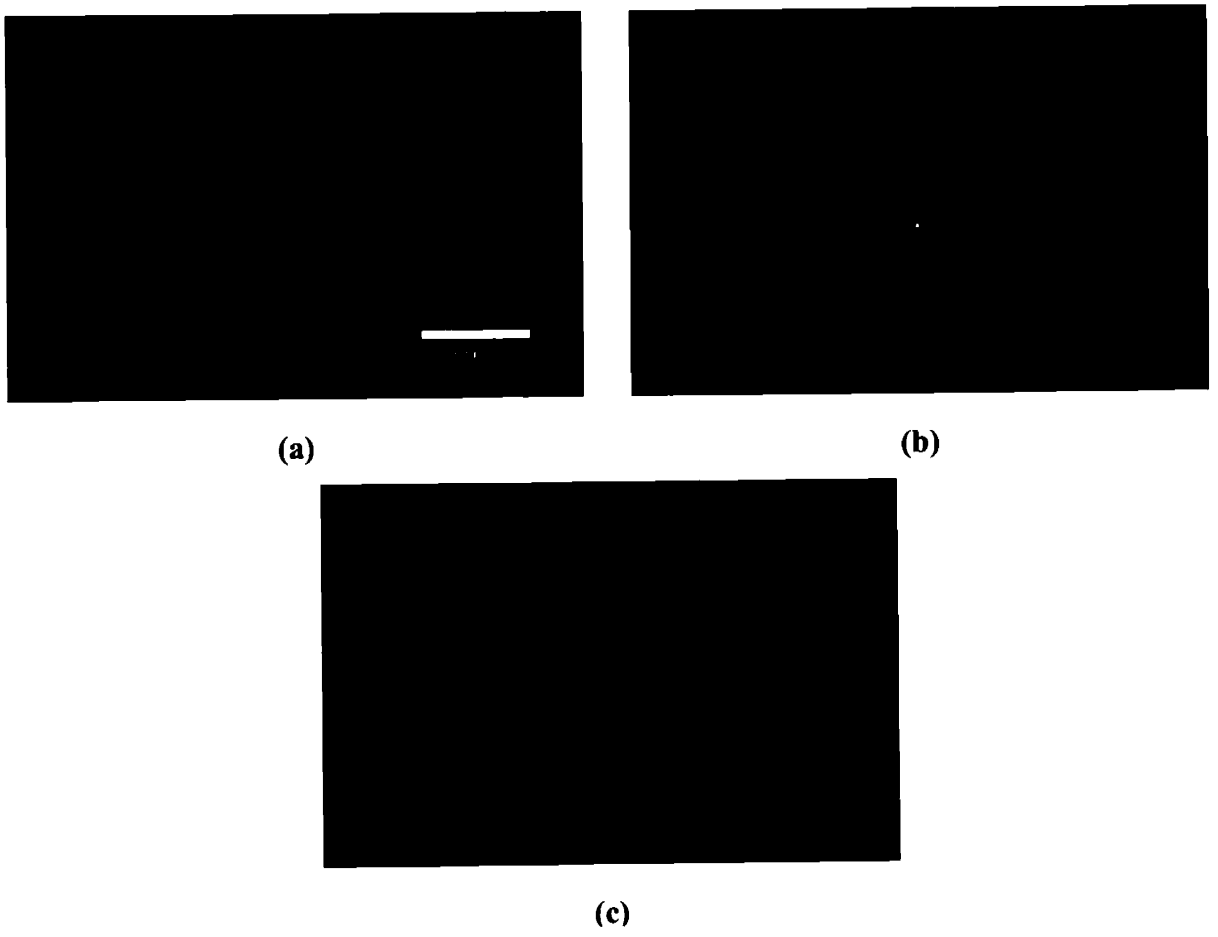

Figure 2.18: Characteristic images of **(a)** original DV image of single particle diffusing on surface, **(b)** thresholded image used to **(c)** identify particle with automation software.

2.7.2 Results

The imaging technique described in the previous section was used to plot the time dependent motion of the silica particles settled on the sapphire surface, as shown in Figure 2.19 for one representative experiment. The data was obtained at a frame rate of 5 fps and the time between individual steps was therefore 0.2 s. Plots of adhesion of particles to the sapphire substrate as a

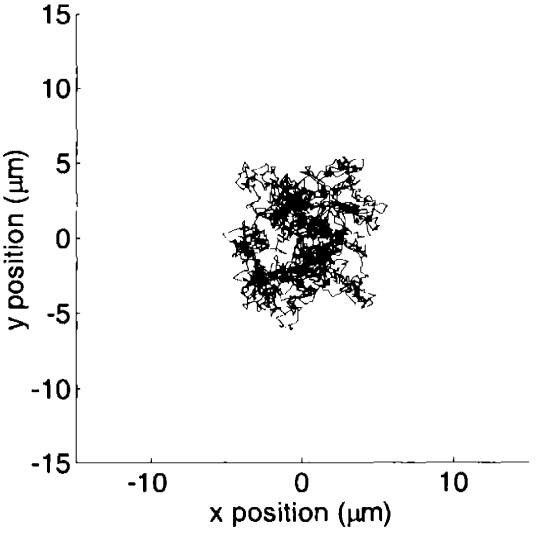

Figure 2.19: Characteristic Brownian motion of a single particles suspended in water at pH 11.

function of time and pH are shown in Figures 2.20, 2.21, and 2.22 for 1, 5, and 10 mM salt con-

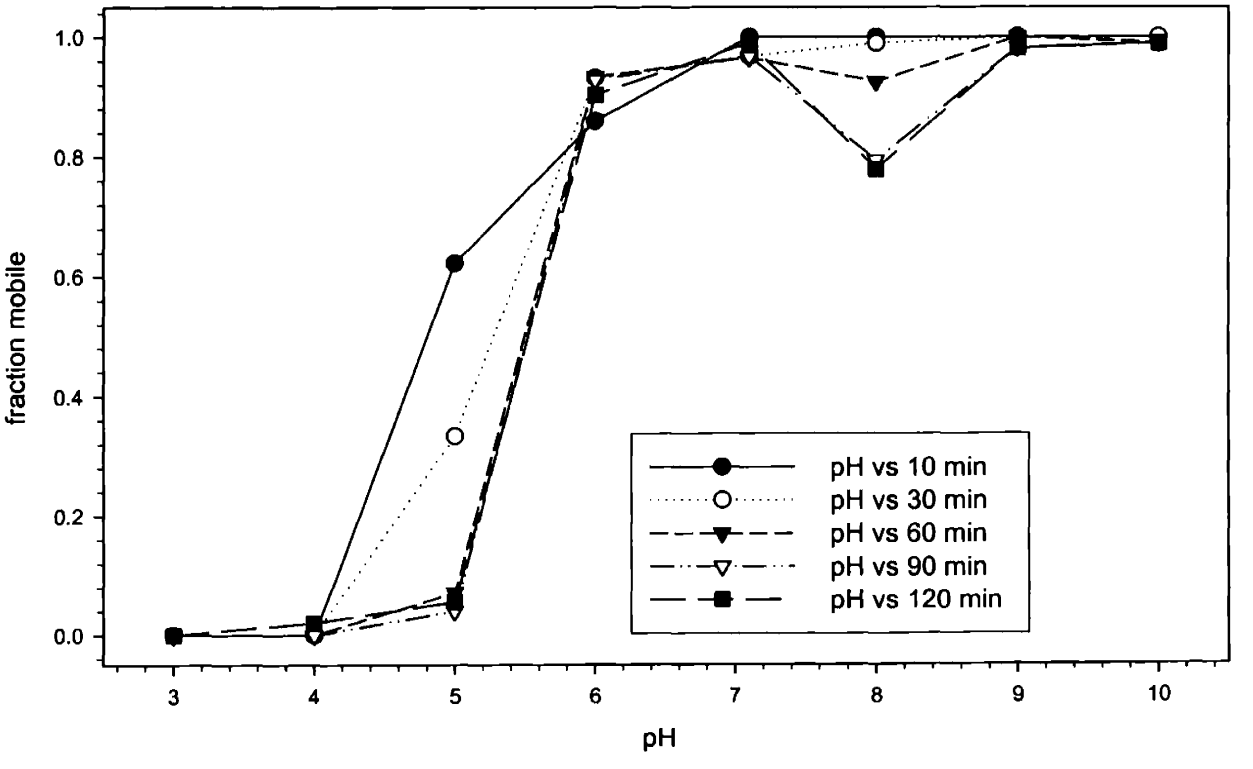

Figure 2.20: Fraction of mobile particles diffusing on an R-plane sapphire substrate as a function of time plotted at various values of pH. The particles are suspended in a 1 mM solution of KNO_3.

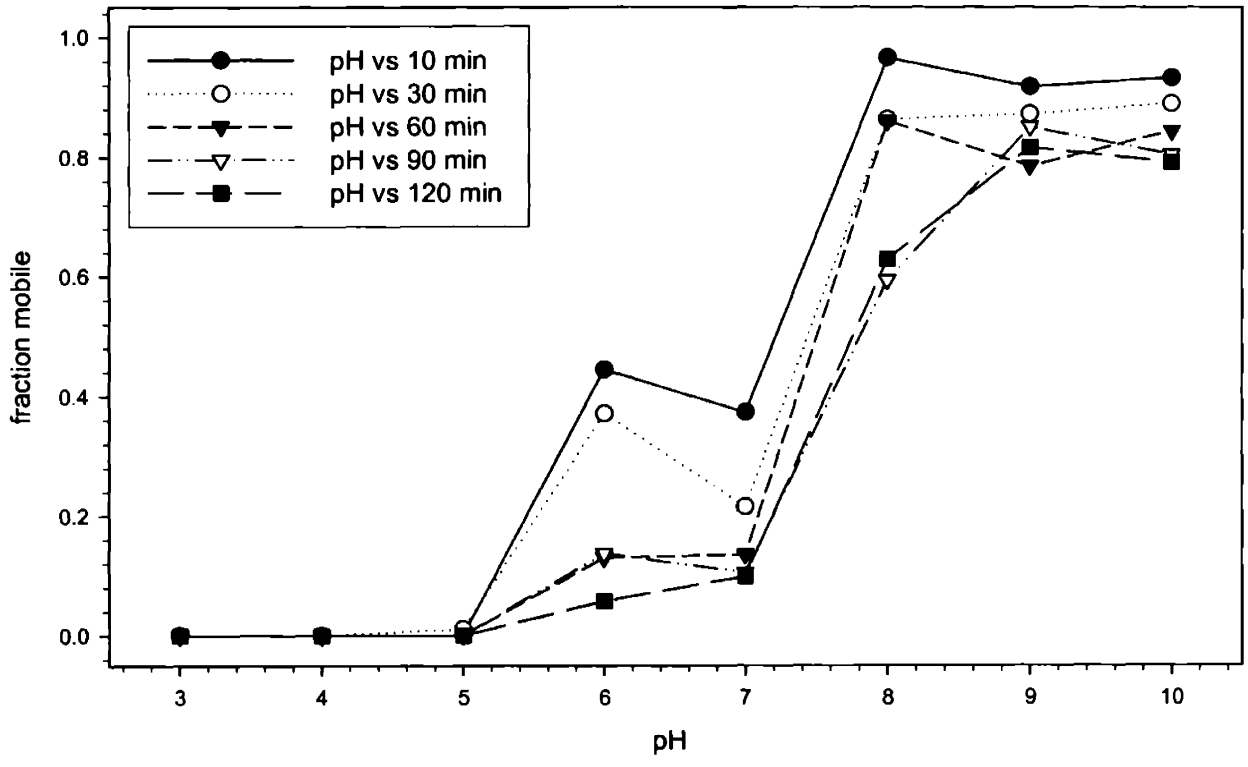

Figure 2.21: Fraction of mobile particles diffusing on an R-plane sapphire substrate as a function of time plotted at various values of pH. The particles are suspended in a 5 mM solution of KNO_3, showing substantial adhesion of particles in the lower pH regime.

centrations, respectively. The plots indicate an increasing probability for adhesion with increasing ionic strength, as would be expected due to the collapse of the Debye layer with added salt. The net effect is to reduce the barrier to adhesion such that a greater percentage of particles are

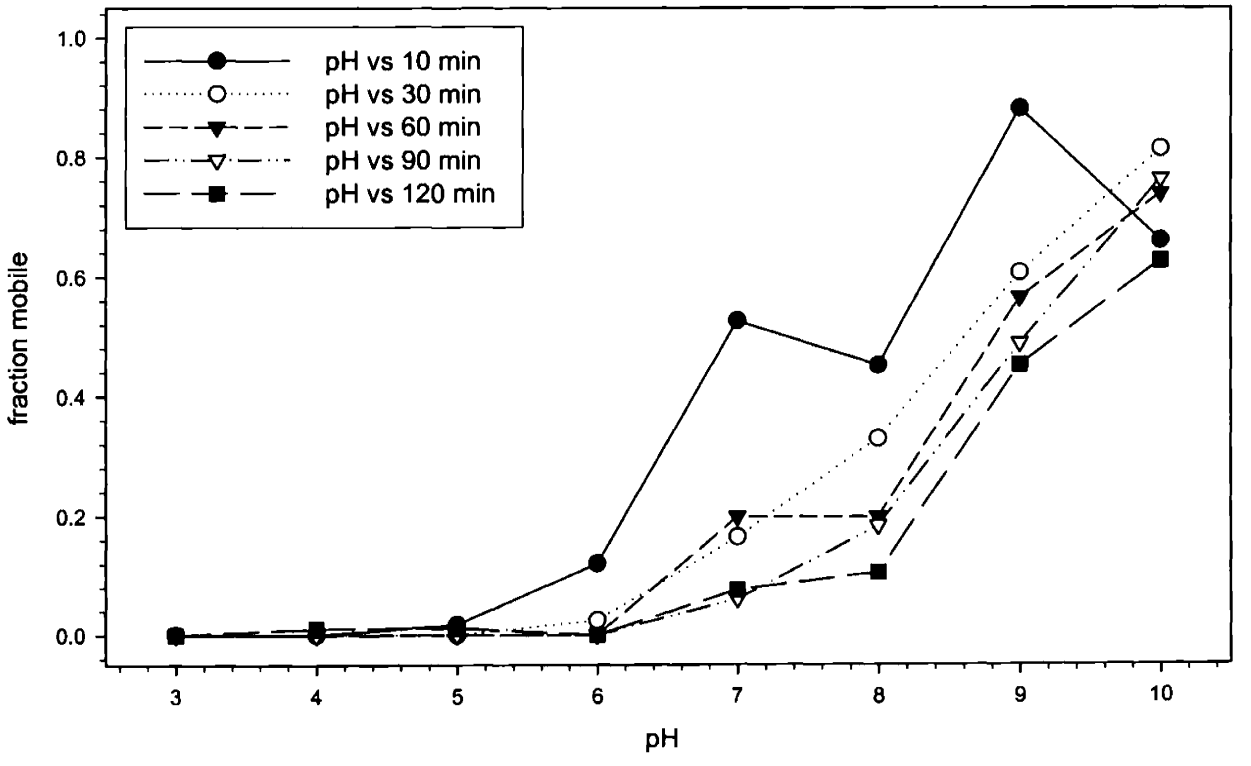

Figure 2.22: Fraction of mobile particles in a 10 mM solution of KNO_3 and water, illustrating substantial adhesion of particles over the full pH range.

adhered at a given pH and time. A clear summary of this effect is provided in Figure 2.23, where the adhesion as a function of pH is plotted for a time of 10 minutes. More subtle, perhaps, is the time-dependent nature of the adhesion. Figure 2.20 shows quite clearly that even at the lowest ionic strength considered the time-dependent behavior at a pH of 5 is quite dramatic, with approximately two-thirds of the particles adhering to the substrate after 10 minutes and a substantial reduction in the number of mobile particles occurring over the next 20 minutes. Nearly all of the particles become adhered before a time of 60 minutes. The effect of time is even more pronounced at the higher ionic strengths, as demonstrated in Figure 2.22. Here the number of adhered particles increases dramatically with increasing time at every pH above 5. This data served to define the pH and ionic strength operating regime for subsequent electrophoretic deposition experiments, to be presented in Chapter 4.

2.8 Conclusions

This chapter has laid the groundwork for exploring the role of complex surface interactions during electrophoretic deposition. Electrokinetic measurements were conducted on the model system of silica particles to characterize the zeta potential as a function of pH and ionic

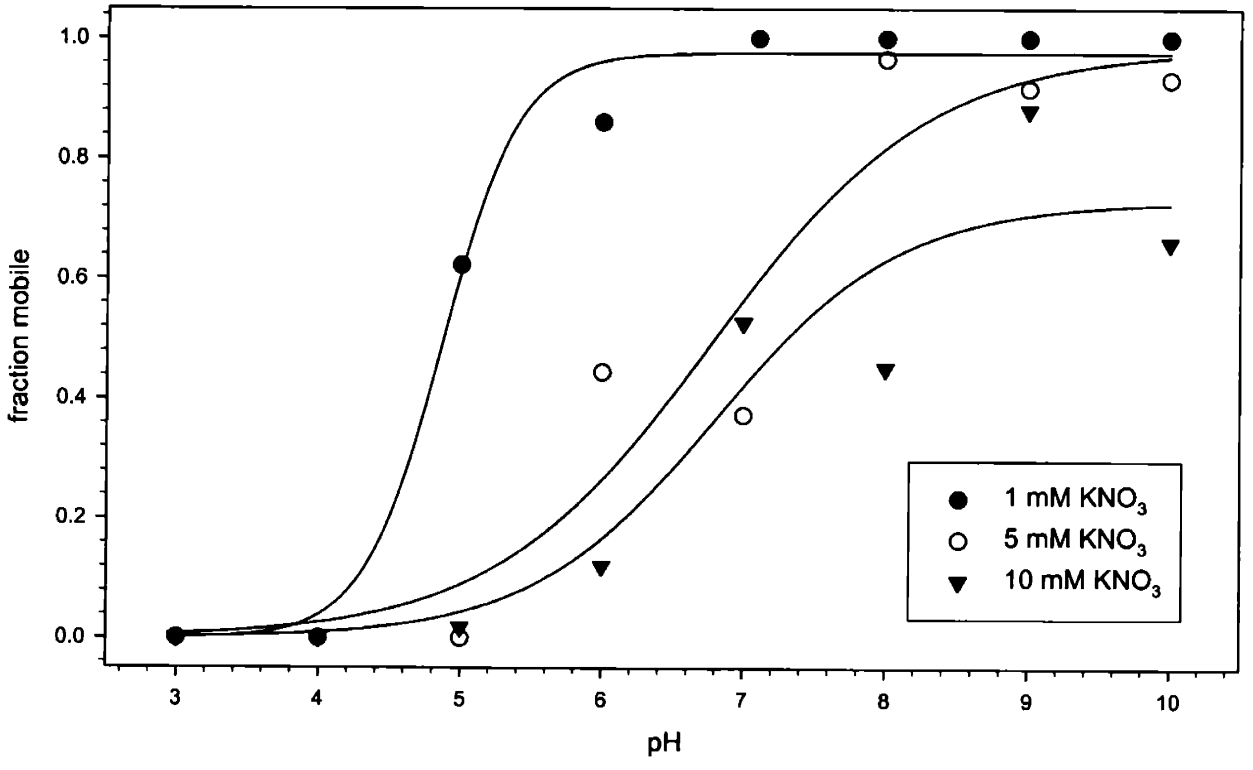

Figure 2.23: Adhesion of silica particles to R-plane sapphire surface after diffusing on surface for 10 minutes. The trendlines are provided simply to guide the eye.

strength. The sapphire substrate was also studied using a streaming potential technique, with great emphasis placed on the dependence of zeta potential on orientation for these single crystalline substrates. Carefully controlled streaming potential measurements were conducted at several different ionic strengths. The zeta potential was evaluated for each crystal plane over the full pH range, allowing three distinct well-defined i.e.p.s to be observed. The dramatic reduction in i.e.p. as compared with α-Al_2O_3 particles suggests a substantially different surface chemistry for the two systems. The systematic shift in i.e.p. as a function of crystal orientation suggests a change in the acidity of the three surfaces. This conclusion was verified by a modified Auger parameter analysis of iridium metal deposited on the surface, revealing a shift in the MAP corresponding to a change in the charge transfer behavior for the R-, A-, and C-plane sapphire substrates.

The role of adhesion in electrophoretic processes will be explored further in Chapter 4. The preceding pages also provided a basis for this investigation by presenting a thorough study of the adhesion of silica particles to the sapphire substrate in absence of externally applied forces. A digital imaging technique was developed to measure the Brownian motion of micron scale silica particles and in turn used to measure the time-dependent adhesion of particles as a function of pH and ionic strength.

Chapter 3: Fabrication and Characterization of an Electrophoretic Deposition Device

3.1 Introduction

This chapter outlines the development and characterization of the system of micropatterned electrodes used to investigate surface forces during electrophoretic assembly. The fabrication of the device is first detailed, followed by a presentation of the packaging used to make electrical contacts. Results of finite element analysis (FEA) are then presented, illustrating the field distribution between the parallel electrodes used in this work. Attention is given to the uniformity of the field as a function of electrode height and interelectrode distance. Finally, the use of electrochemical techniques to characterize the reversibility of the electrodes is highlighted.

3.2 Device Fabrication

3.2.1 Patterning of Sapphire Substrates with Metal Microelectrodes

The electrophoretic positioning device comprised of micropatterned platinum electrodes was fabricated in the Microsystems Technology Laboratory (MTL) at MIT in a class 100 cleanroom environment. A standard ultraviolet photolithography recipe was optimized to produce features having the desired dimensional stability and uniformity. A layer of photoresist was patterned to provide a physical mask for subsequent electron beam deposition of the metal electrodes onto the substrate. This process is commonly referred to as lift-off, so-named because the photoresist mask coated with metal is subsequently removed by soaking in a solvent to leave the desired metallized features patterned on the surface.

Sapphire wafers similar to those used in the streaming potential measurements presented in Section 2.5 were obtained from Saint Gobain Crystals and Detectors (Washugal, WA). One side of the 2" diameter wafers was polished by the manufacturer with a finish suitable for epitaxial growth while the other side was fine ground, making the wafers optically transparent. The as-received wafers were cleaned by rinsing in acetone, methanol, and isopropyl alcohol followed by blowing dry with a steady stream of nitrogen to remove any residual contaminants that may have been deposited during the final polishing step. Hexamethyldisilazane (HMDS) was then deposited in a YES 310T Vapor Prime Oven to promote adhesion between the substrate and photoresist. AZ5214E image reversal photoresist was spun onto the substrate using a Solitec 5110 spin coater, followed by a prebake step during which the wafers were heated in a convection oven for 30 min-

utes at 90 °C. Patterning of the photoresist was then performed by exposing the wafers to ultraviolet light for 40 seconds through a dark field mask in a Karl Suss MA-4 Mask Aligner. The photoaligner was operated in hard contact mode, with the wafer secured to a vacuum chuck to ensure that the features were well defined. The precise alignment of the mask during this step was not necessary since the process consisted of only one mask layer. Another bake in a convection oven was then performed, followed by a flood (unmasked) exposure in the photoaligner for 30 seconds. The photoresist was then developed in an ammonium hydroxide based developer (AZ422MIF) for 90 seconds, leaving a mask of hardened photoresist on the surface with exposed regions corresponding to the areas to be metallized to create the desired features for the EPD device. A Teresco Electron Beam Evaporative Deposition System was then employed to deposit a 100 angstrom thick film of titanium to act as an adhesion layer between the substrate and subsequent metallization. This was followed by deposition of a 200 nm thick noble metal film, resulting in a uniform deposit over both the exposed substrate and the photoresist mask. One final step was performed to "lift-off" the remaining photoresist by immersing the wafer in acetone and sonnicating for approximately 2 minutes, leaving behind the desired metallized features patterned on the substrate. Results of experiments using both.platinum and gold electrodes are presented in Chapter 4.

3.2.2 Blackening of Electrodes

The role of the resistance of the electrical double layer at the electrodes becomes increasingly significant as the interelectrode distance is decreased [81]. It is necessary at small spacings

to consider the reversibility of the electrodes. The two limiting cases are depicted below in Figure 3.1. The completely non-polarizable (reversible) electrode is characterized by an infinitesimally small resistance at the interface with $R_i \ll R_f$. The potential drop between the electrodes therefore occurs entirely in the bulk fluid, resulting in a maximum electric field. The polarizable or (blocking) electrode, on the other hand, exhibits a substantial interface resistance such that $R_i \rightarrow \infty$ and $R_f \ll R_i$. This gives a significant potential drop near both electrodes and the voltage gradient in the bulk fluid is much smaller than that simply approximated by dividing the potential applied between the electrodes by the distance between them. The situation is, in fact, rather unstable such that small fluctuations in the resistance of the interface or fluid will cause the electric field midway between the electrodes to vary by a large percentage [82]. Reversible electrodes are prepared by increasing the surface roughness (known as blackening), thus increasing the exchange current density at the electrode surface. The platinum electrodes were blackened by immersing the device in a chloroplatanic acid/2% lead acetate solution and applying a low frequency alternating current. This process resulted in the electrolytic deposition of a uniform 5 μm thick platinum coating that appeared black in color under an optical microscope due to the substantial increase in surface roughness. The gold electrodes were not blackened and were always used in an as-deposited condition.

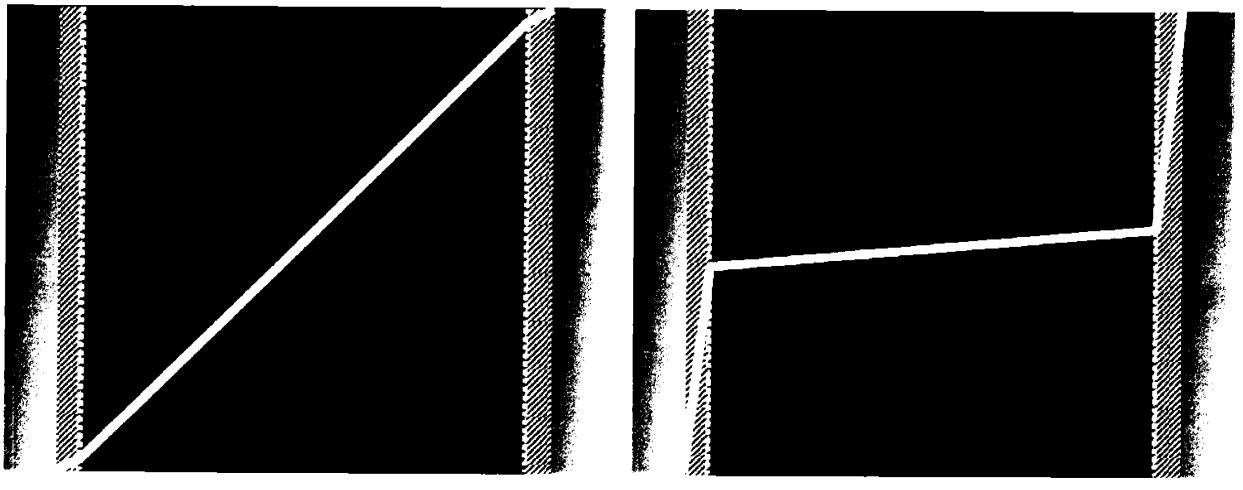

Figure 3.1: Schematic of **(a)** reversible and **(b)** blocking electrodes, showing potential drop as a function of position from the electrode-fluid interface.

3.2.3 Removal of Devices from Wafer

Several individual devices measuring 10 mm x 10 mm were fabricated on a single wafer, and a cleanroom diesaw was used to separate adjacent devices for mounting in a package (see Section 3.3). A six-pass dicing program coupled with a carbide blade allowed the sapphire wafers having an extremely high hardness to be cut out without cracking or substantial chipping. The blade was moved across the wafers having a thickness of 0.060" at a rate of 1 mm/second. The wafers were coated with photoresist to protect them during dicing. A post process hydrogen plasma ash was performed to remove any remaining photoresist and strip the surface of other contaminants, followed by a final rinse of the individual devices in acetone. The devices were then mounted into packaging as described in the next section.

3.3 Packaging

3.3.1 Early-stage Devices

A 100-pin polymer pin grid array (PPGA) package was selected from Chelsea Technology Corporation and used in early-stage prototypes to provide electrical connections to the EPD device. The cavity of the package was through-machined to allow imaging of the particles from below through the transparent substrate during operation of the device. The mounting of the device in the package cavity was first accomplished using a two-part quick curing epoxy (Master Bond). A thin dot was placed at each corner and the device was fitted into the machined area. A gold wire bonder was then used to make electrical connections between each individually addressable electrode and the package. A schematic of the pin configuration showing the wirebond con-

nections is shown in Figure 3.2. Here the entire device is shown, though the work contained in this thesis was conducted using only the region of the device known as parallel electrodes. Other experiments conducted with other features will not be presented. A magnified image of the paral-

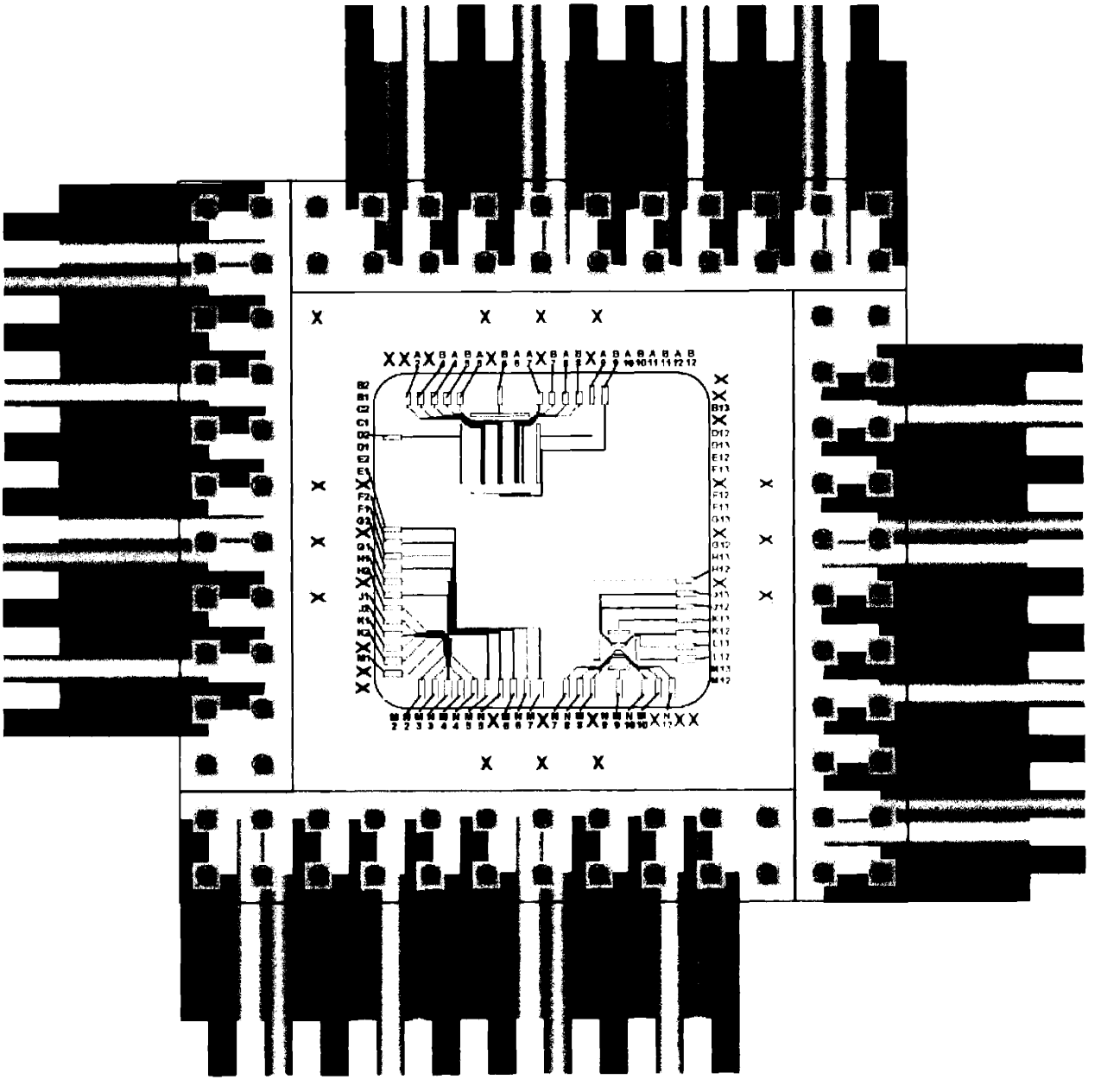

Figure 3.2: Schematic of pin configuration for EPD device, illustrating wirebonds to specific pins.

lel electrode device area is shown in Figure 3.3.

It was determined after a few initial experiments that the fragile wirebonds were subject to failure through delamination or other means due to their exposure to the environment. The epoxy was once again employed to solve this problem, providing a moisture free seal that protected the electrical connections from damage. Epoxy was applied generously to the devices and care was taken to avoid any contamination of the electrodes during this process. The epoxy provided the additional benefit of sealing the gap between the device and package such that fluid was prevented from leaking out during EPD experiments.

3.3.2 Epoxy Free Package Design

The epoxy used to secure devices presented in the previous section was later identified as a possible source of contamination. The epoxy was replaced with a polysulfone clamp in a new package design that served the same function of sealing the gap between the device and package. The clamp was secured to the package with small screws, and a rubber gasket placed between the device and the edge of the package cavity allowed a mechanical seal to be formed. The clamp also provided an open reservoir into which a precise volume of particle suspension could be pipet-

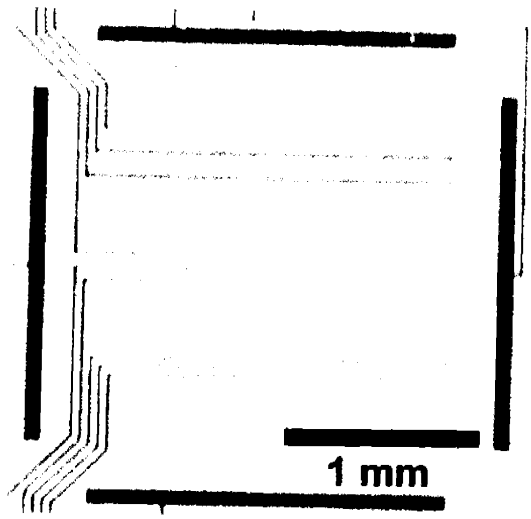

Figure 3.3: Photograph of parallel electrode area of finished device.

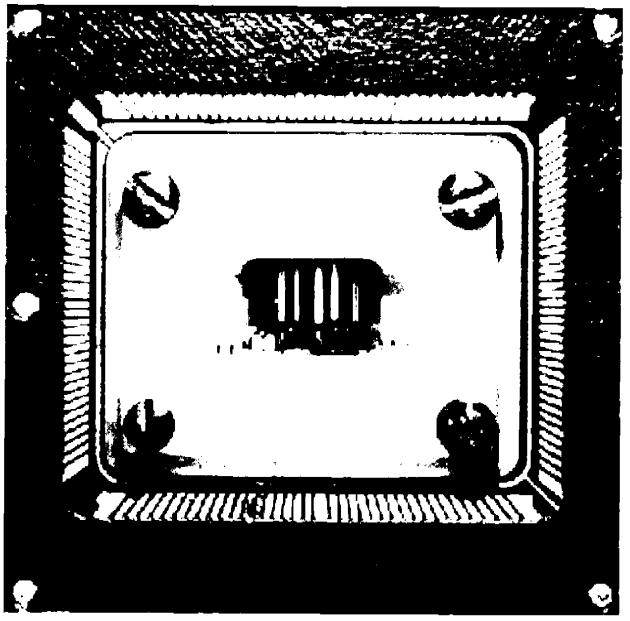

Figure 3.4: Photograph of device secured to package and held in place by polysulfone clamp.

ted, as shown in Figure 3.4. Wirebond connections were made over the clamp and were replaced each time the device was removed for cleaning. The wirebonds could also be easily replaced as necessary following damage or delamination from the bondpads.

3.4 Finite Element Analysis

3.4.1 Experimental Methods

Complete knowledge of the electric field distribution between the electrodes is paramount to understanding the behavior and velocity of particles both very near the electrodes and in the bulk fluid region midway between. A commercial finite element software package was used to model the field distribution between the electrodes during application of a potential. The field strength for both interelectrode spacings of 100 μm and 2500 μm was measured over a range of applied voltage. A single electrode height was modeled for the larger interelectrode distance. The electric field distribution was calculated at three different electrode heights for the 100 μm spacing. Four independent components were defined for the system comprised of the working electrode, counter electrode, fluid, and sapphire substrate, with the corresponding dielectric properties as summarized in Table 3.1. The software, provided by Algor Engineering, Inc., allowed

Table 3.1: Modeling parameters for finite element analysis

Material	Relative Dielectric Constant
Au	1000
Al_2O_3	10.0
H_2O	80.0

for the mesh to be defined either manually or automatically using a meshing routine. The later method is superior from a calculation efficiency standpoint as it also allows the mesh density to be varied locally over the model, though presents difficulties for small geometries where matching of the mesh across material boundaries is required. An automatic mesh approach was selected for the larger interelectrode spacing requiring a larger model size while manual meshing could be applied easily to the smaller 100 μm distance. The total size of the model in both cases was adjusted such that the fluid surrounding the electrodes was approximately twice the interelectrode distance in the dimension corresponding to the plane of the substrate.

3.4.2 Results

A plot of the electric field distribution near a completely non-polarizable blackened anode is shown below in Figure 3.5. Two constant applied potentials are shown. The field in both cases is remarkably uniform in the bulk region up to a distance of approximately 20 μm from the electrode, at which point a sharp field concentration caused by the edge of the electrode occurs. It should be noted that this analysis assumes that all of the applied potential is dropped over the bulk fluid in-between the electrodes. The model does not consider the effects of interface resistance,

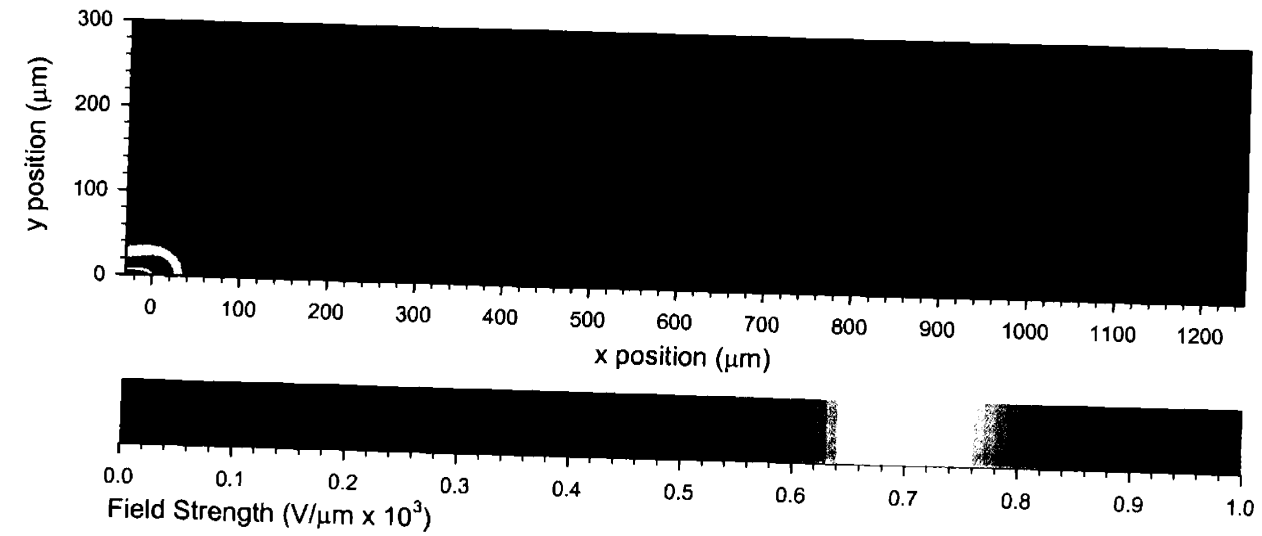

(a)

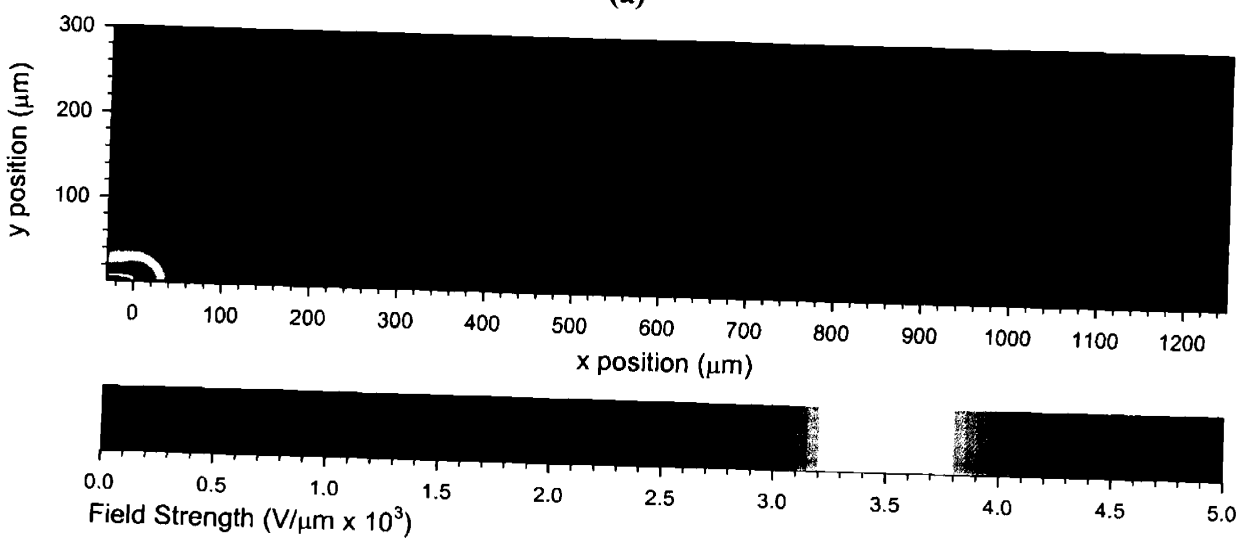

(b)

Figure 3.5: Magnitude of electric field plotted from working electrode (at left) up to a point midway between the electrodes for an applied potential of **(a)** 1000 mV and **(b)** 5000 mV. The scale

and assumes complete reversibility of the electrodes. Similar results were obtained for the smaller interelectrode spacing, as shown in Figure 3.5. Here the field is also measured to be uniform in the bulk region between the electrodes, with the same sharp increase in the gradient very near the electrodes. The model also shows that the magnitude of the field is relatively insensitive to electrode height, with the same distribution illustrated in Figure 3.6 (a) for a height of 0.2 μm as at 10 μm shown in Figure 3.6 (c). Figure 3.6 (d) shows the effect of electrodes having rounded edges. The field is essentially the same in this case, with no substantial reduction in the sharp discontinuity in the field achieved by softening the corner. This model more closely approximates the geometry expected in an actual blackened electrode, where the blackening is deposited isotropically. These results can be extended to the larger interelectrode spacing where the uniformity of the field is likely less sensitive to changes in the height of the electrodes. Small fluctuations in the blackening process would therefore have little effect on the field distribution and hence would not affect the motion and deposition of particles during EPD.

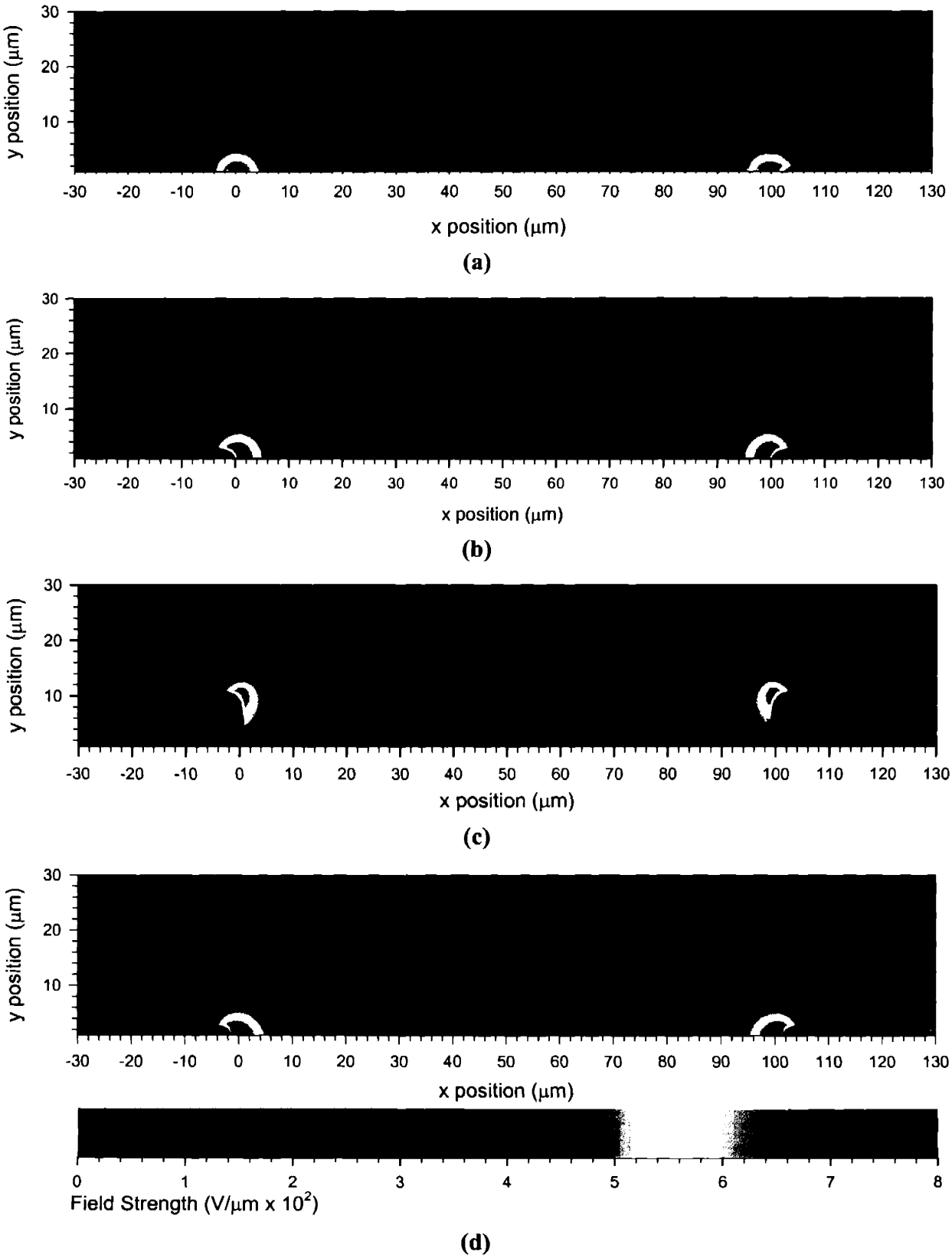

Figure 3.6: Calculated electric field distribution with an interelectrode distance of 100 μm for electrode heights of **(a)** 0.2 μm, **(b)** 2 μm, **(c)** 10 μm, and **(d)** 2 μm with rounded edges.

3.5 Electrochemical Characterization

A study of the electrochemical processes occurring at the electrodes as a function of applied potential was also undertaken. The goal of this work was to identify a specific regime over which the production of a particular ionic species in the gold electrode-nitrate electrolyte system. Cyclic voltammetry with a platinum reference electrode was employed to investigate the effect of low frequency applied AC fields on the current response of the electrodes. These results were compared with the experimentally observed production of dissolved gaseous species at the extremes of potential, manifested by the evolution of gas bubbles as shown in Figure 3.7. A char-

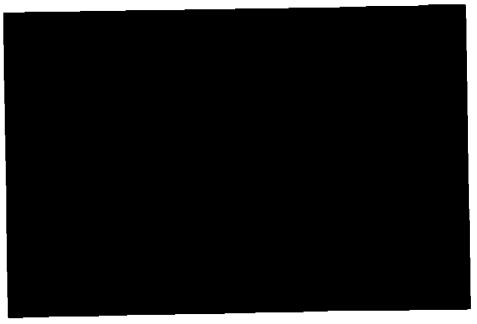

Figure 3.7: Formation of bubbles of dissolved gaseous species during application of potential corresponding to oxidation or reduction reactions.

acteristic cyclic voltamagram is shown in Figure 3.8. A platinum reference electrode was used to measure the potential relative to a standard hydrogen electrode (SHE). The plot shows a relatively reversible system in the positive potential region, with two significant reactions occurring at potentials of 0 and -0.5 V. The sharp increase in current at extreme potentials of 1.5 and -1.5 V indicate the rapid production of hydrogen ion due to hydrolysis of the aqueous medium. These results further validate the need for blackened electrodes to provide a truly reversible system during electrophoretic deposition.

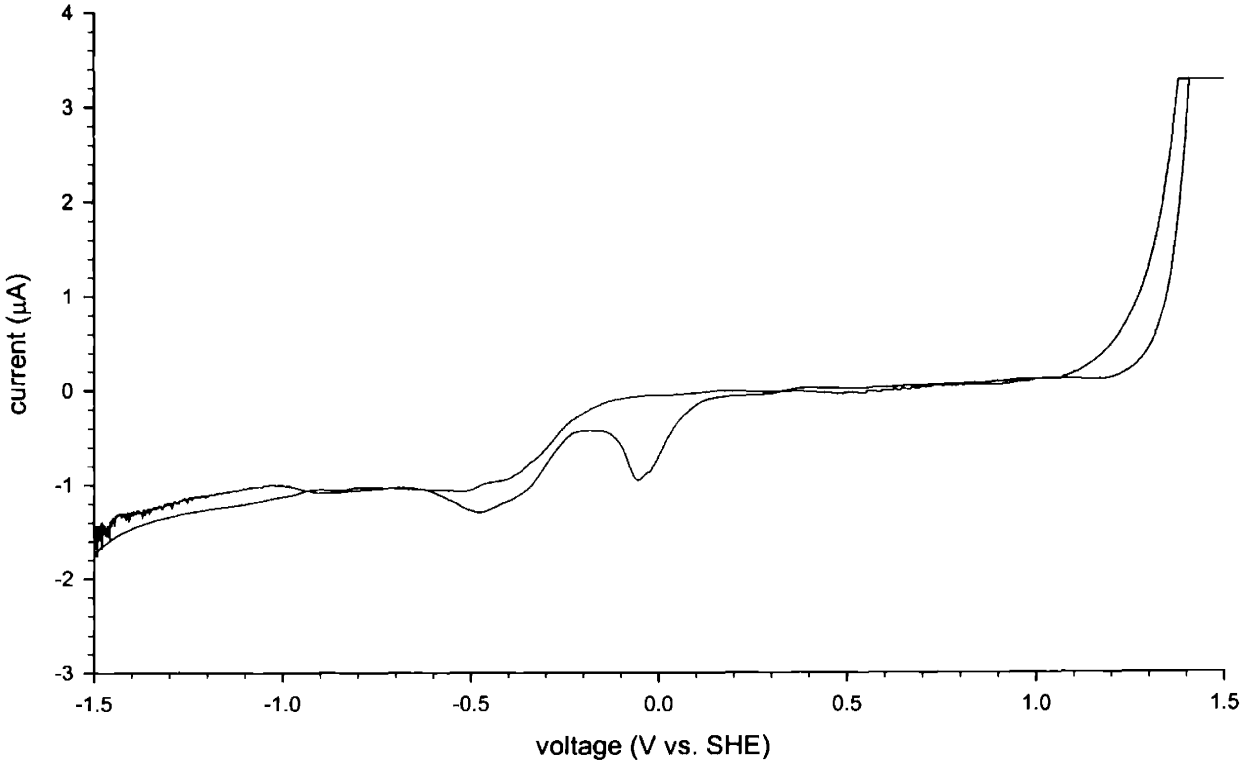

Figure 3.8: Cyclic voltamagram for unblackened platinum electrodes in presence of a 1 mM solution of KNO_3.

Chapter 4: Manipulation of Particles Using Applied Electric Fields

4.1 Introduction

Electric fields applied between microelectrodes deposited on a surface have been used to create a range of structures including optical waveguides, magnetic data storage devices, and bio-sensors [83][84][85]. Two classes of electric field assisted assembly have emerged, namely dielectrophoresis (DEP) originating from induced dipoles in the presence of spatially non-uniform AC or DC fields and electrophoretic deposition (EPD), in which the electrical double layer formed around particles suspended in a fluid medium causes motion in the presence of a spatially uniform field. The use of DEP for the movement and assembly of particles and biological systems has been well characterized in the literature [86][87]. Applications have ranged from the sorting of various cell types to the capture and fractionation of DNA for immunological assays [88][89]. More recently, applied AC fields between microelectrodes were utilized to form microwires from sub-micron metal particles [90]. EPD has been used extensively in commercial coating and electro-assembly processes [91]. A related process known as electro-osmosis, in which the ions in solution cause bulk fluid flow can be responsible for particle motion by viscous drag. Others have reported this phenomenon between microelectrode structures in the presence of both spatially uniform and non-uniform fields but many questions as to the nature and regime of these flows remain unanswered [92]. The high electrical fields necessary to induce substantial particle motion using DEP have also been shown to produce deleterious thermal gradients and electrothermal flows which may contribute to particle motion. These currents are likely to be present during EPD as well [93].

The velocity, v of a charged ceramic particle in the presence of an applied uniform parallel electric field, E is well understood and is described by the familiar Smoluchowski equation:

$$v = \varepsilon_f \zeta_p E / \eta \qquad (4.1)$$

where ε_f and η are the dielectric constant and viscosity of the electrolyte, and ζ_p is the zeta potential of the particle [94]. The driving force resulting from the field is balanced by viscous drag on the particle due to the surrounding fluid medium. This expression is valid for large particles such that the particle radius is much greater than the thickness of the electrical double layer. Particles moving in the vicinity of a planar surface require that the above expression be modified

to account for interaction between the particle and the substrate. The double layer present at the charged substrate surface gives rise to an electro-osmotic flow, the effect of which may be superposed with the velocity field of the particle as follows [95]:

$$v = \left[1 - \frac{1}{16}\lambda^3 + \frac{1}{8}\lambda^5 - \frac{31}{256}\lambda^6 + O(\lambda^8)\right]\frac{\varepsilon_f E}{\eta}(\zeta_p - \zeta_s) \qquad \textbf{(4.2)}$$

where λ is the ratio of the particle radius to the distance between the surface and the particle center, $O(\lambda^8)$ is an error term, and ζ_s is the zeta potential of the substrate. The complete solution represents an expansion of a series of fields reflected from the wall and imposed on the particle in an open system, that is, one in which no pressure gradients exist to oppose the electro-osmotic flow at the wall. The separation between the particle and wall may be assumed to be small relative to the particle radius for large particles such that approaches unity.

The electrophoretic assembly device introduced in Chapter 3 was used to evaluate the effect of field strength on in-plane particle velocity. Observations of bulk particle motion far from the electrodes (electrophoresis) and agglomeration of the particles at the working electrode (deposition) are presented. The zeta potentials of the particles and substrate were measured experimentally as a function of pH and ionic strength and used to calculate the expected particle velocity midway between the electrodes. Results of electrophoretic deposition experiments are presented which illustrate the use of spatially uniform fields for manipulating the in-plane position of micron scale particles. Particles can be positioned anywhere on the surface using this technique, and are also observed to form packed two-dimensional structures directly at the electrode. Substantial adhesion of particles to the substrate in the vicinity of the working electrode coupled with a reduction in velocity near the electrodes was observed. Both phenomena are attributed to the production of potential determining ions at the electrode, causing the differing surface chemistries of the silica particles and sapphire substrate to play a more substantial role than expected in the EPD process. Further validation of this significance was provided by directly measuring the nanoscale forces between the particle and substrate using an atomic force microscope (AFM). Complete force distance curves were measured *in-situ* and the resulting reduction in force as a function of both distance from the electrode and time is presented for a variety of conditions.

4.2 Experimental Methods

4.2.1 Surface Preparation

A surface treatment was employed for all devices and wafers to ensure that the sapphire surfaces were clean and free of organic and other contaminants prior to EPD experiments or measurement of electrokinetic properties. The cleaning procedure consisted of immersing the wafers in a 4:1 bath of sulfuric acid and hydrogen peroxide (commonly known in the microelectronics processing industry as a 'piranha' etch), followed by thorough rinsing in deionized water and blowing dry with nitrogen. X-ray photoelectron spectroscopy was performed on the treated wafers and devices to verify that the surfaces had been adequately cleaned both before and after the electrodes were patterned. It was also confirmed that no silica contamination had occurred at any point during the collection of data. Atomic force microscopy was also used to image the surfaces and confirm that the roughness was not modified by the cleaning procedure.

4.2.2 Preparation of Particle Suspension

The suspension was prepared from monodispersed 1.58 μm diameter SiO_2 particles as received from the manufacturer (Duke Scientific Corporation). The particles were initially suspended in deionized water at neutral pH with no surfactants or salts and were not rinsed prior to use. The concentrated suspension was diluted to contain approximately 10^{10} particles L^{-1}, to which between 1 and 10 mmol of KNO_3 was added. The pH was then adjusted in one direction only to 10.0 using 0.1 M KOH. No acid was used to further bracket the pH in order to keep the conductivity as low as possible for a given salt concentration.

Each experiment was conducted by pippetting a fixed quantity of particle suspension onto the open device. The particles were then allowed to settle under the influence of gravity for approximately 10 min prior to application of the electric field to ensure that all particles were found in the plane of the electrodes at the start of each experiment. A digital video system consisting of a Toshiba color CCD camera and Panasonic digital video tape recorder was connected to the microscope to allow real-time imaging of particle motion. Video data was archived to a digital tape, and individual frames were captured and analyzed using Adobe Premiere 6.0 with an IEEE 1394 interface.

4.2.3 Application of Electric Field

A Gamry PC4-300 potentiostat was used to apply an absolute potential between the working and counter electrodes. Current measurement was facilitated by tying the reference lead of the potentiostat to the counter electrode. A maximum potential was defined as the point at which gas bubbles were nucleated at the electrodes. The field was kept below the limit of bubble formation such that the particle motion was not disturbed by the effects of chaotic fluid flow during evolution of gas.

4.2.4 Atomic Force Microscopy

A Veeco Dimension 3100 AFM with a Nanoscope IV controller was used to acquire force-distance curves near the electrodes. Standard contact microscopy probes mounted with a single silica bead having a diameter of 6 μm were purchased from BioForce Nanosciences, Inc. and used to measure the interaction with the sapphire surface. Effort was made for these force measurements to reproduce exactly the same conditions experienced during electrophoretic deposition experiments. The same potentiostat, cabling, salt solutions, and pH stabilization method were therefore used. The devices were mounted on a glass slide (in absence of the polysulfone package detailed in Section 3.3.2) to provide open access required by the small geometry of the AFM cantilever mount, with electrical connections to the potentiostat provided by wirebonding as before. Each experiment consisting of a time series of force-distance curves measured at a single distance from the electrode was conducted by first pippetting approximately 100 μL of 1 mM solution having an initial pH of 10. The AFM was then moved into contact with the surface far from the working electrode and the position of the electrode identified by translating the AFM piezo in feedback mode until a dramatic change in height was observed.

Force-distance curves were then acquired for approximately 20 seconds at a frequency of 1 Hz in absence of any applied field to provide a control dataset, followed by measurement of the effect of an applied potential for 60 seconds. This was followed in some experiments by an extended observation period during which a return to the initial pH near the electrodes was recorded as the fluid equilibrated with the bulk while the field was again turned off. Datasets at additional distances and/or potentials were collected in succession using the same setup and surface preparation without replacing the fluid droplet. The system was allowed to return to equilibrium as verified by measuring force-distance curves after a sufficient period of time had passed, facilitating the collection of data that could be consistently compared within a given set of condi-

tions. An open bottle of solution at the initial pH was also continuously monitored to ensure that no substantial reduction in pH occurred during the return to the equilibrium pH. Constant potential measurements corresponding to the EPD experiments were conducted at 100, 500, and 1000 mV and a single set of constant current force-distance curves were recorded at 500 nA.

4.3 Results

4.3.1 Positioning of Particles

The positioning electrodes consisted of two sets of features oriented orthogonally, between which electric fields were applied to control particle motion in the x- and y-direction. These initial experiments were conducted using nonblackened, gold electrodes. The application of a DC field to these electrodes resulted in particle motion following the direction of the field lines. The particles were moved across the substrate at a uniform velocity by a potential drop across opposing sets of electrodes. The x- and y-positions of the particles could therefore be controlled in this fashion, allowing particles to be 'driven' into position in the vicinity of the parallel

electrodes. Figure 4.1(a) illustrates the field applied between the x and y electrodes, while the motion of a single particle as imaged at the center of the structure (midway between both the x and y electrodes) is shown in Figure 4.1(b).

(a)

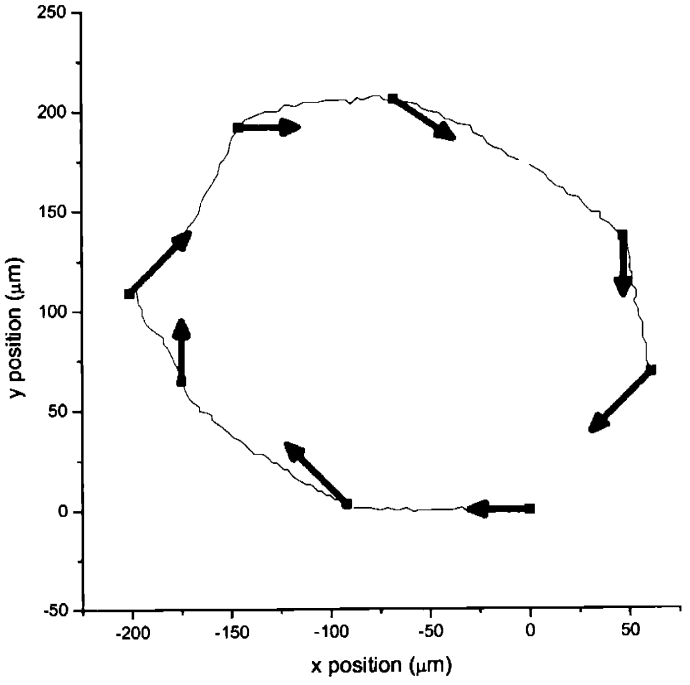

(b)

Figure 4.1: (a) Electric fields applied between x- and y- oriented electrodes to move particles on the surface. Vectors indicate force exerted on negatively charged particles under three different conditions. Gold electrodes are inactive; red is cathode and black is anode. **(b)** Trajectory traced by a single particle showing magnitude and direction of force. Nodes correspond to a change in applied field.

4.3.2 Parallel Electrodes

The parallel electrodes, initially fabricated using gold metallization, were used to move particles along the surface in the direction of the applied field. Particles were observed to pack directly at the electrode at a pH of 12 as shown in Figure 4.2. The negatively charged silica particles were attracted to the anode, shown at left in the figure. The particles, once collected at the electrode, remained fixed and were not dislodged by subsequent voltage cycles.

A dependence of the mobility of the particles on the ionic strength of the electrolyte was

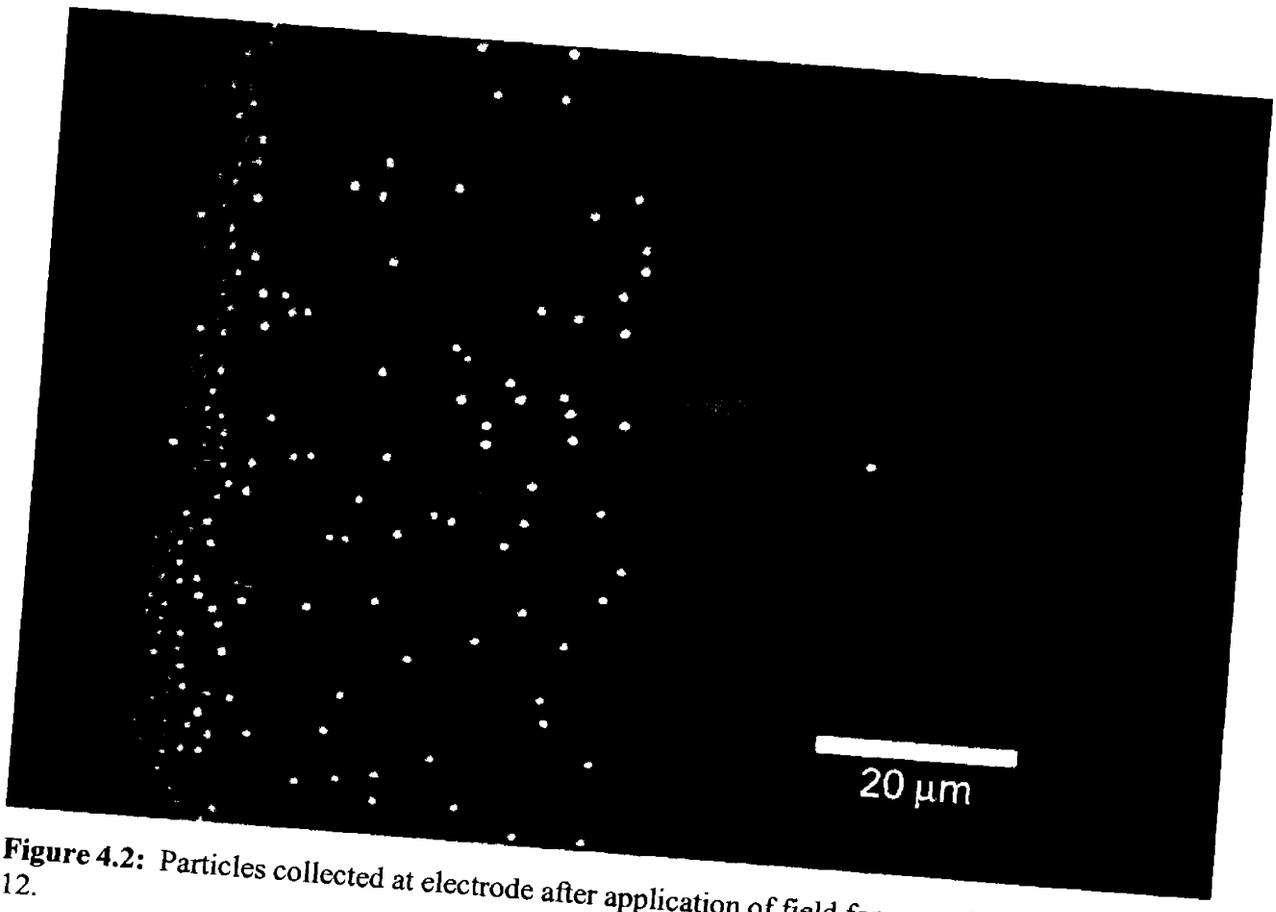

Figure 4.2: Particles collected at electrode after application of field for several seconds at a pH of 12.

also observed. This is shown in Figure 4.3 at pH = 9.8. The particles are seen to move more slowly as the ionic strength is increased, as is expected due to the reduction in zeta potential and hence mobility of the particles in the presence of a greater concentration of dissolved salt. The maximum mobility observed is, however, much lower than that predicted by Equation 4.2. This reduction in mobility is a direct result of the blocking nature of the gold electrodes, as outlined in Section 3.2.2. It was also observed that particles adhered to the surface upon application of the field, with this behavior more pronounced near the cathode. The majority of these bound particles remained immobile even after the field was removed and could not be dislodged during subsequent voltage cycles. This adhesion phenomena will be explored further in Section 4.3.4

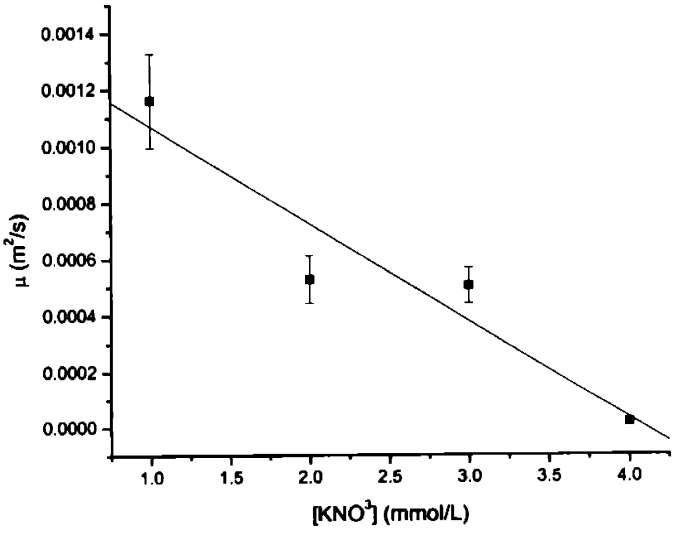

Figure 4.3: Variation in mobility of 1.58 μm silica particles due to applied DC field between microelectrodes as a function of ionic strength. The field was 3500 V/m.

4.3.3 AC Field Behavior

Initially randomly distributed particles settled on the surface were observed to form chains oriented parallel to the field lines upon application of an AC field. The chaining effect was not observed with DC fields. The length of the particle chains was seen to depend on the frequency of the input signal. The chains were much smaller at the lower frequency as shown in Figure 4.4(a) and (b).

The formation of chains is explained by the interaction of dipoles induced by the uniform AC field with a non-uniform field created in the vicinity of the particles due to perturbations at the particle-fluid interface. Such perturbations will occur provided that a significant dielectric contrast between the particles and the suspension medium exists. This results in both particle motion and mutual attraction of neighboring particles. The so-called chaining of neighboring particles was first studied in magneto- and electrorheological fluids and has also been observed with suspensions of dielectric spheres in aqueous and non-aqueous media [96][97]. The orientation of particles θ relative to the applied field and separated by a distance r will determine the nature of their repulsive or attractive potential according to:

$$U(r,\theta) = \beta^2 \varepsilon_r \frac{(a^3 E)^2 (1 - 3\cos^2\theta)}{r^3} \qquad \textbf{(4.3)}$$

where the effective polarizability β depends on the dielectric constants of the fluid and particles ε_p and ε_f, respectively:

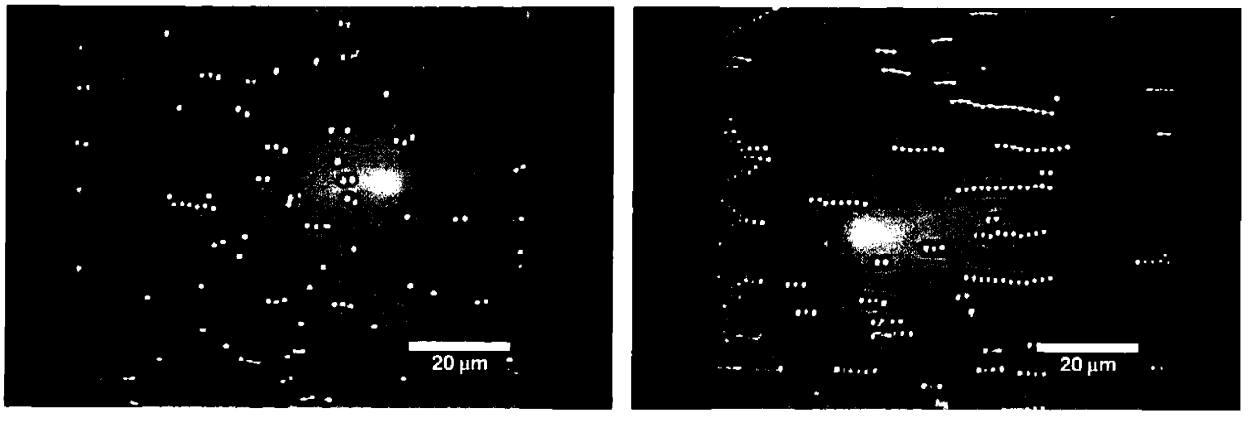

(a) **(b)**

Figure 4.4: Chaining of particles between an applied AC field at **(a)** 10 Hz and **(b)** 1 kHz. The pH was 11.

$$\beta = \frac{\varepsilon_p - \varepsilon_f}{\varepsilon_p + 2\varepsilon_f} \qquad (4.4)$$

A shift in the potential from attractive to repulsive occurs at orientation angles greater than 55°, as illustrated schematically in Figure 4.5 [98].

Characteristic packing of the particles at the electrodes was also observed, suggesting that the dominant force for particle motion is electrophoretic in nature even though DEP is responsible for the formation of chains. The adhesion effect was also observed in AC field experiments at lower frequencies. This may be due to polarization effects at the electrodes that are less pronounced as the frequency is increased.

4.3.4 Electrophoretic Deposition Experiments

Initial results of electrophoretic deposition experiments between as-deposited, parallel platinum electrodes at the larger interelectrode spacing resulted in a mean particle velocity of 3.1 ± 0.26 μm/s, as measured at a point midway between the electrodes. This value is substantially lower than the theoretical value of 25 μm/s expected from Equation 4.2. Subsequent experiments using blackened platinum electrodes resulted in a much greater velocity of 24.8 ± 6.1 μm/s, equivalent to the theoretical value. This increase in velocity was accompanied by a large increase

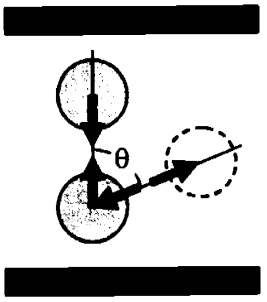

Figure 4.5: Attractive or repulsive potential induced between two spherical particles oriented at an angle θ to uniform applied field.

in current, as shown in Figure 4.6. The increase in current is consistent with the improved performance of the non-polarizable, blackened platinum electrodes, offering a substantial increase in exchange current density at the electrode-fluid interface and a corresponding reduction in the

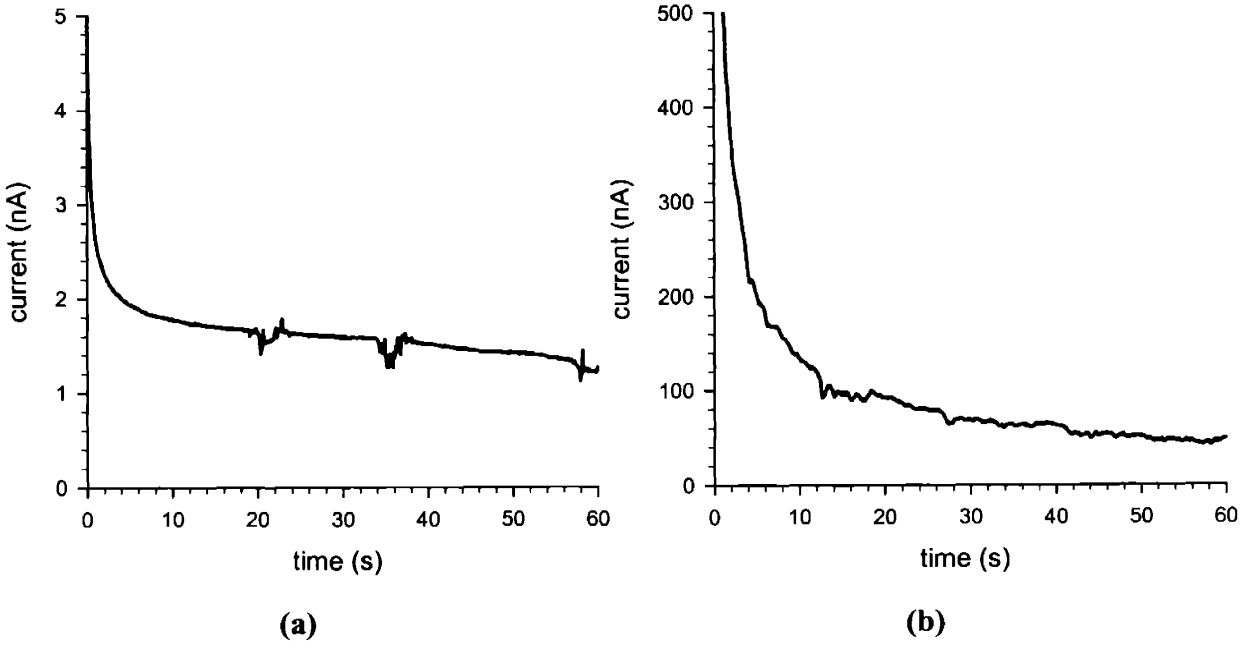

Figure 4.6: Time-dependent current for **(a)** as-deposited electrodes and **(b)** blackened electrodes, showing substantial increase in current for reversible case.

interface resistance. Figure 4.7 shows the measured particle velocity as a function of the applied potential for the blackened electrode case, with a linear dependence as predicted by Equation 4.2. The dependence of velocity on field strength observed with the as-deposited electrodes was, in contrast, quite erratic, owing to the variability caused by the high interface resistance at the electrodes. Proper preparation of the electrodes to ensure reversibility is obviously necessary in order to achieve the maximum theoretical velocity. Therefore, only blackened electrodes were used for subsequent experiments.

The situation directly at the electrodes was quite different. Only a few particles achieved the goal of deposition onto the working electrode under constant potential conditions. The vast majority adhered to the sapphire substrate at all applied potentials, with a substantial increase in the rate of adhesion observed with increasing voltage. Comparing the two extreme conditions of 1 and 5 volts, the adhesion at the higher field strength was so rapid that measurement of the velocity was not possible, as the ability to detect motion before the particles became fixed to the substrate was compromised by the relatively low frame rate of image acquisition. High speed imaging

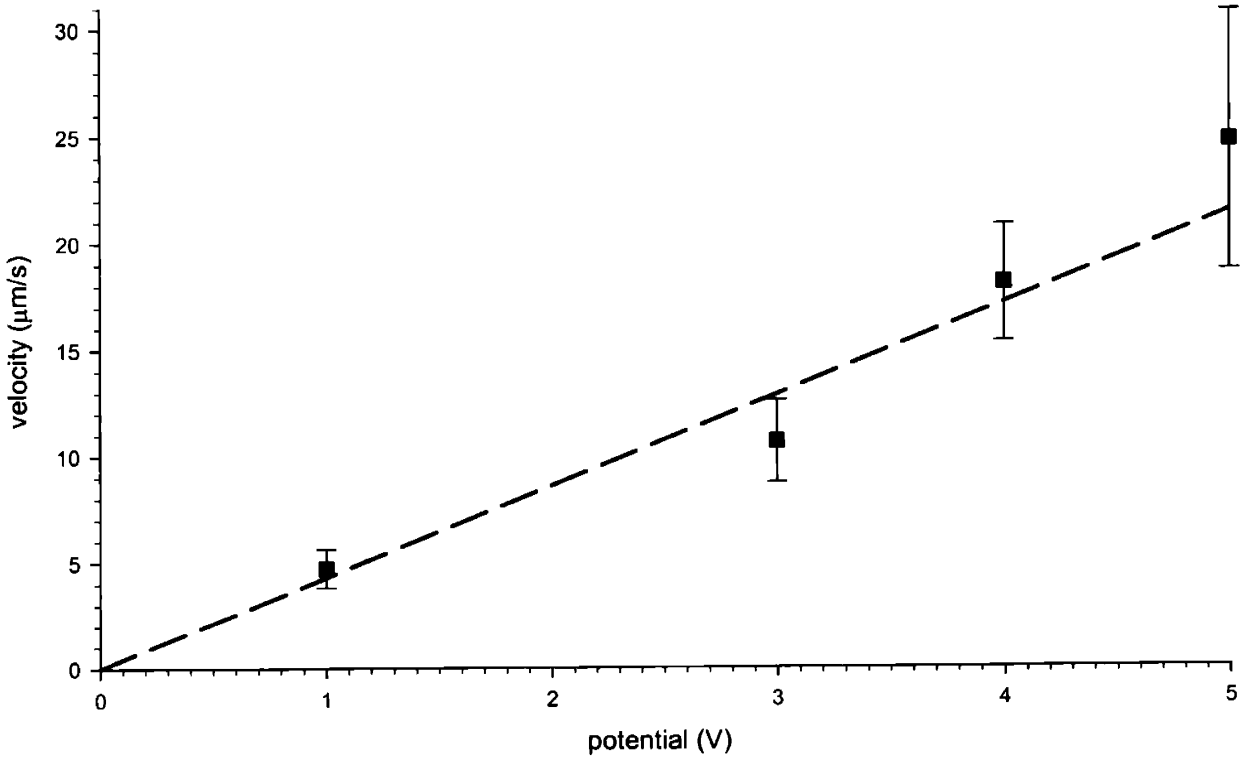

Figure 4.7: Linear variation of particle velocity with field strength measured midway between the electrodes for constant potential experiments. The theoretical velocity calculated from Equation 4.2 is given by the dotted line.

using strobe lighting or other rapid shutter techniques would be necessary to accurately measure the particle velocity at extreme potentials. The velocity at 1 volt was, however, accurately measured to occur between 2-4 μm/s as compared with the constant velocity recorded at a point midway between the electrodes. Particles immediately began moving rapidly in the direction of the applied field until adhered as they approached the electrode. The velocity of particles further from the electrode continued to decrease, resulting in an increase with time in the distance from the electrode at which the particles were fixed to the substrate, as show in Figure 4.8. Considering the relative zeta potentials of the particles and substrate provides an explanation for both the decrease in velocity and the time rate of adhesion. The electrokinetic characterization of the silica particles and sapphire surface presented in Section 2.3 and Section 2.5 reveals that the two surfaces have a charge opposite in sign below the i.e.p. of the sapphire. Adhesion would be expected below this critical pH due to the surface charge interaction, suggesting that a local reduction in pH results from the application of the potential during EPD. This is due to the production of potential determining ions at the working electrode, where the relevant reaction is:

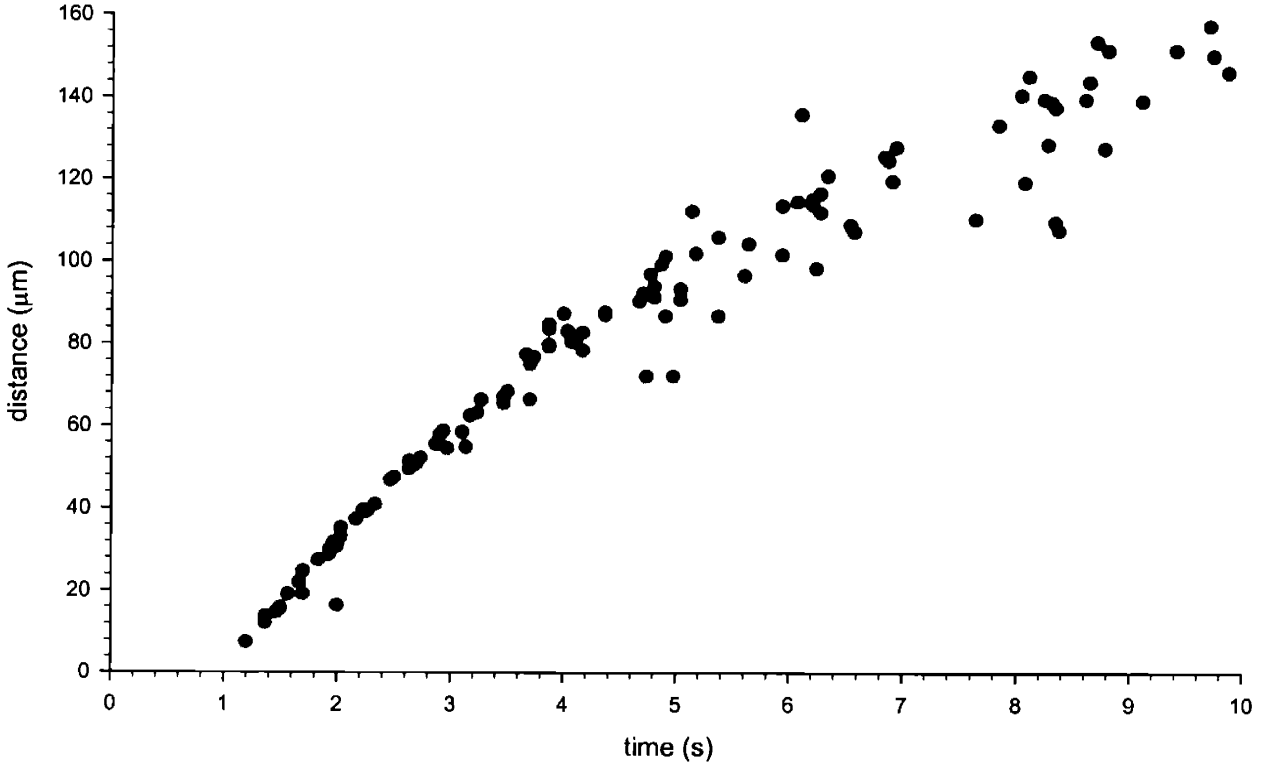

Figure 4.8: Distance from electrode at which all particles became adhered as a function of time for a constant potential of 1 V.

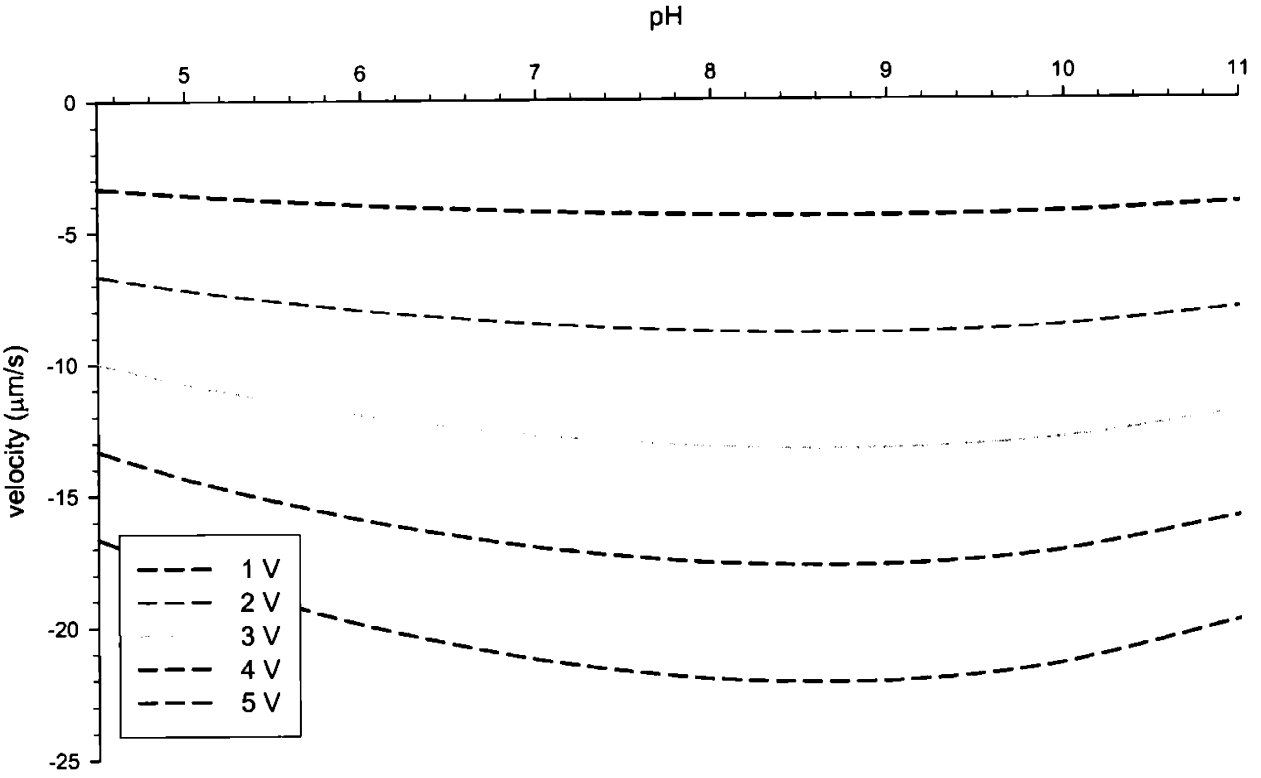

Figure 4.9: Maximum theoretical velocity as a function of pH and applied potential for silica particles moving adjacent to a sapphire substrate. The x-axis scale corresponds to the pH range over which motion is possible, where the particles and substrate are both negatively charged.

$$H_2O \rightarrow 2H^+ + \frac{1}{2}O + 2e^- \qquad \textbf{(4.5)}$$

The hydrolysis of water to produce at the working electrode results in a local decrease in the pH, causing particles to adhere to the surface. The experimentally observed reduction in velocity follows directly from Equation 4.2, as illustrated in the plot of maximum theoretical velocity as a function of pH and applied potential (Figure 4.9). Here the zeta potential data and calculated field strength from Figures 2.1, 2.10, and 3.5 were input directly to calculate the theoretical velocities. The plot indicates a substantial reduction in silica particle velocity as the pH approaches and

passes below the i.e.p. of the sapphire substrate. Hence the reduction in pH at the electrodes changes the relative magnitude of the particle and substrate zeta potentials, causing the particles to move more slowly as they reach the electrode-solution interface.

A handful of particles were successfully brought to the electrode under constant current conditions at 500 nA, as shown below in Figure 4.10(a). The deposition stage was followed by substantial adhesion of the particles to the sapphire surface, indicated in Figure 4.10(b). The distance from the electrode at which particles became adhered was linear in time, deviating from the

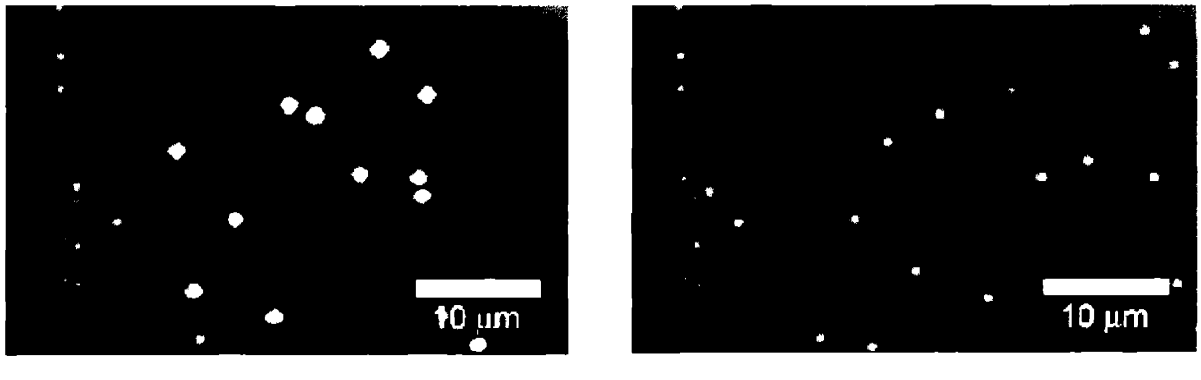

(a) **(b)**

Figure 4.10: Deposition of particles near blackened electrodes after **(a)** 5 sec and **(b)** 10 sec, showing the distance at which particles become adhered. Emphasis has been added to the mobile particles at left for clarity; adhered particles are shown without emphasis.

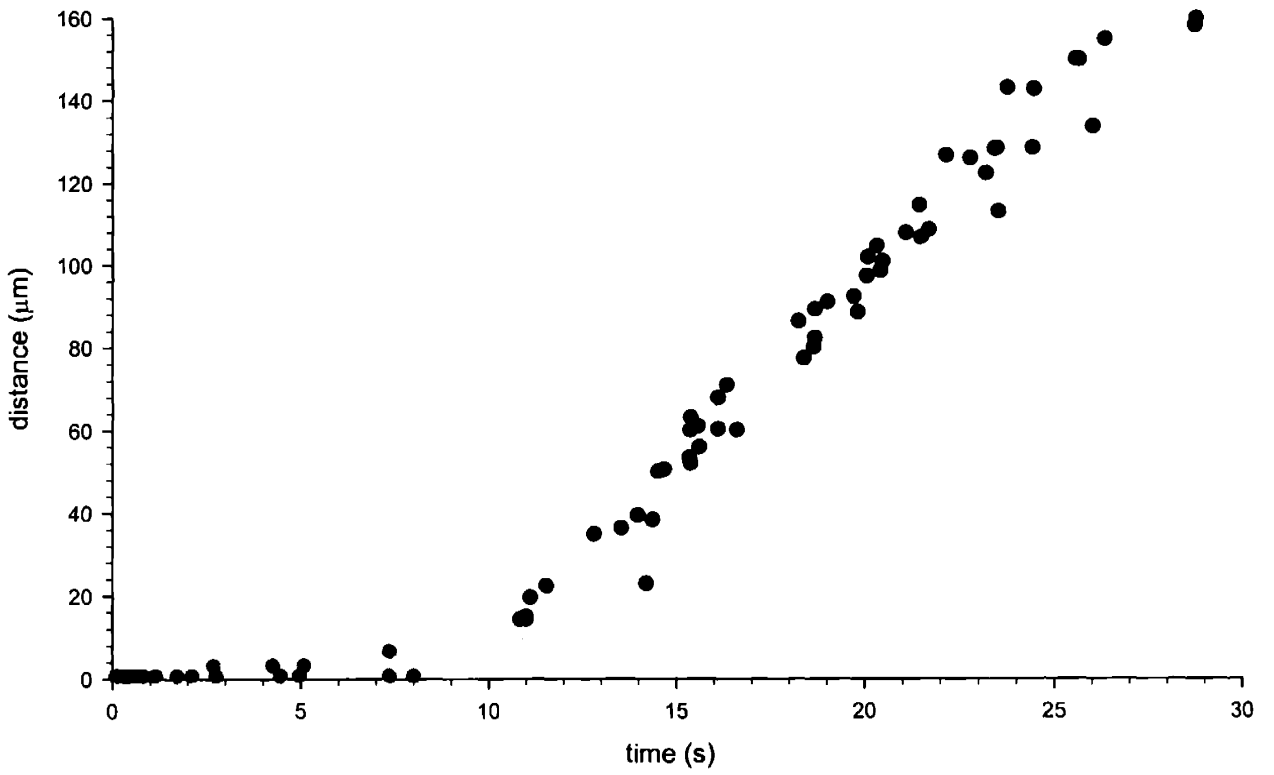

Figure 4.11: Distance from electrode at which all particles became adhered as a function of time for the constant current experiment at 500 nA. Particles which reached the electrode are shown in green while the remaining particles adhered to the substrate before reaching the electrode are shown in red.

behavior observed under constant potential conditions. This result is plotted in Figure 4.11, with the particles reaching the electrode shown in green. An increase in the voltage as a function of

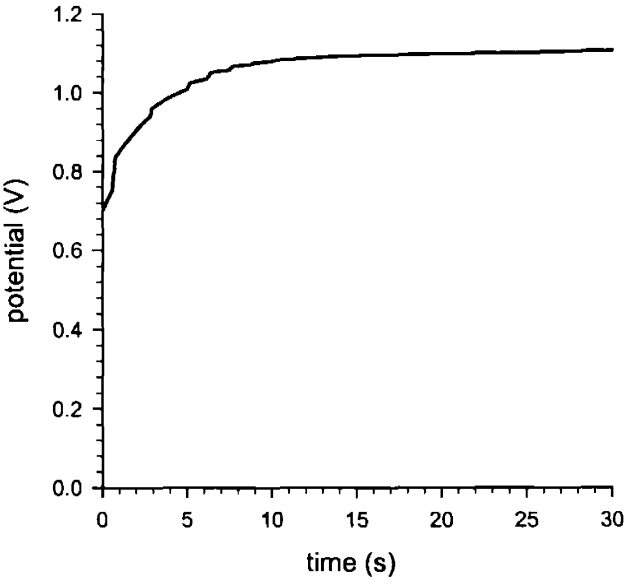

Figure 4.12: Time-dependent potential for constant current experiment at 500 nA using blackened electrodes

time was also measured and is displayed in Figure 4.12. This potential increase is necessary to maintain a constant current throughout the experiment. The production of potential determining ions at the working electrode will be explored further in the next section.

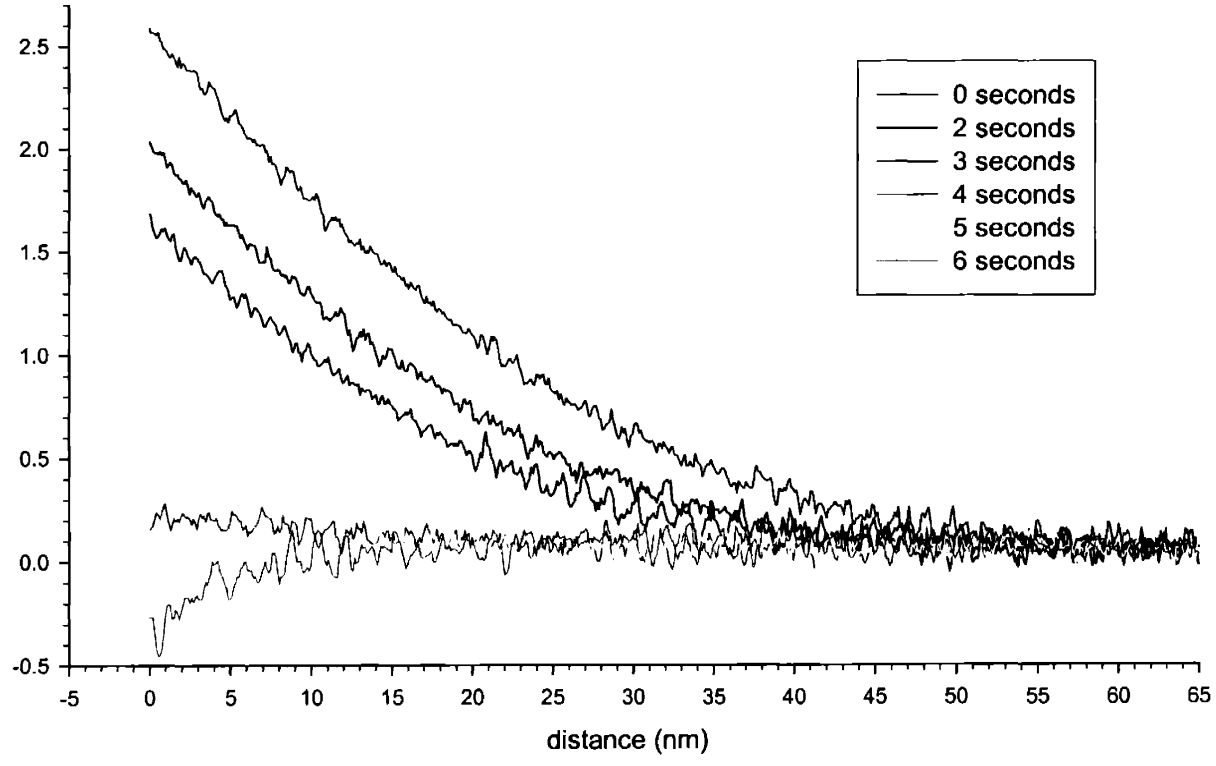

Figure 4.13: Complete force vs. distance curves plotted at various times as measured at a distance of 25 m from the anode at an applied potential of 500 mV.

4.3.5 Atomic Force Microscopy

Characteristic force-distance curves measured at different times after the potential was applied are plotted in Figure 4.13, indicating an immediate reduction in the peak force after the potential was first turned on. Curves from all times were analyzed using an automated processing routine written in Matlab (see Appendix A) to determine the peak force as a function of time at the various distances studied. A summary of these results for the constant current experiment is

shown in Figure 4.14, where the force has been integrated to illustrate the reaction at the electrode in terms of the work required to bring the colloid probe to the sapphire surface. This work of adhesion diminishes rapidly at all three distances from the electrode before reaching a steady-state value, consistent with a local change in pH due to the Farradaic production of hydrogen ions at the anode. The repulsive interaction between the colloid probe and the surface, both negatively charged above the i.e.p. of sapphire, accounts for the increase in the positive work of adhesion upon approach of the probe. A reduction in the work as a function of time reflects the decrease in pH during the application of the potential at constant current, leading in turn to a reduction in the

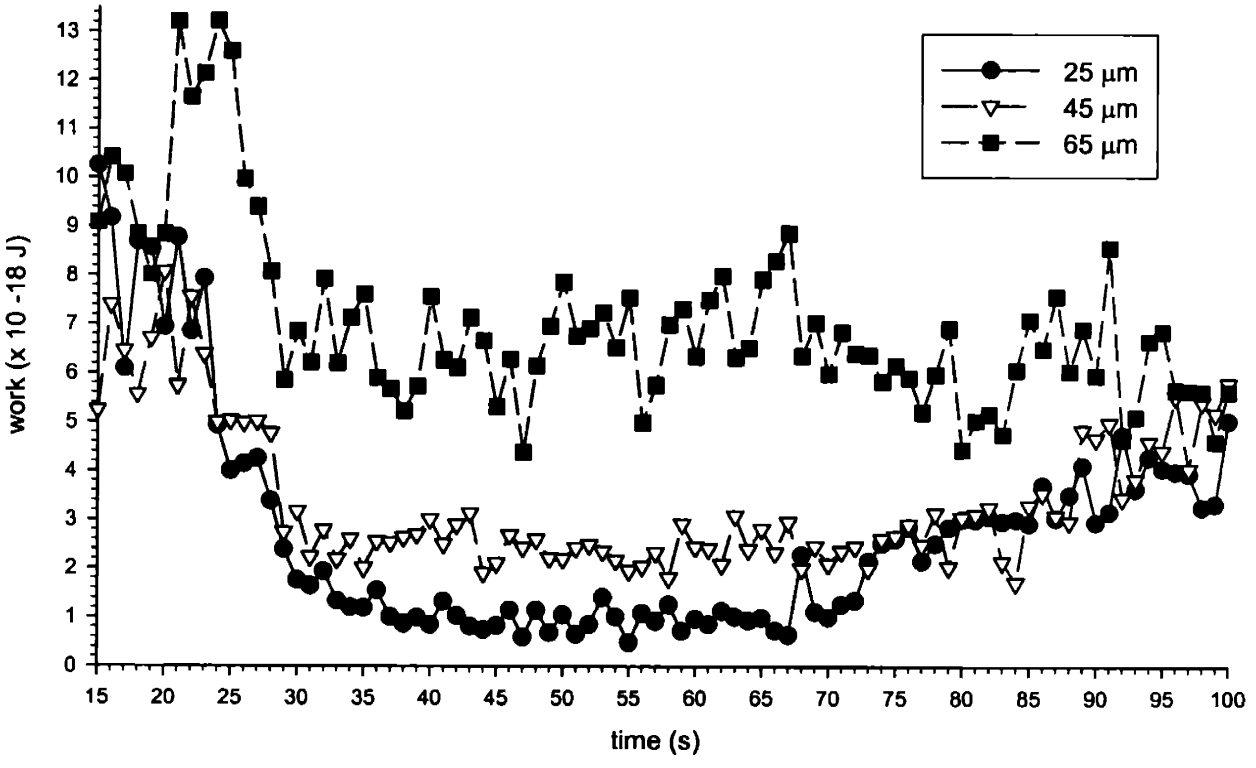

Figure 4.14: Work of adhesion plotted against time for the constant current AFM experiments at multiple distances from the electrode. The grayed area shows the time over which the potential was applied.

zeta potential of both the sapphire surface and silica particle. Also consistent with these observations is the gradual increase in the work after the potential was turned off, reflecting a return of the fluid surrounding the electrode to the bulk pH.

Results of a similar experiment conducted at applied potentials of 500 and 1000 mV are

shown in Figures 4.15, and 4.16. The former shows little change in the work of adhesion as a

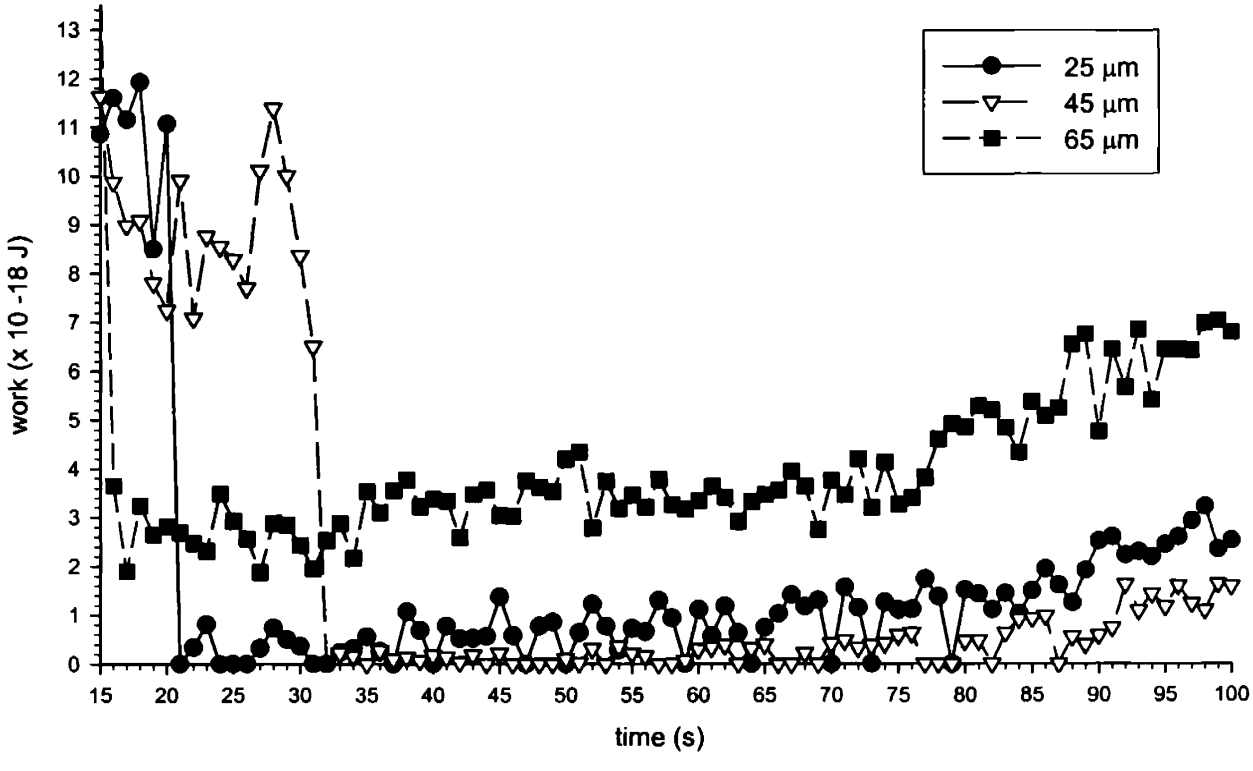

Figure 4.15: Work of adhesion plotted against time for the 1000 mV constant potential AFM experiments at multiple distances from the electrode. The grayed area shows the time over which the potential was applied.

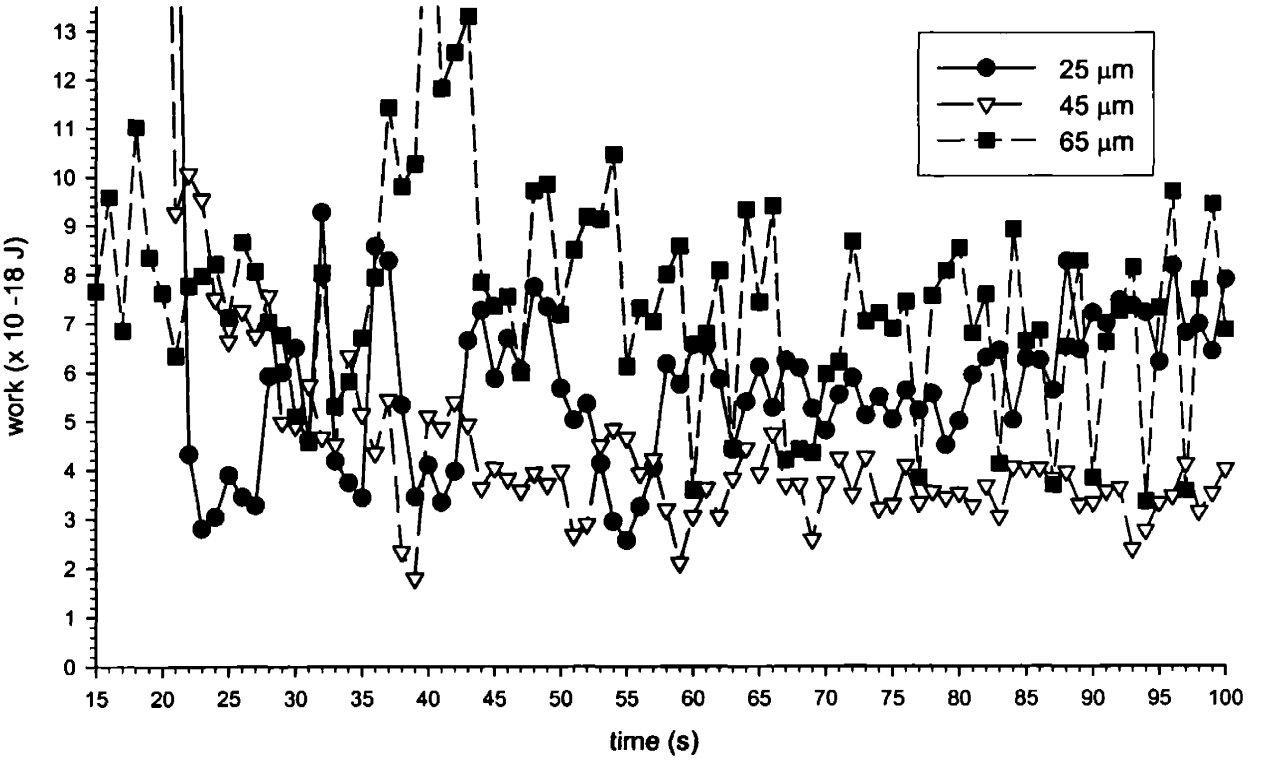

Figure 4.16: Work of adhesion plotted against time for the 500 mV constant potential AFM experiments at multiple distances from the electrode. The grayed area shows the time over which the potential was applied.

function of time, as would be expected at a fairly low potential. A dramatic decrease occurs at all distances at a potential of 1000 mV, suggesting a critical potential above which the system must be operated in order to see substantial reduction in the pH.

Figure 4.14 also shows a decrease in the steady-state work of adhesion with increasing distance from the electrode during application of the potential. This observation is consistent with the results of the EPD experiments under constant current conditions and can be explained by the development of a steady-state H^+ diffusion profile. The time required for the particles to adhere to the sapphire substrate increases with distance from the electrode, just as the work of adhesion is decreased. These spatial differences are directly related to a local reduction in pH and reflect a decreasing hydrogen ion concentration gradient moving away from the working electrode. Such a gradient is characteristic of the steady state electrochemical conditions under which these experiments were performed, and appears very rapidly across the system due to the rapid diffusivity of H^+ in the aqueous solution. A time-dependent finite element analysis with a constant surface flux

of hydrogen ions was employed to validate this model. A characteristic plot of the hydrogen ion concentration as a function of distance from the electrode at one timestep is shown in Figure 4.17. The resulting pH (calculated directly from the simulation concentration of hydrogen ions) is

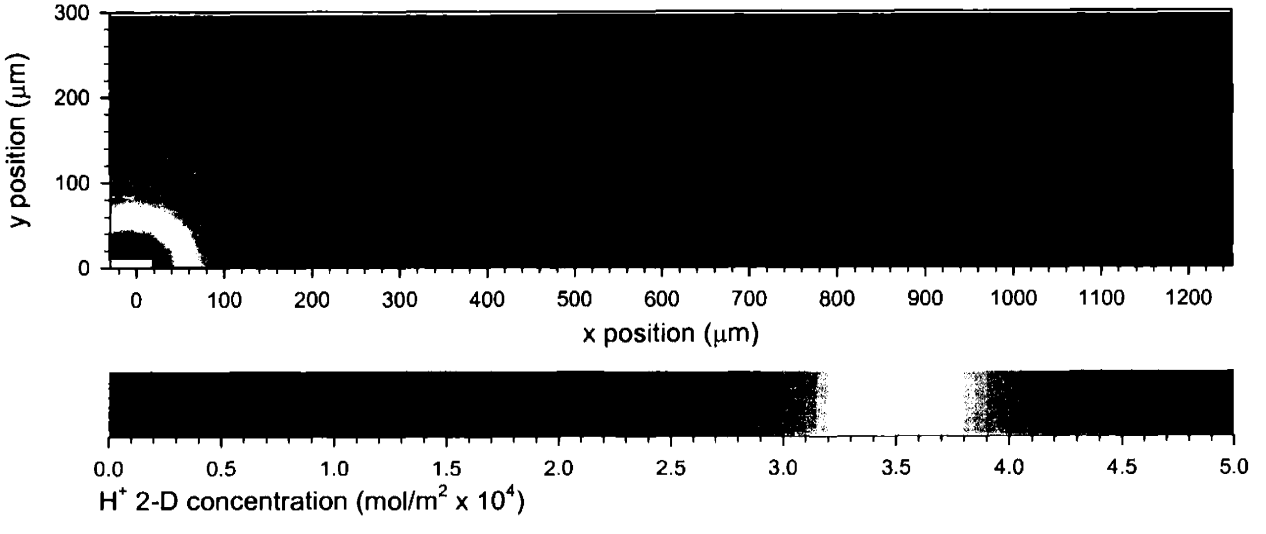

Figure 4.17: Contour plot of hydrogen ion concentration near the parallel electrodes at a time of 60 seconds, showing dramatic increase in concentration gradient at the electrode surface that diminishes rapidly into the bulk fluid.

shown in Figure 4.18 as a function of time for the three distances studied experimentally. The curves show a rapid reduction in pH at all distances within a few seconds, after which time the rate of change of pH slows dramatically. More significant is the change in the steady-state pH as a function of distance, with the lowest pH occurring closest to the electrode as expected. The pH reduction is less substantial at 45 and 65 μm though still significant. The spatial reduction in pH is not, however as dramatic in the over-simplified simulation as is observed in both the AFM and EPD experiments. This diffusion-based model is therefore insufficient to accurately predict the expected reduction in pH to near the i.e.p. of the sapphire substrates.

We consider as an additional explanation the fluid flow behavior at the sapphire surface, outlined in Section 4.1. The positively charged ions located outside of the Debye layer directly adjacent to the surface move in the opposite direction as the negatively charged particles at pHs

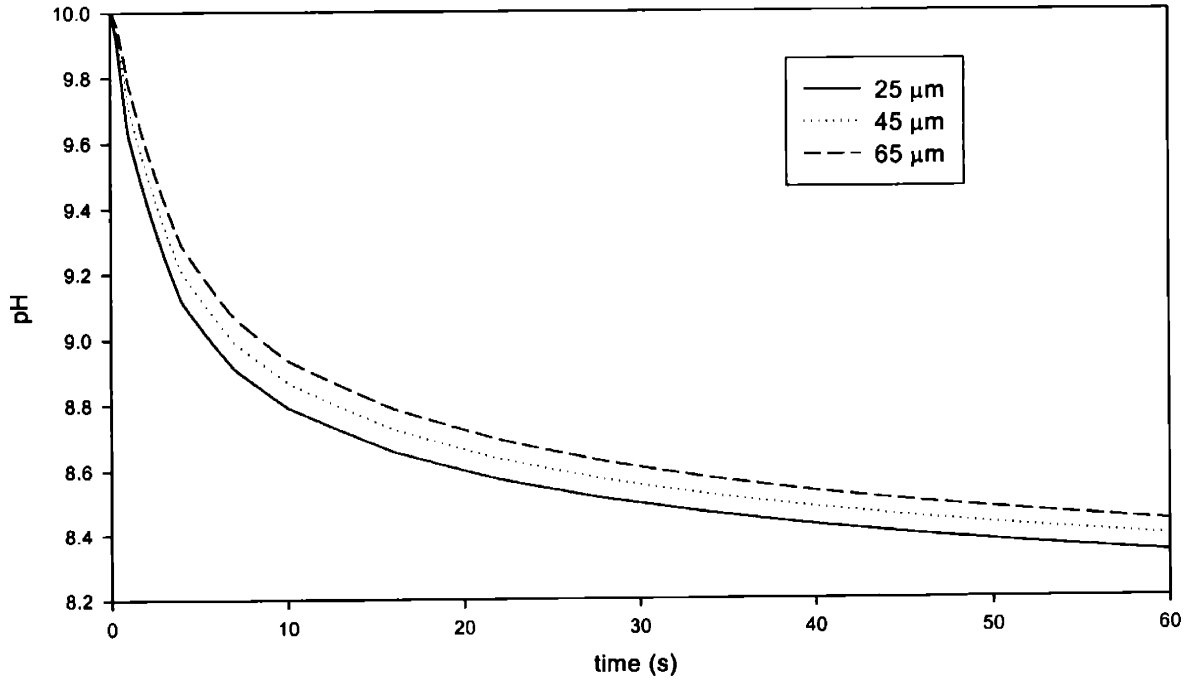

Figure 4.18: Results of finite element model, illustrating the rapid decrease in pH as a function of time. A smaller change is observed as a function of distance.

greater than the i.e.p. of the sapphire. This is illustrated in Figure 4.19, where the resulting flow profile corresponding to a no-slip condition at the fluid-substrate interface is shown schematically. Equation 4.1 may be then applied to this layer of adsorbed ions to predict the velocity of the fluid, v_∞ independent of the motion of the particles. The position of a test charge within this fluid front, which moves in the opposite direction from the particles, has been plotted as a func-

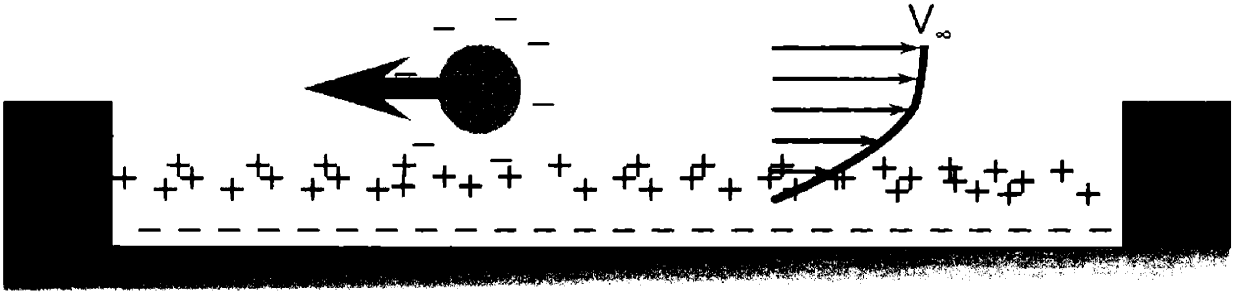

Figure 4.19: Schematic of negatively charged Debye layer at the fluid-sapphire interface, bounded by positively charged ions. The resulting velocity profile of fluid flowing away from the positively charged working electrode is indicated.

tion of time in Figure 4.20. Here the time rate of adhesion for the constant current experiment is superposed, showing a striking similarity between the distance at which the particles begin to adhere and the distance the fluid travels in a given amount of time. The positive potential determining ions produced at the working electrode are therefore swept rapidly into solution by the moving fluid front, thus reducing the pH as a function of distance away from the electrode. It should be expected that the time rate of adhesion of the silica particles will be directly related to the local pH. The expression for the interaction potential between a silica particle and single crystalline α-Al_2O_3 substrate was introduced in Section 2.1.2. This potential exhibits a maximum at some separation distance greater than zero. The maximum, which decreases with decreasing pH, represents an energetic barrier to adhesion. It follows that the kinetics of adhesion will be directly related to the magnitude of the potential energy barrier, with particles experiencing a lower local pH requiring less time before adhering to the substrate. Such is the effect observed in the experiments.

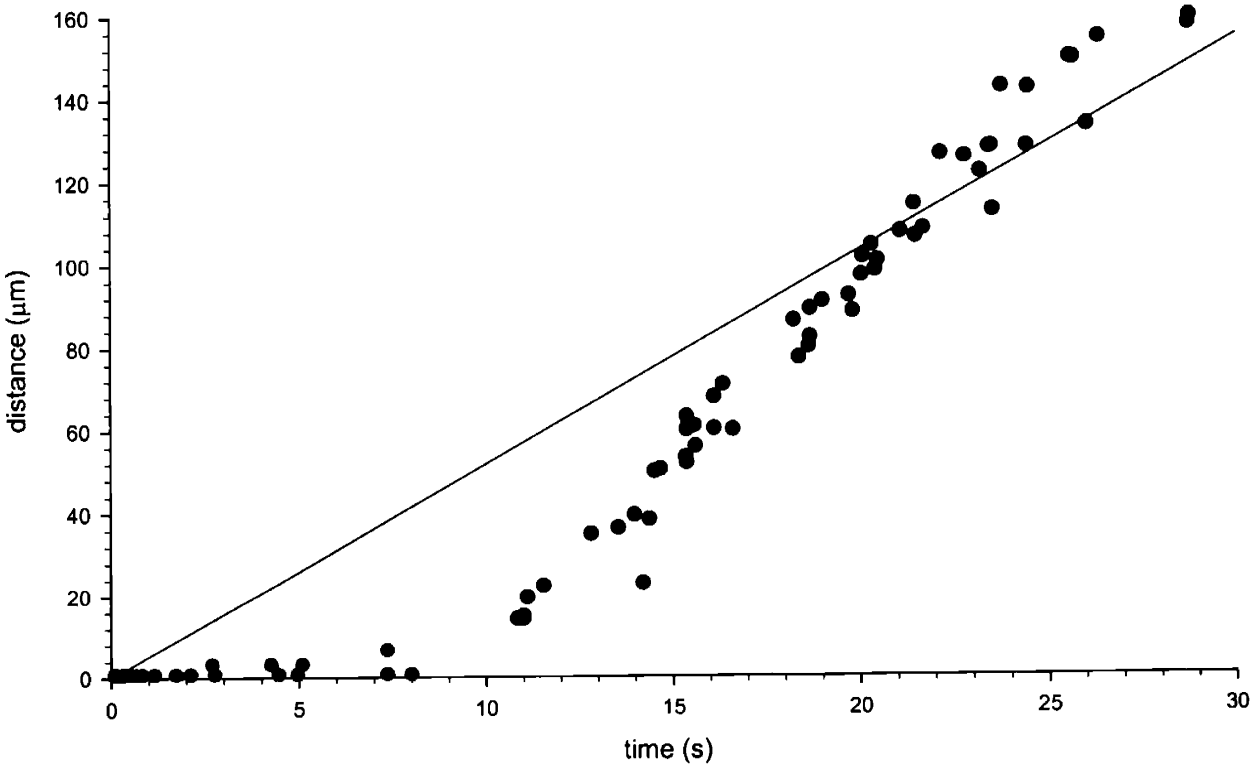

Figure 4.20: Plot of fluid distance from electrode as a function of time (blue line), with distance at which particles became adhered at each time superposed.

4.4 Conclusions

The *in-situ* observation of EPD has been demonstrated and used to image the electrophoresis of particles far from the electrode and their deposition onto the electrode. Experimental results demonstrate that the reversibility of the electrodes, introduced in Chapter 3, plays a significant role in both the transport and deposition steps. Properly prepared electrodes were necessary in the microelectrode experiments to improve the reproducibility and achieve particle velocities near the value expected by theory. Comparisons of particle velocities midway between the electrodes and directly near them indicate that particles are slowed substantially as they reach the electrode. The particles were also observed to adhere to the sapphire substrate as they approached the electrode under both constant current and constant potential conditions. The hydrolysis reaction proceeded even though the concentration of gas produced as a result was low enough to avoid the nucleation of bubbles. AFM force-distance curves using a colloidal probe technique were measured at various distances from the electrode during application of an externally applied potential. The peak force and hence the work necessary to move the colloid probe towards the sapphire substrate decreased immediately after application of the potential, reaching a steady-state value after just a few seconds. This steady-state work of adhesion was seen to decrease most substantially closest to the electrode, indicative of a local pH gradient that further validates the observed adhesion during EPD. The pH gradient was also responsible for an experimentally observed reduction in velocity as the particles moved towards the electrode. These results are significant to the understanding of the mechanisms active during EPD, and point to an agglomeration mechanism at the electrode that is responsible for deposition.

Chapter 5: Conclusions and Future Work

5.1 Summary of Major Findings

The preceding pages have detailed the successful fabrication and implementation of a device capable of manipulating micron scale particles using an externally applied electric field. A model system of micron scale particles suspended in an aqueous medium was used to investigate the role of surface forces during particle motion adjacent to a sapphire substrate of known surface chemistry. Complete electrokinetic characterization of the sapphire substrate, presented in Chapter 2, illustrated a dramatic shift in the i.e.p. as a function of orientation of the single crystals. This observation, that surface chemistry is dictated not only by the surrounding fluid but also by *structural* changes in the surface itself, has far-reaching implications for any system where small bodies and fluids are caused to move near a substrate. The orientation dependence of the zeta potential also sheds light on the long-standing debate in the literature regarding the exact chemistry of the pure α-alumina surface. The results presented here conclusively demonstrate a significantly lower i.e.p. than that traditionally accepted and suggests that the composition of the single crystalline sapphire surface may be strikingly different from that of polycrystalline particles.

Electrophoretic deposition experiments were conducted both at constant current and constant potential. Reversibility of the electrochemical system comprising the working electrode, counter electrode, and suspension medium was shown to be significant in achieving the maximum theoretical velocity during EPD. The same model system was used to deposit silica particles at the electrode. Substantial adhesion to the surface was observed very near the electrodes, and colloidal probe atomic force microscopy was employed to investigate the interaction force between a silica particle and the sapphire surface. This was coupled with finite element modelling to reveal that a modest decrease in pH due to diffusion is predicted to occur immediately after application of a constant current. The velocity of the fluid, however, illustrates a remarkable similarity to the time rate of adhesion of particles, suggesting that fluid convection is in fact responsible for the reduction in pH and the resulting adhesion of particles. Similar AFM results were obtained for the constant potential experiments, also showing a decrease in the work required to bring the silica particle to the sapphire surface. This behavior was also observed to be dependent on the magnitude of the applied potential. These significant findings have contributed greatly to the understanding of both the commercial electrophoretic deposition process and the role of surface

forces during assembly of particles on the micron scale. Nevertheless additional experiments could serve to advance the work presented here even further, possibly leading to direct applications of this work to a new industrial assembly process.

5.2 Future Work

5.2.1 Surface Characterization

The results of streaming potential experiments on sapphire wafers presented here were conducted over a full range of pH and ionic strength. This thorough assessment, coupled with XPS and AFM analysis of the exact composition and roughness of the surface, is sufficient to conclusively demonstrate the acidity of all three crystal orientations studied. An additional study may, however, provide further evidence of the more basic behavior of α-Al_2O_3 particles and reveal crucial information about the exact composition of the surface layer. Streaming potential measurements of pure sapphire surfaces subjected to a variety of controlled conditions, coupled with low-angle x-ray scattering could therefore be envisioned to investigate this phenomenon further.

5.2.2 Device Fabrication

The relatively simple device presented in this work resulted from a substantial effort of cleanroom process optimization. Further improvements are possible, however, to solve practical issues such as delamination of metal from the sapphire substrate during wire bonding of electrical contacts. Bernhardt *et al.* present the successful use of zinc as an adhesion layer prior to primary metallization [99]. This approach has been demonstrated to be superior to the titanium and chromium layers more commonly used in microelectronics and MEMS processing on silicon. Additional benefit could also be derived from an overhaul of the trace and bond pad design to incorporate larger areas for bonding, thus incorporating a fault tolerant approach that would allow for some level of delamination without the need to discard entire devices prematurely. Other device designs could be envisioned which take advantage of the findings of this thesis to both manipulate and place particles in specific locations on a surface. One such design might, for example, incorporate patterned regions having different surface chemistries coupled with microelectrodes deposited on the surface. The electrodes could be used to electrophoretically deposit particles on these regions of patterned surface charge, thus dictating the precise placement of particles.

5.2.3 Other Particles and Surfaces

The selection of a model system allowed the surface chemistry of the silica and sapphire particles to be thoroughly characterized. This analysis could then be directly applied to the study of surface forces during electrophoretic assembly. This work could also be extended easily to other systems of more practical significance. The microelectrodes could easily be patterned on, for example, silicon or quartz surfaces. The streaming potential technique used here could also be adapted to these surfaces. Different crystallographic orientations of silicon could be studied to determine the dependence of the zeta potential on the structural properties of additional information. Still other particles could be considered for electrophoretic assembly, including functionalized surfaces and biological macromolecules. One interesting example is the single crystalline α-Al_2O_3 used as a comparison to the planar sapphire substrates in Section 2.5.5.

5.3 Outlook

The results presents in this thesis have far reaching significance for applications ranging from traditional ceramics processing to catalysis and microfluidics, where complete knowledge of the charge on the substrate is paramount to understanding the complex processes which occur at the fluid-liquid interface. The reported dependence of surface charge behavior on the structure of the surface also open up new possibilities for controlling the interaction of particles and other macromolecules with the substrate, potentially providing new methods for templating and assembly of ordered structures.

References

1. Tarhan, I. Inanc; Watson, George H. *Physical Review Letters* (1996), 76(2), 315-18.

2. Joannopolous, J.D., Meade, R.D., Winn, J.N., *Photonic Crystals: Molding the Flow of Light*, Princeton University Press, Princeton, NJ (1995).

3. Joannopoulos, J. D.; Villeneuve, Pierre R.; Fan, Shanhui. *Nature* (1997), 386(6621), 143-149.

4. Vlasov, Yuril A.; Bo, Xiang-Zheng; Sturm, James C.; Norris, David J. *Nature* (2001), 414(6861), 289-293.

5. Braun, Paul V.; Wiltzius, Pierre. *Nature* (1999), 402(6762), 603-604.

6. Wijnhoven, Judith E. G. J.; Vos, Willem L. *Science* (1998), 281(5378), 802-804.

7. mhof, A.; Pine, D. J. *Nature* (1997), 389(6654), 948-951.

8. Velev, Orlin D.; Kaler, Eric W. *Advanced Materials* (2000), 12(7), 531-534.

9. Norris, David J.; Vlasov, Yurii A. *Advanced Materials* (2001), 13(6), 371-376.

10. Kumar, Amit; Biebuyck, Hans A.; Whitesides, George M. *Langmuir* (1994), 10(5), 1498-511.

11. Wilbur, James L.; Kumar, Amit; Biebuyck, Hans A.; Kim, Enoch; Whitesides, George M. *Nanotechnology* (1996), 7(4), 452-457.

12. Aizenberg, Joanna; Braun, Paul V.; Wiltzius, Pierre. *Physical Review Letters* (2000), 84(13), 2997-3000.

13. Yang, Peidong; Deng, Tao; Zhao, Dongyuan; Feng, Pingyun; Pine, David; Chmelka, Bradley F.; Whitesides, George M.; Stucky, Galen D. *Science* (1998), 282(5397), 2244-2247.

14. Chen, Kevin M.; Jiang, Xueping; Kimerling, Lionel C.; Hammond, Paula T. *Langmuir* (2000), 16(20), 7825-7834.

15. Nikolaides, M. G.; Bausch, A. R.; Hsu, M. F.; Dinsmore, A. D.; Brenner, M. P.; Gay, C.; Weitz, D. A. *Nature* (2002), 420(6913), 299-301.

16. Holland, Brian T.; Blanford, Christopher; Stein, Andreas. *Science* (1998), 281(5376), 538-540.

17. Cooper, K. A.; Yang, R.; Mottet, J. S.; Lecarpentier, G. Proceedings - Electronic Components & Technology Conference (1998), 48th, 176-180.

18. Miyazaki, H.; Sato, T. *Advanced Robotics* (1997), 11, 169-185.

19. Verma, A. K.; Hadley, M. A.; Yeh, H. J.; Smith, J. S. *Proceedings - Electronic Components & Technology Conference* (1995), 45th, 1263-1268.

20. Talghader, J. J.; Tu, J. K.; Smith, J. Stephen. *IEEE Photonics Technology Letters* (1995), 7, 1321-1323.

21. Yeh, H. J.; Smith, J. S.; *IEEE Photonics Technology Letters* (1994), 6, 706-708.

22. Mustakis, I.; Clear, S. C.; Nealey, P. F.; Kim, S. *ASME Fluids Engineering. Division Summer Meeting* (1997), 1-8.

23. Rahaman, M. *Ceramic Processing and Sintering.* Marcel Dekker, New York (1995).

24. Bohmer, M. R. *Langmuir* (1996), 12(24), 5747-5750.

25. Trau, M.; Saville, D. A.; Aksay, I. A. Field-induced layering of colloidal crystals. Science (1996), 272(5262), 706-9.

26. Hunter, R.J. *Foundations of Colloid Science*, pp. 317-323, Oxford University Press, Oxford (2001).

27. Hogg, R.; Healy, T. W.; Fuerstenau, D. W. *Transactions of the Faraday Society* (1966), 62(6), 1638-51.

28. Holman, Richard K. *Effects of the polymeric binder system in slurry-based three dimensional printing of ceramics*, MIT PhD Thesis (2001).

29. Larson, I.; Drummond, C. J.; Chan, D. Y. C.; Grieser, F. *Langmuir* (1997), 13(7), 2109-2112.

30. Smit, Willem; Stein, Hans N. *Journal of Colloid and Interface Science* (1977), 60(2), 299-307.

31. Smit, W.; Holten, C. L. M. *Journal of Colloid and Interface Science* (1980), 78(1), 1-14.

32. Horn, R. G.; Clarke, D. R.; Clarkson, M. T. *Journal of Materials Research* (1988), 3(3), 413-16.

33. Ducker, William A.; Xu, Z.; Clarke, David R.; Israelachvili, Jacob N. *Journal of the American Ceramic Society* (1994), 77(2), 437-43.

34. Veeramasuneni, S.; Yalamanchili, M. R.; Miller, J. D. *Journal of Colloid and Interface Science* (1996), 184(2), 594-600.

35. Meagher, Laurence; Maurdev, George; Gee, Michelle L. *Langmuir* (2002), 18(7), 2649-2657.

36. Franks, George V.; Meagher, Laurence. *Colloids and Surfaces A* (2003), 214(1-3), 99-110.

37. Sasaki, Hiroshi; Muramatsu, Atsushi; Arakatsu, Hiroshi; Usui, Shinnosuke. *Journal of Colloid and Interface Science* (1991), 142(1), 266-71.

38. Schwarz, S.; Eichhorn, K.-J.; Wischerhoff, E.; Laschewsky, A. *Colloids and Surfaces A* (1999), 159(2-3), 491-501.

39. Bismarck, Alexander; Kumru, M. Emin; Springer, Jurgen. *Journal of Colloid and Interface Science* (1999), 217(2), 377-387.

40. Bellmann, C.; Opfermann, A.; Jacobasch, H. J.; Adler, H. J. *Fresenius' Journal of Analytical Chemistry* (1997), 358(1-2), 255-258.

41. Boulange-Petermann, Laurence; Doren, A.; Baroux, B.; Bellon-Fontaine, Marie-Noelle. *Journal of Colloid and Interface Science* (1995), 171(1), 179-86.

42. Schmid, Frederick; Khattak, Chandra P.; Felt, D. Mark. *American Ceramic Society Bulletin* (1994), 73(2), 39-44.

43. Schmid, Frederick; Viechnicki, Dennis J. *Journal of the American Ceramic Society* (1970), 53(9), 528-9.

44. Wyckoff, Ralph W. G. *Crystal Structures. Vol. 2.* 2nd ed. (1964)

45. Gautier, M.; Duraud, J. P.; Pham Van, L.; Guittet, M. J. *Surface Science* (1991), 250(1-3), 71-80.

46. Charig, J. M. *Applied Physics Letters* (1967), 10(5), 139-40.

47. Chang, Chuan Chung. *Journal of Applied Physics* (1968), 39(12), 5570-3.

48. French, T. M.; Somorjai, Gabor A. *Journal of Physical Chemistry* (1970), 74(12), 2489-95.

49. Susnitzky, David W.; Carter, C. B. *Journal of the American Ceramic Society* (1986), 69(9), C217-C220.

50. Baik, S.; Fowler, D. E.; Blakely, J. M.; Raj, R. *Journal of the American Ceramic Society* (1985), 68(5), 281-6.

51. Di Felice, Rosa; Northrup, John E. *Physical Review B* (1999), 60(24), R16287-R16290.

52. Barth, Clemens; Reichling, Michael. *Nature* (2001), 414(6859), 54-57.

53. Jarvis, Emily A. A.; Carter, Emily A. *Journal of Physical Chemistry B* (2001), 105(18), 4045-4052.

54. Vilfan, Igor; Lançon, Frederic; Villain, Jacques. *Surface Science* (1997), 392(1-3), 62-68.

55. Arbab, Mehran; Chottiner, Gary S.; Hoffman, R. W. *Materials Research Society Symposium Proceedings* (1989), 153(Interfaces Polym., Met., Ceram.), 63-9.

56. Guo, J.; Ellis, D. E.; Lam, D. J. *Physical Review B* (1992), 45(23), 13647-56.

57. Ahn, J.; Rabalais, J. W. *Surface Science* (1997), 388(1-3), 121-131.

58. Suzuki, T.; Hishita, S.; Oyoshi, K.; Souda, R. *Surface Science* (1999), 437(3), 289-298.

59. Verdozzi, C.; Jennison, D. R.; Schultz, P. A.; Sears, M. P. *Physical Review Letters* (1999), 82(4), 799-802.

60. Pisani, C.; Causa, M.; Dovesi, R.; Roetti, C. *Progress in Surface Science* (1987), 25(1-4), 119-37.

61. Causa, M.; Dovesi, R.; Pisani, C.; Roetti, C. *Surface Science* (1989), 215(1-2), 259-71. CODEN: SUSCAS ISSN:0039-6028.

62. Puchin, V. E.; Gale, J. D.; Shluger, A. L.; Kotomin, E. A.; Guenster, J.; Brause, M.; Kempter, V. *Surface Science* (1997), 370(2-3), 190-200.

63. Gomes, J. R. B.; Moreira, I. d. P. R.; Reinhardt, P.; Wander, A.; Searle, B. G.; Harrison, N. M.; Illas, F. *Chemical Physics Letters* (2001), 341(5,6), 412-418.

64. Chang, Chuan Chung. *Journal of Vacuum Science and Technology* (1971), 8(3), 500-11.

65. Liu, Ping; Kendelewicz, Tom; Brown, Gordon E., Jr.; Nelson, Erik J.; Chambers, Scott A. *Surface Science* (1998), 417(1), 53-65.

66. Elam, J. W.; Nelson, C. E.; Cameron, M. A.; Tolbert, M. A.; George, S. M. *Journal of Physical Chemistry B* (1998), 102(36), 7008-7015.

67. Nelson, C. E.; Elam, J. W.; Cameron, M. A.; Tolbert, M. A.; George, S. M. *Surface Science* (1998), 416(3), 341-353.

68. Wittbrodt, J. M.; Hase, W. L.; Schlegel, H. B. *Journal of Physical Chemistry B* (1998), 102(34), 6539-6548.

69. Eng, Peter J.; Trainor, Thomas P.; Brown, Gordon E., Jr.; Waychunas, Glenn A.; Newville, Matthew; Sutton, Stephen R.; Rivers, Mark L. *Science* (2000), 288(5468), 1029-1033.

70. Werner, Carsten; Korber, Heinz; Zimmermann, Ralf; Dukhin, Stanislav; Jacobasch, Hans-Jorg. *Journal of Colloid and Interface Science* (1998), 208(1), 329-346.

71. Childress, Amy E.; Elimelech, Menachem. *Journal of Membrane Science* (1996), 119(2), 253-268.

72. Erickson, David; Li, Dongqing; Werner, Carsten. *Journal of Colloid and Interface Science* (2000), 232(1), 186-197.

73. Franks, George V.; Lange, Fred F. *Colloids and Surfaces, A* (1999), 146(1-3), 5-17.

74. Johnson, Stephen B.; Scales, Peter J.; Healy, Thomas W. *Langmuir* (1999), 15(8), 2836-2843.

75. Velamakanni, Bhaskar V.; Lange, Fred F. *Journal of the American Ceramic Society* (1991), 74(1), 166-72.

76. Ascarelli, P.; Moretti, G. *Surface and Interface Analysis* (1985), 7(1), 8-12.

77. Wagner, C. D. *Analytical Chemistry* (1975), 47(7), 1201-3.

78. Wagner, C.D.; Dale, L.H.; Raymond, R.H. *Analytical Chemistry* (1979), 51, 466.

79. Nehasil, V.; Zafeiratos, S.; Matolin, V.; Ladas, S. *Vacuum* (1998), 50, 143-145 .

80. Ealet, B.; Gillet, E.; Nehasil, V.; Moller, P.J. *Surface Science* (1994), 151-157, 318.

81. Stulik, Karel; Amatore, Christian; Holub, Karel; Marecek, Vladimir; Kutner, Wlodzimierz. *Pure and Applied Chemistry* (2000), 72(8), 1483-1492.

82. Bard, A. J.; Faulkner, L. R.; *Electrochemical Methods: Fundamentals and Applications*, John Wiley, New York (2001).

83. Yeh, Syun-Ru; Seul, Michael; Shraiman, Boris I. *Nature* (1997), 386(6620), 57-59.

84. Hayward, R. C.; Saville, A.; Aksay, A. *Nature* (2000), 404(6773), 56-59.

85. Velev, O. D.; Kaler, E. W. *Langmuir* (1999), 15(11), 3693-3698.

86. Pethig, Ronald; Markx, Gerard H. *Trends in Biotechnology* (1997), 15(10), 426-432.

87. Morgan, Hywel; Hughes, Michael P.; Green, Nicolas G. *Biophysical Journal* (1999), 77(1), 516-525.

88. Huang, Y.; Wang, X. B.; Tame, J. A.; Pethig, R. *Journal of Physics D* (1993), 26(9), 1528-35.

89. Cheng, Jing; Sheldon, Edward L., III; Wu, Lei; O'Connell, James P., "Channel-less Separation of Bioparticles on a Bioelectronic Chip by Dielectrophoresis," U.S. Patent Number 6,071,394, Jun. 6, 2000.

90. Hermanson, Kevin O.; Lumsdon, Simon O.; Williams, Jacob P.; Kater, Eric W.; Velev, Orlin D. *Science* (2001), 294(5544), 1082-1086.

91. Sarkar, Partho; Nicholson, Patrick S. *Journal of the American Ceramic Society* (1996), 79(8), 1987-2002.

92. Ramos, Antonio; Morgan, Hywel; Green, Nicolas G.; Castellanos, Antonio. *Journal of Colloid and Interface Science* (1999), 217(2), 420-422.

93. Ramos, A.; Morgan, H.; Green, N. G.; Castellanos, A. *Journal of Physics D* (1998), 31(18), 2338-2353.

94. Hunter, R. J. *Foundations of Colloid Science*, pp. 380-381, Oxford University Press, Oxford (2001).

95. H.J. Keh and J.L. Anderson. *Journal of Fluid Mechanics* (1985), 153, 417.

96. Jones, T. B. *Electromechanics of Particles*, pp. 166-172, Cambridge University Press, Cambridge (1995).

97. Giner, V.; Sancho, M.; Lee, R. S.; Martinez, G.; Pethig, R. *Journal of Physics D* (1999), 32(10), 1182-1186.

98. Gast, Alice P.; Zukoski, Charles F. *Advances in Colloid and Interface Science* (1989), 30(3-4), 153-202.

99. Bernhardt, G.; Silvestre, C.; LeCursi, N.; Moulzolf, S. C.; Frankel, D. J.; Lad, R. J. *Sensors and Actuators B* (2001), B77(1-2), 368-374.

100. R. J. Kershner, J. W. Bullard, M. J. Cima. *Langmuir*, in review.

Appendix A: Matlab Code for Force-Distance Curve Analysis

```
handles.filenamecount=1;
guidata(hObject,handles)

for fileloop = 1:size(handles.files,1)
    fname = handles.files(fileloop).name;
    if strfind(fname, handles.asciiname) ~= 0

        filename(handles.filenamecount,:) = char(fname);
        handles.suffix(handles.filenamecount,:) = fname(findstr(fname,'.'):findstr(fname,'.')+3);
        guidata(hObject,handles)

        fidafm = fopen([handles.filedir fname],'rt');
        contents = fread(fidafm);
        contentschars = char(contents');
        fclose(fidafm);

        rampsize = getafmparameter(contentschars,'Ramp size: V [Sens. Zscan]'); %V
        blanks = strfind(rampsize{1},' ');
        rampsize = str2num(rampsize{1}(blanks(end-1)+1:blanks(end)-1));

        zscansens = getafmparameter(contentschars,'@Sens. Zscan'); %nm/V
        blanks = strfind(zscansens{1},' ');
        zscansens = str2num(zscansens{1}(blanks(end-1)+1:blanks(end)-1));

        sampsperline = 4608;

        deltaz = rampsize * zscansens/(sampsperline - 1); %nm
        zvals = [0 : deltaz : (sampsperline - 1 ) * deltaz]';

        zscale = getafmparameter(contentschars,'Z scale: V [Sens. Deflection]');
        if isempty(zscale)
              msgstr = sprintf('\nFor File: %s:\n\nParameter "Z scale: V [Sens. Deflection]" not
found.\n',fname);
            error(msgstr);
        end
        zscale = str2num(zscale{1}(strfind(zscale{1},'(') + 1 :strfind(zscale{1},' V/LSB'))); %V/
LSB

        xxx.sensdeflection = getafmparameter(contentschars,'\@Sens. Deflection: V');
        if isempty(xxx.sensdeflection)
                  msgstr = sprintf('\nFor File: %s:\n\nParameter "\@Sens. Deflection: V" not
found.\n',fname);
            error(msgstr);
        end
        blanks = findstr(xxx.sensdeflection{1},' ');
       xxx.sensdeflection = str2num(xxx.sensdeflection{1}(blanks(1) + 1 : blanks(2) - 1)); %nm/V

       linevals = find(contents==10);
        datastart = linevals(length(linevals)-9217);
        datavals = str2num(char(contents(datastart:end)')); %LSB
         datavals = datavals .* zscale .* xxx.sensdeflection.*0.12;    %(Last value is spring con-
stant of cantilever)

        extendvals = datavals(1:4608);
        retractvals = datavals(4609:9216);
        allvals = [zvals, extendvals];          %Build matrix containing both sets of data
        %(A requirement for the use
        %of the MIN command below)

        if handles.filenamecount == 1
```

```
for i = 1:length(allvals)-1
    diffval1(i) = allvals((i+1),2) - allvals(i,2);
end

[maxdiff1, zdiffpos1] = max(diffval1);
for i = zdiffpos1:length(diffval1)
    if abs(mean(diffval1(i:i+2))) < abs(mean(diffval1) + std(diffval1))
        zmaxpos1 = i;
        break
    end
end
for i = zdiffpos1 + 1000 : length(extendvals) - 150
    m_init = polyfit(zvals(i:i+149), extendvals(i:i+149),1);
    m_init_mat(i - zdiffpos1 - 149) = m_init(1);
end
m_init_mean = mean(m_init_mat);
m_init_std = std(m_init_mat);

for i = zdiffpos1:length(extendvals) - 150
    m_test = polyfit(zvals(i:i+149), extendvals(i:i+149), 1);
    if abs(m_test(1) - m_init_mean) < m_init_std
        baselinestart1 = i;
        baselinestart_mat(handles.filenamecount,1) = i;
        baselinestart_mat(handles.filenamecount,2) = handles.filenamecount;
        break
    else
        m_test = polyfit(zvals(i:i+148), extendvals(i:i+148), 1);
        if abs(m_test(1) - m_init_mean) < m_init_std
            baselinestart1 = i;
            baselinestart_mat(handles.filenamecount,1) = i;
            baselinestart_mat(handles.filenamecount,2) = handles.filenamecount;
            break
        else
            continue
        end
    end
end

% calculate baseline value
handles.raw(:,1) = zvals;
handles.raw(:,2) = extendvals;
handles.fname = fname;
handles.zmaxpos1 = zmaxpos1;
handles.deltaz = deltaz;
handles.length = length(zvals);
stepval = double(int16(handles.zmaxpos1 - handles.raw(1,1)./handles.deltaz)) + 1;

lineav1 = mean(extendvals(baselinestart1:baselinestart1+100,1));
% lineav1 = mean(extendvals(baselinestart1:baselinestart1+500,1));
zvalmax1 = allvals(zmaxpos1,1);

handles.lineav(1) = lineav1;

handles.cut(1:size(handles.raw(stepval:end,1),1),1) = handles.raw(stepval:end,1);
handles.cut(1:size(handles.raw(stepval:end,1),1),2) = handles.raw(stepval:end,2);

handles.finalraw(1:size(handles.raw,1),1) = handles.raw(:,1);
handles.finalraw(1:size(handles.raw,1),2) = handles.raw(:,2);
handles.finalcut(1:size(handles.cut,1),1) = handles.cut(:,1) - handles.cut(1,1);
handles.finalcut(1:size(handles.cut,1),2) = handles.cut(:,2) - handles.lineav(1);

handles.stepval(1) = stepval;
handles.baselinestart(1) = baselinestart1;
guidata(hObject,handles)
```

```
        else

            for i = 1:length(allvals)-1
                diffval(i+1) = allvals((i+1),2) - allvals(i,2);
            end

            [maxdiff, zdiffpos] = max(diffval);
            for i = zdiffpos:length(diffval)
                if abs(mean(diffval(i:i+2))) < abs(mean(diffval) + std(diffval))
                    zmaxpos = i;
                    break
                end
            end

            for i = zdiffpos1 + 1000 : length(extendvals) - 150
                m_init = polyfit(zvals(i:i+149), extendvals(i:i+149),1);
                m_init_mat(i - zdiffpos1 - 149) = m_init(1);
            end
            m_init_mean = mean(m_init_mat);
            m_init_std = std(m_init_mat);

            for i = zdiffpos:length(extendvals) - 150
                m_test = polyfit(zvals(i:i+149), extendvals(i:i+149), 1);
                if abs(m_test(1) - m_init_mean) < m_init_std
                    baselinestart = i;
                    baselinestart_mat(handles.filenamecount,1) = i;
                    baselinestart_mat(handles.filenamecount,2) = handles.filenamecount;
                    break
                else
                    m_test = polyfit(zvals(i:i+148), extendvals(i:i+148), 1);
                    if abs(m_test(1) - m_init_mean) < m_init_std
                        baselinestart = i;
                        baselinestart_mat(handles.filenamecount,1) = i;
                        baselinestart_mat(handles.filenamecount,2) = handles.filenamecount;
                        break
                    else
                        continue
                    end
                end
            end

            zdiff = zvalmax1 - allvals(zmaxpos,1);
             zvals = zvals + zdiff;                %Readjust values of all subsequent matrices to
overlay with "anchor"

            handles.raw(:,1) = zvals;
            handles.raw(:,2) = extendvals;
            handles.fname = fname;
            handles.zmaxpos1 = zmaxpos1;
            handles.deltaz = deltaz;
            handles.length = length(zvals);
            stepval = double(int16(handles.zmaxpos1 - handles.raw(1,1)./handles.deltaz)) + 1;

            lineav = mean(extendvals(baselinestart:baselinestart+100,1));

            handles.lineav(handles.filenamecount) = lineav;

            handles.cut(1:size(handles.raw(stepval:end,1),1),1) = handles.raw(stepval:end,1);
            handles.cut(1:size(handles.raw(stepval:end,1),1),2) = handles.raw(stepval:end,2);

            handles.finalraw(1:size(handles.raw,1),1) = handles.raw(:,1);
            handles.finalraw(1:size(handles.raw,1),handles.filenamecount+1) = handles.raw(:,2);
            handles.finalcut(1:size(handles.cut,1),1) = handles.cut(:,1) - handles.cut(1,1);
             handles.finalcut(1:size(handles.cut,1),handles.filenamecount+1) = handles.cut(:,2) -
handles.lineav(handles.filenamecount);
```

```
            handles.stepval(handles.filenamecount) = stepval;
            handles.baselinestart(handles.filenamecount) = baselinestart;
            guidata(hObject,handles)
        end
        handles.filenamecount = handles.filenamecount + 1;
    end
end
```